Experimental studies of neoclassical tearing modes on the MAST spherical tokamak

by

Jack Snape

A thesis submitted for the
degree of Doctor of Philosophy

at the
University of York
York Plasma Institute
Department of Physics

October 2012

Abstract

Neoclassical tearing modes (NTMs) are plasma instabilities that can limit the performance of tokamaks and cause a termination of the plasma if allowed to grow. Systems to mitigate NTMs exist but have significant power requirements, which motivates further study of the mechanisms that lead to their growth in order to assist in the development of NTM avoidance strategies. NTMs typically require a seed magnetic island, above some threshold width, before they become unstable. The best available description of this threshold is the modified Rutherford equation (MRE) for NTM evolution; a combination of different models, which includes the effect of transport on NTM stability. Finite transport across magnetic field lines means that magnetic islands smaller than a critical width, w_c, do not completely flatten the pressure profiles and have a reduced bootstrap current perturbation, which leads to a threshold width, w_{th}.

This thesis describes novel measurements of NTMs with mode structure $m/n = 2/1$ on the MAST spherical tokamak (ST), which have allowed a direct evaluation of the effect of transport on island behaviour for the first time on an ST. Temperature profiles obtained with the upgraded Thomson scattering system on MAST have been used to constrain the solutions of a heat transport equation for a magnetic island [1], allowing the experimental determination of w_c, an important parameter in the MRE. The measured value of $w_c = 0.7 \pm 0.2$cm obtained for an ensemble of MAST discharges is used in an analysis of the MRE for 2/1 NTM onset and saturation on MAST. By using a probabilistic method for parameter and error estimation, which takes account of the experimental uncertainty on measured equilibrium parameters, it is found that the temporal evolution of the island size is well described by marginally, classically unstable NTMs (that is, $\Delta' \gtrsim 0$) with strongly destabilising bootstrap current and stabilising curvature terms. Finally, an analysis of two β ramp-down discharges is presented, in which the measured w_c value explains the observed threshold width well.

Contents

List of Figures

Acknowledgements

Firstly, I would like to thank Kieran Gibson for his guidance and encouragement during the production of this thesis and the other activities that I have undertaken during my PhD. I would also like to thank Tom O'Gorman for many useful conversations about the research in this thesis and the quirks of the MAST tokamak. I would like to thank Howard Wilson for the opportunities and training provided through the Fusion Doctoral Training Network and for his valuable advice. I also received a great deal of support while conducting experiments at the Culham Centre for Fusion Energy from Ian Chapman, Andrew Thornton, Geof Cunningham, Rory Scannell, Andrew Kirk, Anthony Field and the rest of the MAST team, which has been much appreciated. I would also like to thank Jakob Svensson and Koki Imada for helping me make tentative steps towards work beyond this thesis.

I have made some firm friends on the Fusion Doctoral Training Network who have blocked the path to the completion of this thesis with numerous amusing distractions. I can't mention everybody but in particular I'd like to thank Andy, Tom, Lee, Billy, James, Sarah, Lucy, Özgür, Ed, Llion, Matt and Ben.

Finally, thank you to my family and to Kristina for being there through my PhD and for not complaining too much when I felt the need to talk about magnetic islands.

Declaration of Authorship

I, JACK SNAPE, declare that this thesis titled, 'EXPERIMENTAL STUDIES OF NEOCLASSICAL TEARING MODES ON THE MAST SPHERICAL TOKAMAK' and the work presented in it are my own. I confirm that:

- This work was done wholly while in candidature for a research degree at this University.
- Where I have consulted the published work of others, this is always clearly attributed.
- Where I have quoted from the work of others, the source is always given. With the exception of such quotations, this thesis is entirely my own work.
- I have acknowledged all main sources of help.

Chapter 1

Introduction

1.1 Fusion power

The sun is the solar system's main source of power, producing approximately 3.8×10^{26} Watts. In 1939 nuclear fusion was identified as the origin of this power [2]. What emerged from this discovery was the idea that the human race could harness nuclear fusion to generate electricity. Since the late 1940s there have been many experiments investigating the production of controlled fusion reactions on Earth. Though many advances have been made, a series of physics and engineering challenges have slowed progress towards commercial fusion power.

Fusion power is arguably more necessary now than it was at the time of its conception for a number of reasons. As of 2011, fossil fuels make up approximately 81% of global energy consumption [3] but these resources are finite. For example, in the 1950s it was predicted that the rate at which the human race consumes oil will increase until the Earth's oil fields are so depleted that the rate of consumption is forced to drop [4]. The theory is known as "Peak oil" and it is forecasted that this maximum will occur in a matter of decades [5] after which the amount of energy available from oil will decline and alternative energy sources will be required to make up the deficit. Also, a combination of population increase and the industrialisation of developing countries will continue to push global energy demand upwards. By 2030, global demand is predicted to increase by around 40% [6]. Furthermore, it is now widely accepted that the combustion of fossil fuels has caused an increased concentration of greenhouse gases in Earth's atmosphere, that this is the main cause of the global warming observed throughout the 20^{th} century and that the temperature will continue to rise unless these concentrations are reduced

very soon. Such a temperature increase is likely to cause droughts, rising sea levels and a series of other potentially catastrophic events [7].

For these reasons it is clear that providing sufficient energy for the future will be extremely challenging. It will be necessary to move away from fossil fuels and find alternative sources of energy that can not only replace but surpass the current capacity of fossil fuels to satisfy global energy demand.

It is likely that nuclear fission power will provide a significant fraction of the future energy market but the proliferation of nuclear weapons, the safe and ecological storage of long-lived nuclear waste and the risk of a large scale disaster all remain a genuine concern. The main drawbacks associated with renewable technologies are their relative expense, large land requirements and inconsistent power output due to natural variations in the input source. Solar power from photo-voltaic cells is the most promising of these technologies but with current levels of efficiency, approximately 0.5% of Earth's landmass would need to be covered to meet current energy demand [8].

It is possible to take the list of problems associated with current energy sources and turn it into a "wish-list" of properties, which an ideal future source of power would possess. It should have an abundant source of fuel, not produce greenhouse gases, not produce long-lived nuclear waste, be free from the risk of large scale disasters, generate energy at a consistent rate, use a small amount of land to produce a large amount of energy and be commercially attractive for private sector investment. Fusion power has the potential to fulfill all of these criteria but a number of problems remain to be solved before it can be made commercially viable.

1.1.1 Fusion reactions

In a fusion reaction, two light nuclei must come close enough together that the short-range, attractive, strong nuclear force becomes larger than the electrostatic repulsion between their nuclei. Energy is released because the total mass of the constituents is greater than the total mass of the products. The "missing" mass, m, is converted into a certain amount of energy, E, given by the famous equation, $E = mc^2$ [9].

The reaction between deuterium and tritium is most commonly used in fusion reactor design. The main reason for this is that the cross section peak is both higher and at a temperature lower than that of any other fusion reaction, as illustrated by figure 1.1, but also because the reactants can be obtained with relative ease and because a large

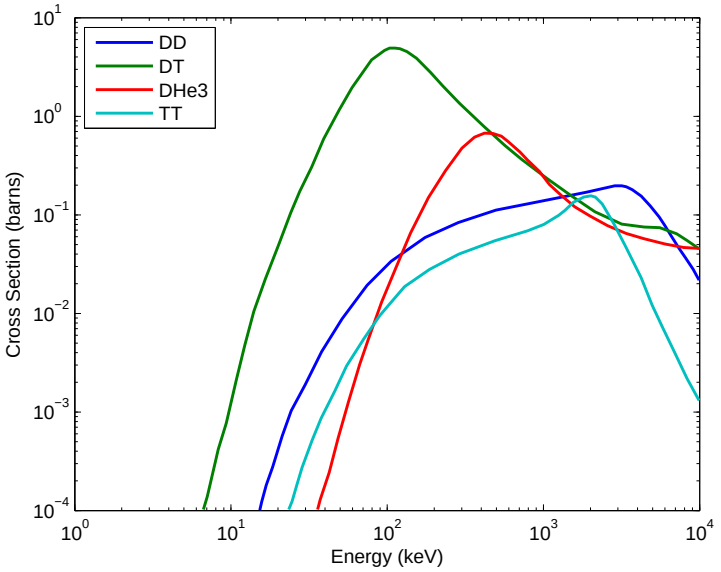

FIGURE 1.1: Fusion cross sections for light nuclei as a function of particle energy.

amount of energy is released. Deuterium can be extracted from sea water and tritium can be produced through nuclear fission reactions between lithium and a neutron. The products of the DT reaction are a helium nucleus (α particle) with 3.5MeV and a neutron with 14.1MeV (see equation 1.1). This neutron can then be used to breed tritium from lithium (see equations 1.2 and 1.3).

$$ {}^{2}_{1}\mathrm{D} + {}^{3}_{1}\mathrm{T} \rightarrow {}^{4}_{2}\mathrm{He} + \mathrm{n} + 17.6\mathrm{MeV} \tag{1.1} $$

$$ {}^{6}_{3}\mathrm{Li} + \mathrm{n} \rightarrow {}^{4}_{2}\mathrm{He} + {}^{3}_{1}\mathrm{T} + 4.8\mathrm{MeV} \tag{1.2} $$

$$ {}^{7}_{3}\mathrm{Li} + \mathrm{n} \rightarrow {}^{4}_{2}\mathrm{He} + {}^{3}_{1}\mathrm{T} + \mathrm{n} - 2.5\mathrm{MeV} \tag{1.3} $$

For the nuclei to overcome the Coulomb barrier and achieve fusion, they require a certain amount of energy. If this energy can be supplied by a sufficient number of fusing nuclei then the reaction will be self sustaining. This threshold is called ignition and in 1957 John D. Lawson calculated the criteria for this to be achieved [10]. The calculation uses a number of assumptions, such as the fuel being pure DT with no impurity or ${}^{4}_{2}\mathrm{He}$ component, but it provides a useful lower limit for the ignition criterion. It is most commonly expressed in the form of the fusion triple product:

$$ n\,T\,\tau_E \geq \frac{12}{E_{fus}}\frac{T^2}{\langle\sigma v\rangle} \approx 10^{21}\mathrm{keV\ s/m^3} \qquad \text{(for the DT reaction)} \tag{1.4} $$

Here, n is the density, T is the temperature and τ_E is the energy confinement time which is a measure of the rate at which energy is lost to the environment. At this point it is worth noting that throughout this thesis, and in plasma physics more generally, temperatures are usually expressed in units of electron-volts (eV).

Equation 1.4 leads to the classification of two different schemes for fusion reactor design. Both aim to increase the temperature towards the peak cross-section energy in figure 1.1 (around 100 million degrees), an important consequence of which is that the DT fuel becomes a fully ionised plasma (see section 1.2). In addition, one scheme simultaneously tries to maximise the density for a short period of time whilst the other aims to maximise the confinement time at lower density. In the first scheme, known as "Inertial Confinement Fusion" (ICF), a pellet of DT fuel is heated and compressed using pulsed, high powered lasers. The energy is confined for a short period of time using the inertia of the collapsing fuel pellet. In the second scheme, known as "Magnetic Confinement Fusion" (MCF) on which this thesis will focus, the plasma fuel is confined by magnetic fields whilst being heated. If a sufficient fusion reaction rate was achieved, an MCF reactor could operate steady-state with a relatively small amount of external heating and current drive. It is worth noting that the sun's core temperature and density are not high compared to man-made MCF and ICF experiments but it is able to operate as a successful fusion reactor because it has an extremely long confinement time.

In the race to find a configuration capable of achieving commercial MCF power, the tokamak is generally considered to be the front-runner (see section 1.3). There are many tokamaks conducting MCF experiments around the world, the largest of which is JET at Culham, Oxfordshire. JET and TFTR (Princeton) have had some DT operation but most current tokamaks use 100% deuterium fuel as the neutron flux from the DT reaction requires costly safety measures. In addition, large supplies of tritium are not available because it has a short half-life and is only currently produced in a limited number of fission laboratories. Much of the research done in the MCF community is in preparation for the ITER project. ITER will be the largest tokamak ever. The main project aims are to demonstrate a DT plasma, producing 10 times more fusion power than applied heating power, lasting for $\sim$3000s [11]. This would be considered proof that MCF fusion is technically feasible and would be followed by the construction of a demonstration power station. Construction of ITER has commenced in the south of France and completion is expected by the end of the decade. Though it will be larger than any current tokamak, it is likely to be faced with some similar challenges and a more

complete understanding of phenomena on smaller machines will help in the preparation for ITER. The tokamak on which this thesis will focus is MAST, also at Culham.

1.2 Plasma physics

A plasma is a gas-like ensemble of particles, a significant fraction of which are ionised. An important characteristic of a plasma is that it exhibits collective behaviour. For example, the charged particles in a plasma tend to rearrange themselves to cancel out any electric fields, so that the plasma is 'quasi-neutral'. These collective effects can only be understood by considering the plasma as an ensemble but discussions of plasma behaviour often begin by considering the motion of individual charged particles, as this can help to demonstrate a number of other important effects.

A charged particle can respond to electric and magnetic fields in a variety of ways depending on the field configuration. For example, a positive ion will experience a force parallel to the electric field and will be accelerated in that direction. In a magnetic field, the particle experiences a force perpendicular to the field which gives rise to a circular motion (with speed, $v_\perp$) around the field line. The radius of the circular motion, given by $r_L = mv_\perp/eB$, is known as the *Larmor radius*. If the velocity also has a parallel component ($v_\parallel$) this circular path becomes helical.

When different fields and forces are combined, or vary in space, the particle can experience an extra component of velocity known as a *drift*. Important examples are the $\mathbf{E} \times \mathbf{B}$ drift and the ∇B drift. Figure 1.2 shows that these drifts can be explained in terms of changes in r_L. a) $\mathbf{E} \times \mathbf{B}$ - The ion circular motion is alternately parallel and anti-parallel to $\mathbf{E}$. It is accelerated during its descent and decelerated during its ascent, so the net motion is downwards. This drift is in the same direction for electrons and ions. b) ∇B - When the particle is in the high $|\mathbf{B}|$ region, r_L is smaller than in the low $|\mathbf{B}|$ region. This causes a sideways drift in opposite directions for electrons and ions.

If the magnetic field strength increases in the direction of the field, the particle will experience a *magnetic mirror force* in the opposite direction. Figure 1.2c shows how magnetic field lines come closer together in a region of high field. Where $|\mathbf{B}|$ is increasing, there is a component of the field ($\mathbf{B}_r$) in the radial direction of the particle's circular orbit. As this is perpendicular to the velocity, there is a force, $\mathbf{F}_{mirror} = q\mathbf{v} \times \mathbf{B_r}$, that pushes the particle towards the low field region. Another way to understand this is to consider the fact that the magnetic moment, μ, is conserved. As the particle enters

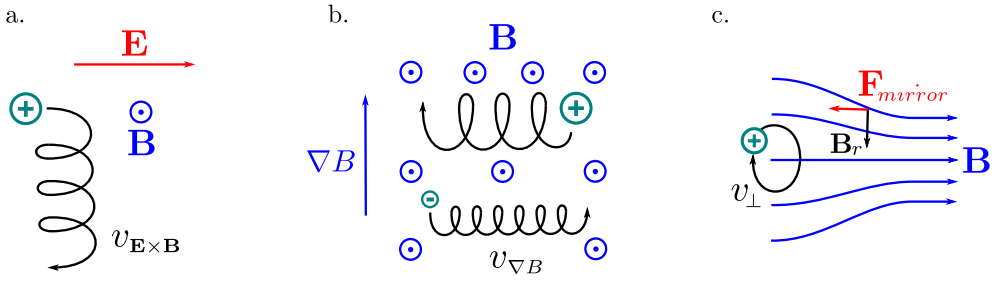

FIGURE 1.2: a) $\mathbf{E}\times\mathbf{B}$ drift ($\mathbf{B}$ out of the page). b) ∇B drift. c) Magnetic mirror.

the high field region its Larmor radius decreases so, to conserve μ, its perpendicular velocity increases. As energy must also be conserved, this leads to a reduction in the parallel velocity.

Though study of single particle motion can be instructive, the task of simulating a plasma requires a higher level formalism, such as the kinetic description or the Magneto-Hydrodynamic (MHD) fluid description, which will be used in this thesis. The set of four solveable MHD equations is obtained by taking moments of the particle distribution function and using the adiabatic equation of state as a closure relation. The MHD equations, outlined below, assume the electron mass is negligible compared to the ion mass in order to treat the electrons and ions as a single fluid. The validity of these equations breaks down when the system under consideration is small enough to be comparable with the Larmor radius or when the mean free path of a particle becomes comparable to the system length scale. This can be an issue when considering the plasma's behaviour in the direction parallel to the magnetic field, where the mean free path is often much longer than it is perpendicular to the field.

$$\frac{\partial \rho}{\partial t} + \nabla \cdot (\rho \mathbf{u}) = 0 \tag{1.5}$$

$$\rho \left[\frac{\partial \mathbf{u}}{\partial t} + (\mathbf{u} \cdot \nabla)\, \mathbf{u} \right] = -\nabla p + \mathbf{J} \times \mathbf{B} \tag{1.6}$$

$$\frac{\partial p}{\partial t} + (\mathbf{u} \cdot \nabla)\, p = -\gamma p\, (\nabla \cdot \mathbf{u}) \tag{1.7}$$

$$\mathbf{E} + \mathbf{u} \times \mathbf{B} = \eta \mathbf{J} \tag{1.8}$$

Here, ρ is the mass density, $\mathbf{u}$ is the flow, $\mathbf{J}$ is the current, $\mathbf{B}$ is the magnetic field, p is the pressure, γ is ratio of specific heats, $\mathbf{E}$ is the electric field and η is the resistivity. Equation 1.5 is the equation of continuity which is an expression of mass conservation.

Equation 1.6 is the force balance equation which describes the flow of plasma under the influence of a combination of magnetic and pressure forces. Equation 1.7 is the equation of state, which assumes that the plasma behaves adiabatically. Equation 1.8 is a version of Ohm's law describing the influence of electric fields on a plasma with finite resistivity, η. These equations ignore some important physics but they do provide a useful (and surprisingly accurate) starting point for analysis of plasma stability.

If the plasma resistivity is small then Ohm's law becomes $\mathbf{E} + \mathbf{u} \times \mathbf{B} = 0$. Consider the magnetic flux through a surface S, $\Psi = \int_S \mathbf{B}.d\mathbf{S}$ (see figure 1.3). The rate of change of flux through this surface is the sum of two parts: 1) The change in background flux. 2) The plasma flow changes the size and shape of the curve C, also changing the flux through the loop. Equation 1.9 shows these two parts summed together.

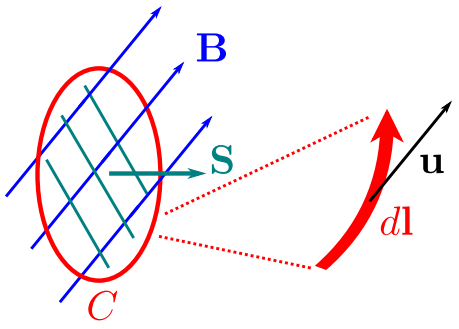

FIGURE 1.3: The flux through surface S bounded by curve C in a plasma with flow $\mathbf{u}$.

$$\frac{d\Psi}{dt} = \int_S \frac{\partial \mathbf{B}}{\partial t}.d\mathbf{S} + \oint_C \mathbf{B}.(\mathbf{u} \times d\mathbf{l}) \tag{1.9}$$

$$\frac{d\Psi}{dt} = -\int_S \nabla \times \mathbf{E}.d\mathbf{S} - \oint_C \mathbf{u} \times \mathbf{B}.d\mathbf{l}$$

$$\frac{d\Psi}{dt} = -\int_S \nabla \times [\mathbf{E} + \mathbf{u} \times \mathbf{B}] .d\mathbf{S} = 0 \tag{1.10}$$

Equation 1.10 shows that for $\eta = 0$, $d\Psi/dt$ through any surface is zero. The significance of this result is that in the $\eta = 0$ case, magnetic flux is *frozen in* to the plasma. That is, the field lines move with the plasma and vice versa. In some cases, it is important to take into account the finite resistivity of the plasma. Equation 1.11 is obtained by taking the curl of equation 1.8 (Ohm's law).

$$\frac{\partial \mathbf{B}}{\partial t} = \nabla \times (\mathbf{u} \times \mathbf{B}) + \frac{\eta}{\mu_0} \nabla^2 \mathbf{B} \tag{1.11}$$

This is has the form of a convection-diffusion equation. The movement of the field lines with the plasma is described by the first term (this is the *frozen in* part) while their diffusion through the plasma is described by the second term [12]. The ratio of these two terms is approximately expressed as the *Lundquist number*, S (equation 1.12). If S is small then the diffusive term becomes important and the magnetic field lines can move through the plasma and even tear and reconnect to form a completely new topology. This process is called *magnetic reconnection*; a key concept in this thesis.

$$S \approx \frac{|\nabla \times (\mathbf{u} \times \mathbf{B})|}{|\frac{\eta}{\mu_0} \nabla^2 \mathbf{B}|} \approx \frac{\mu_0 L V_A}{\eta} \tag{1.12}$$

where L is the system length scale and V_A is the Alfvén speed. There are certain thin layers within a tokamak plasma that have very short system length scales and a small S value, which means that resistivity is important to consider and that magnetic reconnection can become favourable. Because of this, these regions can become susceptible to the growth of a type of resistive plasma instability called a *neoclassical tearing mode* (NTM). NTMs can impair the performance of a tokamak by reducing the temperature of the core plasma or by causing a plasma disruption if allowed to grow to a large size (see section 1.4). The aim of this thesis is to develop a deeper understanding of the onset and growth of NTMs in order to find ways of minimising these effects.

1.3 Tokamaks

1.3.1 Magnetic field configuration

In the limit of zero plasma resistivity and viscosity (i.e. no collisions between particles, so-called *ideal MHD*), the particles tend to stay within r_L of a field line. If a field line joins back on itself, the particles will be confined to stream along it (neglecting drifts). The simplest way to bend a column of plasma to join back on itself is the *toroidal* geometry. Figure 1.4a shows half a *torus* with the relevant toroidal coordinates.

Here, r is the minor radius (a is the value of r at the plasma edge), R is the major radius (R_0 is the value of R at the magnetic axis), θ is the poloidal angle, ϕ is the toroidal angle and Z is the vertical coordinate. The usual method for inducing a toroidal field,

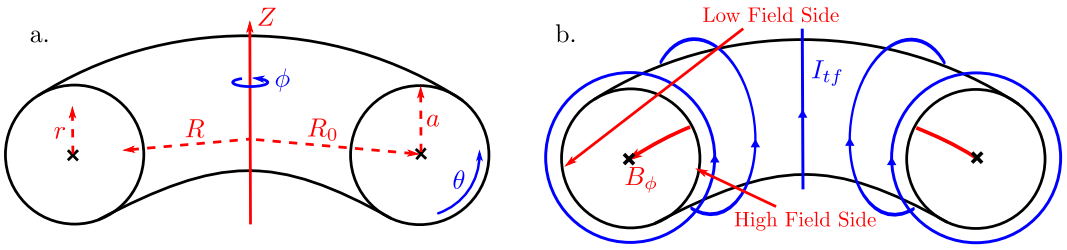

FIGURE 1.4: a) Toroidal geometry. b) Toroidal field generation in a torus.

B_ϕ, is to wrap a series of coils, carrying toroidal field current, I_{tf}, around the toroidal vessel (see figure 1.4b). As the coils are more closely spaced on the inside of the torus, the toroidal field strength varies approximately like $B_\phi \sim 1/R$. This makes it necessary to distinguish between the high and low field sides of the vessel, known as the *inboard* and *outboard* sides, respectively.

An important consequence of this $1/R$ dependence is that there is a ∇B drift; in opposite directions for electrons and ions. Similarly, the toroidal curvature of the magnetic field gives rise to a curvature drift, in the same direction as the ∇B drift. Figure 1.5a shows that if the field was purely in the toroidal direction, the ions and electrons would separate, giving rise to an electric field. In combination with the toroidal magnetic field, this electric field would cause both species to have an $\mathbf{E} \times \mathbf{B}$ drift out of the plasma, resulting in complete loss of plasma confinement.

The solution is to include another magnetic field in the poloidal direction, B_θ. This can be done using specially shaped coils or by ramping current through a central solenoid to produce a time varying magnetic field in the Z direction, which generates a toroidal plasma current (I_p) and an associated B_θ, as shown in figure 1.5b. The sum of B_θ and B_ϕ has a toroidal helix shape, which prevents either species from collecting at the top or bottom of the vessel. The ∇B and curvature drifts still exist but by avoiding charge accumulation, large scale $\mathbf{E} \times \mathbf{B}$ drifts are eliminated. In general, the combination of a poloidal and toroidal field is known as the *toroidal pinch*.

The amount the helical field lines 'twist' in a toroidal pinch is quantified by a parameter known as the safety factor, q. This is defined as the number of times a field line winds around the torus toroidally for every once poloidally. At this point it is necessary to state, without proof, that magnetic field lines lie in closed toroidal surfaces. This is discussed more thoroughly in section 1.3.2. The magnetic surfaces where q has a rational value are of particular interest, as the field lines connect back on themselves and

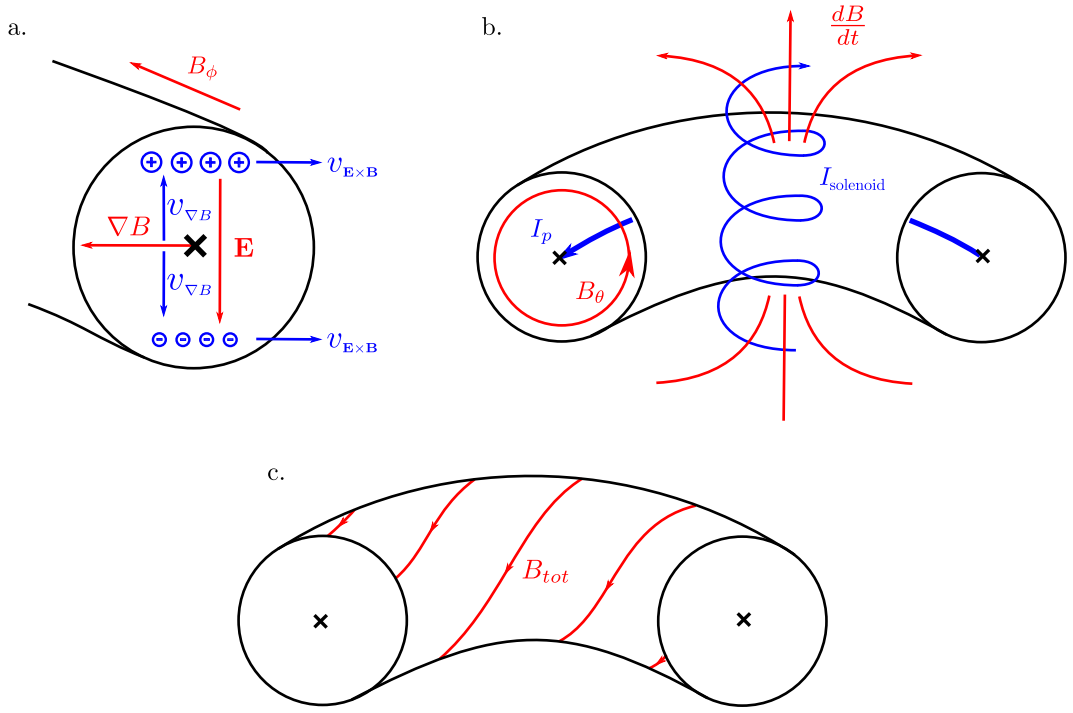

FIGURE 1.5: a) Drifts with a purely toroidal field. b) Poloidal field. c) Total helical field.

perturbations to these field lines have periodic boundary conditions. This means that these surfaces are resonant with particular *modes*, made up of toroidal and poloidal harmonics with toroidal mode number, n, and the poloidal mode number, m. Modes with a particular combination of m and n will be resonant on surfaces with $q = m/n$. These modes may be unstable and grow in amplitude so are often referred to as *instabilities*. Furthermore, the plasma resistivity can become important at these rational surfaces, making them susceptible to magnetic reconnection and resistive instabilities, such as tearing modes (as was mentioned in section 1.2). The radial gradient of the q profile is also an important parameter in determining the stability of modes and is normally expressed in terms of the *magnetic shear* defined as:

$$s = \frac{r}{q}\frac{dq}{dr} \tag{1.13}$$

There are three stable variations of the toroidal pinch, with different q profiles shown in figure 1.6. These configurations often have q profiles tailored to avoid the $q = 1$ surface, as it can be become susceptible to large and rapidly growing $m/n = 1/1$ kink-like instabilities. The *stellarator* consists of a series of twisted coils, which provide a helical field without the need for a plasma current. Its safety factor profile usually has negative magnetic shear and, though there are a variety of different stellarator q profile

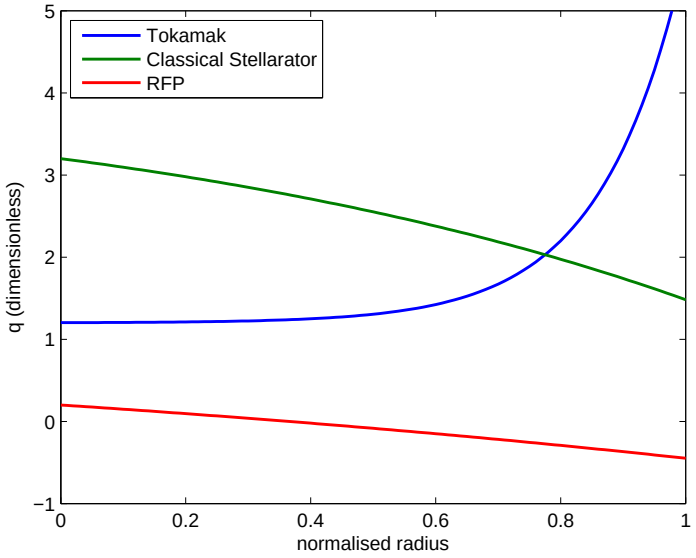

FIGURE 1.6: Safety factor for different toroidal pinch configurations as a function of normalised minor radius [13].

designs, the classical stellarator q profile goes from 2-3 at the axis to about 1 at the edge. The *reversed field pinch* (RFP) uses a plasma current to produce a poloidal field of similar magnitude to the external toroidal field. The RFP is a self organised plasma configuration; a minimum energy state, in which the toroidal field spontaneously changes direction close to the plasma edge. This leads to a very low negative shear safety factor profile, with a central q of just below 1 and an edge q of just below 0. The *tokamak* has a toroidal field much stronger than its poloidal field. It's safety factor profile usually has positive magnetic shear, starting at around 1 at the centre and increases to somewhere in the range 3-10 towards the plasma edge.

1.3.2 Equilibrium

It is instructive to study the MHD equilibrium in a tokamak. Conventionally axisymmetry is assumed, which allows much of the analysis to be restricted to the poloidal plane. If we assume that the global plasma flow is zero, the force balance equation (equation 1.6) becomes $\nabla p = \mathbf{J} \times \mathbf{B}$.

Combining force balance and Ampère's law gives:

$$\begin{aligned} \mathbf{J} \times \mathbf{B} &= \frac{1}{\mu_0} (\nabla \times \mathbf{B}) \times \mathbf{B} \\ &= \frac{1}{\mu_0} (\mathbf{B}.\nabla) \mathbf{B} - \frac{1}{2\mu_0} \nabla B^2 \end{aligned} \tag{1.14}$$

The first term of equation 1.14 describes the forces due to the curvature of the magnetic field. The fact that it takes energy to bend magnetic field lines has important implications for plasma stability and this is discussed later. The second term describes the magnetic pressure forces that act when field lines are compressed together. An important equilibrium parameter is the ratio of the plasma pressure and this magnetic pressure:

$$\beta = \frac{p}{B^2/2\mu_0} \tag{1.15}$$

The magnetic pressure is related to the strength of the externally applied field which should be minimised to reduce the power requirements of the tokamak. A high β scenario is desirable as it uses relatively little magnetic pressure to achieve a hot and dense plasma. Another, similar parameter of interest is β_p, the poloidal β, which is calculated by replacing B with B_θ in equation 1.15.

The plasma β cannot increase indefinitely, as eventually global MHD instabilities rapidly grow and terminate the plasma. Troyon calculated the β limit beyond which the plasma, without a stabilising metal wall, becomes globally unstable to an ideal kink mode [14]. For a large aspect ratio, circular cross section tokamak, this limit was found to follow the scaling $\beta_N = 4l_i$ [15], where $\beta_N = \beta[\%] \frac{a[\mathrm{m}]B[\mathrm{T}]}{I_p[\mathrm{MA}]}$ is the 'normalised β' and $l_i = 2\int_0^a B_\theta r dr / a^2 B_\theta(a)$ is the plasma internal inductance.

In a successful MCF device, the pressure should be greater in the core than at the edges, with nested surfaces of constant p (see figure 1.7). As p is a scalar field, ∇p will always point perpendicular to these surfaces. The surface area of the inboard side of a torus is less than that of the outboard side. Since pressure is force per unit area and is constant on a surface, the surfaces are pushed away from the inboard side so that the maximum pressure is shifted off centre. This contributes to a shift of the flux surfaces towards the outboard side of the torus, known as the *Shafranov shift* (see figure 1.7), which leads to a distinction between the geometric and magnetic axes of the plasma. In this thesis, 'axis' will generally refer to the magnetic axis.

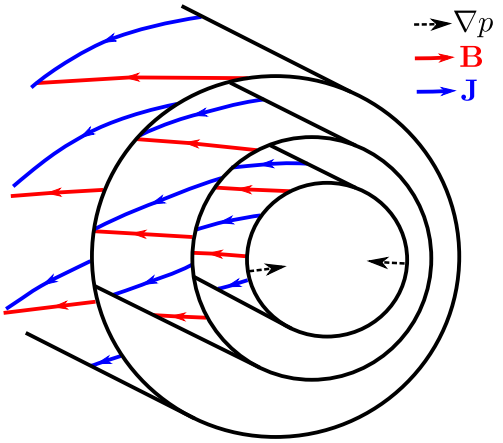

FIGURE 1.7: Surfaces of constant pressure with Shafranov shift off axis. Magnetic field lines and currents lie in surfaces.

The dot product of the equilibrium force balance with $\mathbf{B}$ gives $\mathbf{B}.\nabla p = 0$ and the dot product with $\mathbf{J}$ gives $\mathbf{J}.\nabla p = 0$. This means that both $\mathbf{B}$ and $\mathbf{J}$ lie in the surfaces of constant p, perpendicular to ∇p, which is illustrated in figure 1.7. This result can be used to show that the magnetic flux due to the poloidal field, Ψ, is also constant on a pressure surface. It is often useful to label each surface by its local Ψ value (renaming them *flux surfaces*) and to use Ψ as a substitute spatial coordinate, independent of plasma cross section shape (unlike r).

Transport of heat and particles is much faster parallel to magnetic field lines than it is perpendicular to magnetic field lines. Field lines that lie in closed equilibrium flux surfaces, are good for confinement because they only allow slower perpendicular transport of heat and particles out of the plasma. Any perturbation or instability that breaks open flux surfaces or provides a component of the magnetic field perpendicular to the equilibrium surfaces will have a detrimental effect on confinement as heat and particles can free stream out of the plasma. Instabilities such as neoclassical tearing modes can have such an effect and this will be revisited in more detail later.

Force balance is also influenced by the rotation of the plasma. This rotation is primarily in the toroidal direction and to a large extent is driven by momentum input from the tangential neutral beams (covered in section 1.3.4), although there is some intrinsic toroidal and poloidal rotation the cause of which is not fully understood. The toroidal rotation usually has a sheared profile with a high rotation in the plasma core, which tends to be beneficial for stability, although there is still some debate about the effects of rotation shear. Loss of rotation often results in a disruption of the plasma.

A range of other factors can influence plasma equilibrium from fast particles produced in the plasma core by external heat sources to the influx of impurities and neutrals at the plasma edge. Some of these other factors will be looked at in Chapter 2, when considering MAST equilibria in more depth.

1.3.3 Plasma stability

Sections 1.3.1 and 1.3.2 described some of the properties of plasma equilibrium that can lead to the growth of instabilities, such as high β or the presence of rational q surfaces. Plasma stability is often determined by considering whether there is free energy available for a perturbation to grow, which can be influenced by a wide range of local and global plasma parameters.

Pressure gradients are one potential source of free energy to drive instability growth. One example of this is the Edge Localised Mode (ELM), a periodic eruption of the plasma edge, which can cause highly damaging transient heat loads on the plasma-facing components. In 1982, a new high β operational regime was discovered when a new plasma edge configuration, called a *divertor* (see section 1.3.5), was used [16]. This high confinement mode (*H-mode*, in contrast to the low confinement, *L-mode*) has a steep edge pressure gradient (or *pedestal*) and a significantly higher core pressure (see figure 1.8). The confinement time was found to approximately double. H-mode seems to be an advantageous operational regime for an MCF reactor but this high pedestal pressure gradient makes the edge plasma susceptible to ELMs, which are likely to cause unacceptable levels of damage if not mitigated on ITER.

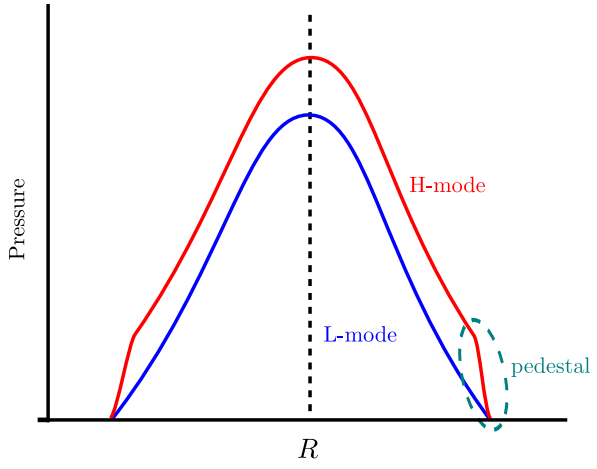

FIGURE 1.8: Typical pressure profiles for L and H mode operational regimes.

Another important parameter for determining plasma stability is the *curvature* of the field, $\varkappa$, defined as a unit vector which points from the infinitesimal arc of field line towards the centre of the arc's circle. MHD stability analysis shows that in regions where $\nabla p.\varkappa > 0$, such as the outboard side of the torus, the curvature has a destabilising effect on perturbations, whereas curvature acts to stabilise on the inboard side, which has $\nabla p.\varkappa < 0$. This effect is seen in experimental observations of ELMs, which erupt much more violently on the outboard side of the tokamak.

This thesis considers the various contributions to the stability of neoclassical tearing modes, which includes the effects of pressure gradients, curvature and also other effects such as the shape of the current profile. Further details can be found in Chapters 3 and 6.

1.3.4 Heating and current drive

The magnetic fields provide the plasma confinement, but to access the Lawson ignition condition the plasma must also be heated. There are three main heat sources used in tokamaks:

1. The plasma current provides ohmic heating.

2. Radio or microwave frequency radiation, resonant with certain plasma oscillations, is used as a source of heating. Common examples are ion and electron cyclotron resonance heating (ICRH and ECRH). A similar system can be used to drive current (e.g. electron cyclotron current drive, ECCD).

3. High energy beams of neutral deuterium atoms are often injected into the plasma. This neutral beam injection (NBI) provides heating, current drive and angular momentum in the toroidal direction.

1.3.5 Tokamak design

Tokamaks are designed in a variety of different sizes and configurations, but a number of features are common to most modern tokamaks. Figure 1.9 shows a schematic of a tokamak with some of these features labelled.

The *first wall* faces the plasma and is built to withstand high heat loads and exposure to x-rays caused by runaway electrons during a disruption. Graphite tiles are used for the first wall in many tokamaks (e.g. MAST) but sometimes metal walls are used such

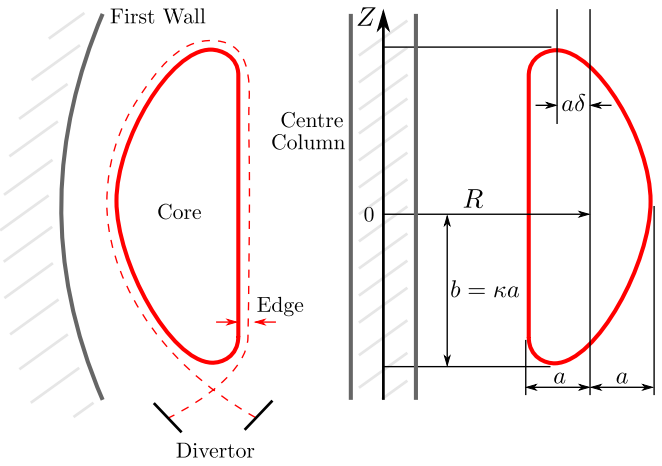

FIGURE 1.9: A tokamak plasma cross section with shaping. The dashed red line is the separatrix and the solid red line is the last closed flux surface. δ is the triangularity and κ is the elongation.

as in JET, which is currently using an all metal wall in preparation for ITER. The *centre column* contains the central solenoid and the inner loop of the toroidal field coils. It is protected by the first wall. The *divertor* is the point where the plasma makes contact with the first wall. The magnetic field configuration in a divertor tokamak has a field null X-point, just above the divertor, which creates a separatrix flux surface and two legs down which plasma streams onto the divertor target plates. Building these plates to withstand high heat loads, particularly transient events, presents a real challenge.

Just inside the separatrix is the *last closed flux surface* (LCFS) and just outside it is the region called the *scrape-off layer* (SOL). The flux region spanning from $\Psi/\Psi_{LCFS} \approx 0.95$ to just outside the SOL is called the *edge* plasma. The physics of this region is very complex due to the steep gradients in pressure and current and the large neutral particle fraction, but this will not be covered in detail in this thesis. The *core* plasma is fully ionised and is usually confined by closed toroidal flux surfaces. The low q values in this region make it susceptible to large scale, low m/n MHD instabilities, which will be the focus of this thesis.

The plasma cross section used in most tokamak experiments is not circular but 'D' shaped (see figure 1.9), characterised by the triangularity parameter, δ, and the elongation parameter, κ. One advantage of this shape is that it allows a higher achievable plasma pressure. A number of additional magnetic coils are required to provide this plasma shaping, as well as for position control.

1.3.5.1 Spherical tokamaks

Another important parameter is the aspect ratio of the torus, R_0/a. If this parameter is large, the toroidal curvature of the plasma is small and a cylindrical approximation can be made. Figure 1.10 shows the path followed by field lines in the large and small aspect ratio cases for a $q = 5$ flux surface. A small aspect ratio tokamak is usually called a *Spherical Tokamak* (ST). This thesis will focus on data from the Mega Amp Spherical Tokamak (MAST), which is described in more detail in Chapter 3.

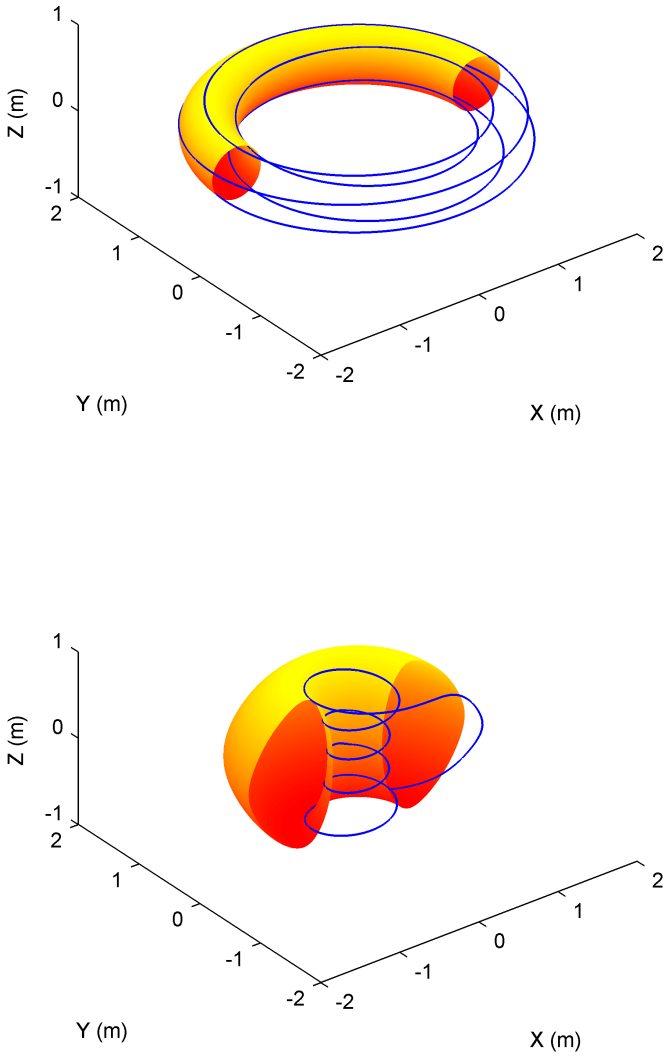

FIGURE 1.10: Comparison of magnetic field lines in a conventional large aspect ratio tokamak and spherical tokamak (ST).

The ST has a number of advantages over the conventional, large aspect ratio tokamak. As the inboard side of a flux surface is much closer to the centre column, the magnetic field is considerably stronger there than on the outboard side. This means that a magnetic field line winds more tightly around the centre column, as shown in figure 1.10, and there is more field line length in 'good curvature' regions. The ST is therefore able to achieve higher β than a conventional tokamak due to improved plasma stability. Increases in natural elongation and triangularity also contribute to this effect. Another advantage is that pushing the plasma closer to the centre column can provide a large *bootstrap current*, a current intrinsically generated by a tokamak plasma, which is described below, in section 1.3.6.

1.3.6 The neoclassical model

In the large aspect ratio approximation, the magnetic field is generally assumed to be constant on a flux surface. This is known as the *classical model*. Section 1.3.5.1 showed that, for smaller aspect ratio machines, differences in the field strength on the inboard and outboard side become important. A more realistic approach is the *neoclassical model* in which the $1/R$ dependence of the toroidal field is included. One consequence is that particles with low $v_{\|}/|\mathbf{v}|$ experience a magnetic mirror force and become trapped on the outboard side of the tokamak. Their trajectories almost follow field lines but are lifted slightly off this course by the ∇B drift (see figure 1.11a). When projected onto the poloidal plane this path has a banana shape and as a result is called a *banana orbit*. It can be shown that the banana orbit width is $w_b \sim \frac{\pi}{\sqrt{2}} \frac{qr_L}{\sqrt{\varepsilon}} > r_L$.

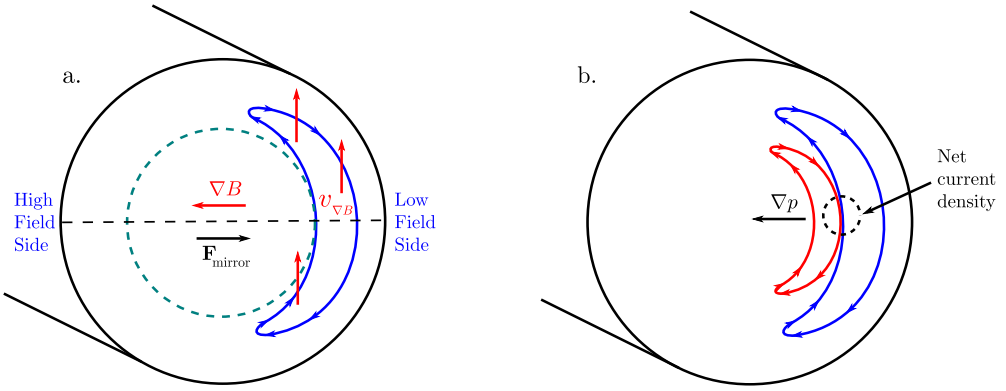

FIGURE 1.11: a) Banana orbit trajectory in the poloidal plane. b) Neighbouring banana orbits in a pressure gradient.

Unfortunately for confinement, diffusion of heat and particles across field lines is inherent in all tokamaks. Initially, it was thought that the mechanism for such diffusion was Coulomb collisions and that the diffusivity of a plasma is related to the mean free path of the particles, λ_{mf}. In a collisional plasma, the particle mean free path is approximately equal to the Larmor radius, r_L. As the plasma moves to higher temperature, the resistivity of the plasma decreases and fewer collisions occur. Here, particles are often able to follow full banana orbits before collisions occur and as such it is called the banana regime, so $\lambda_{mf} \sim w_b > r_L$. This means that the banana regime has an enhanced diffusivity and transport of heat and particles out of the plasma is increased. However, the observed perpendicular transport is still higher than the values predicted by neoclassical theory and it is now understood that the dominant transport mechanism in tokamaks is turbulence.

Kinetic theory considerations of electron-ion momentum exchange in the banana regime predict a field-aligned current known as the bootstrap current [17]. The bootstrap current has been measured experimentally and is found to agree with theoretical predictions [18]. It is possible to obtain an approximate formula for J_{bs} (the bootstrap current density) [19]. The plasma pressure increases towards the centre of the tokamak which means there are a greater number of faster particles on inner banana orbits (see figure 1.11b). By considering the pressure gradient between neighbouring banana orbits, a net banana current density (along the path of the trapped particles) can be shown to exist. Trapped particles exchange momentum with passing particles and J_{bs} arises from a force balance between this momentum change and an opposing frictional force due to collisions of passing particles. This gives an estimate of the bootstrap current density:

$$J_{bs} \sim \frac{\sqrt{\varepsilon}}{B_\theta} \frac{dp}{dr} \tag{1.16}$$

where $\varepsilon = r/R$ is the inverse aspect ratio (considered to be small in this approximation).

This extra current can constitute a considerable fraction of the total current, which can reduce the amount of external current drive required. A large bootstrap fraction would be advantageous in a tokamak fusion power station, as this would help to provide steady state operation. This could be achieved if 50-90% of the plasma current was provided by the bootstrap current [20].

1.4 Neoclassical tearing modes

Figure 3.2a shows a slab of plasma with sheet flux surfaces, in which the magnetic field lines lie (shown in blue). This can be thought of as a toroidal plasma that has been straightened out into a cylinder, then sliced radially down the poloidal cross section and flattened out. The top flux surface is a $q = 2$ rational surface. If a filamented current perturbation is introduced parallel to the $q = 2$ field line, an additional field component arises, perpendicular to the flux surface. The flux surface tears open, reconnecting to form a $m/n = 2/1$ magnetic island, shown in figure 3.2b. This *tearing mode* can be caused by a variety of parallel current perturbations. The key features of the associated magnetic island are its O-point, X-point and separatrix shown as a red line in figure 3.2b.

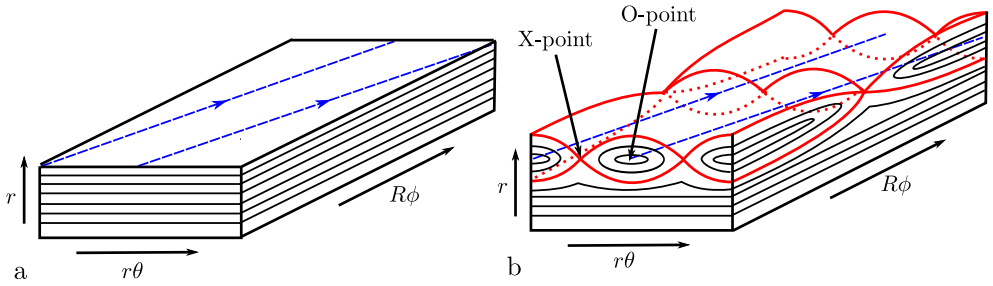

FIGURE 1.12: a) A slab of plasma. b) Slab with a magnetic island.

Figure 1.13 shows a set of toroidal flux surfaces without (left) and with (right) a $m/n = 2/1$ magnetic island along with their associated pressure profiles. Since the pressure is usually constant on a flux surface, the new island flux surfaces make a flat region in the pressure profile and reduce the central pressure, which is detrimental to tokamak performance. This flattening in the pressure profile constitutes a perturbation to the neoclassical bootstrap current, parallel to the magnetic field, which further destabilises the mode. Tearing modes driven unstable by perturbations to the bootstrap current are therefore known as neoclassical tearing modes (NTMs).

Experiments show that NTMs require a seed perturbation before they can grow. One theory is that magnetic islands smaller than a critical island width, w_c, do not completely flatten the pressure profile or perturb the bootstrap current, which leads to a threshold island width, w_{th}, above which the NTM will grow. Investigating the physics of this threshold is a key aim of this thesis.

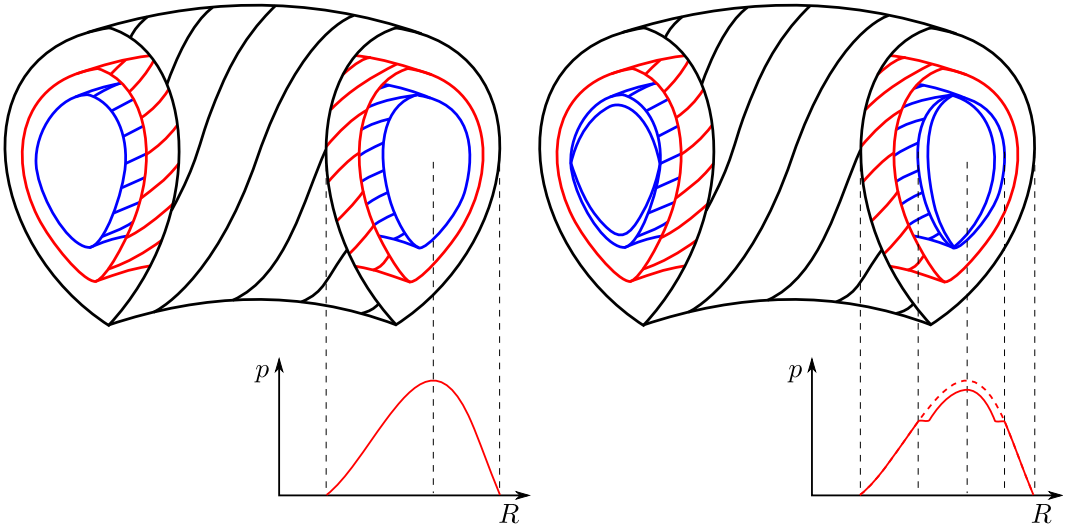

FIGURE 1.13: Left: Example tokamak flux surfaces and pressure profile. Right: With magnetic island.

Another problem caused by NTMs is that the additional field component, perpendicular to the flux surfaces, can induce eddy currents in the metal tokamak vessel and cause a drag on the rotating plasma. Large magnetic islands can completely 'lock' to the wall and cause a loss of global plasma rotation and stability. This usually results in a disruption in which the plasma's stored energy is lost to the vessel wall over a short period of time. The projected first wall energy load for a disruption on ITER is on the order of 100 MJ m^{-2} $s^{-0.5}$, whereas the limit of melting and vapourisation is on the order of 10 MJ m^{-2} $s^{-0.5}$ for the first wall materials, beryllium, carbon and tungsten [21]. As such, all feasible measures to avoid disruptions should be taken, including the avoidance and mitigation of NTMs.

Systems have been developed to stabilise and mitigate NTMs but the power required to run these systems will significantly reduce the overall efficiency of the tokamak. Figure 1.14 is a plot of power applied to the plasma by the mitigation systems against the effective Q factor, the ratio of fusion power to applied heating power for a standard ITER discharge. Points A and B are for plasmas without the mitigation system switched on, containing an $m/n = 3/2$ and 2/1 NTM, respectively. The effective Q factors of these points are reduced from an initial value of 10 to about 7 and 5 due to the confinement degradation caused by the NTM. Points C and D are for the same plasmas but with the NTMs mitigated by 10MW and 20MW of mitigation power, respectively. Though the Q factors are higher in scenarios C and D than in A and B, they are still both significantly

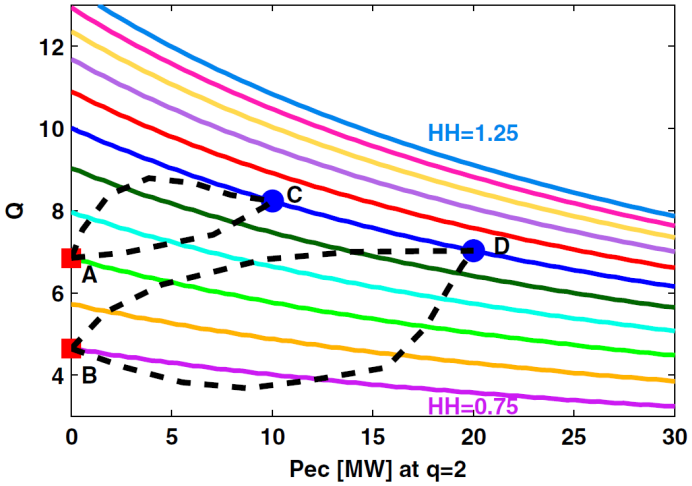

FIGURE 1.14: ITER $Q = 10$ scenarios with NTMs. **A**: 3/2 NTM, no mitigation. **B**: 2/1 NTM, no mitigation. **C**: 3/2 NTM, mitigation power=10MW. **D**: 2/1 NTM, mitigation power=20MW. [22]

below $Q = 10$. Depending on how long the mitigation system has to remain switched on, this presents the potential for a significant reduction in tokamak performance [22].

Minimising the use of these mitigation systems is clearly a priority if fusion is to be made commercially viable and this is the motivation for the thesis presented here. This thesis will make comparisons of NTM theory and experiment with the aim of providing an improved understanding of the physics of the threshold for growth, in order to inform NTM avoidance strategies on future devices.

1.5 Thesis overview

This chapter has covered the background plasma and tokamak physics required for the study of NTMs and outlined the motivation for gaining an improved understanding of this instability. Chapter 2 provides a description of the MAST tokamak and its diagnostic capabilities. A study of MAST's operational parameter space is undertaken in order to help develop the experimental scenarios used throughout this thesis, which are also described. In Chapter 3, the theoretical models for NTMs are examined and the experimental and theoretical literature is reviewed. The modified Rutherford equation (MRE) for NTM evolution is described, term by term, so that it can be used to investigate the balance of the different contributions to NTM stability later in the thesis. A heat transport equation for a magnetic island is presented in Chapter 4. The solutions

of this equation are model temperature profiles, described by a set of six free parameters, including w_c, the critical width for temperature flattening. Chapter 5 focuses on a method of measuring w_c experimentally by fitting the solutions of the heat transport model to experimental Thomson scattering data. This is the first time such a measurement has been made on a spherical tokamak. In Chapter 6, a study of the competing NTM growth mechanisms is undertaken. The evolution of the magnetic island width, evaluated from the MRE, is fitted to experimental data using a probabilistic method that takes into account the uncertainties on measured parameters. The value of w_c measured in Chapter 5 is used to help constrain these fits. The experimentally observed NTM threshold is found to agree with that predicted using the MRE. Finally, Chapter 7 concludes with a review, a summary of the previous four chapters and an outline of potential future work in this area.

Chapter 2

Experimental tools and scenarios

2.1 Introduction

This chapter describes the experimental facilities, diagnostic tools and plasma scenarios used throughout this thesis to study neoclassical tearing modes. The experimental measurements were made on the Mega Amp Spherical Tokamak (MAST); the UK's national magnetic confinement fusion experiment. Section 2.2 gives a brief overview of MAST's design and capabilities. Section 2.3 outlines a selection of MAST's diagnostics, such as the Mirnov coil array and the Thomson scattering diagnostic, which are relevant to the study of NTMs. Section 2.4 describes an investigation of MAST's operational parameter space, which was conducted in order to identify conditions suitable for NTM experiments. The chapter finishes with a description of the characteristics of the MAST scenarios analysed in this thesis.

2.2 The MAST tokamak

As a spherical tokamak (ST), MAST has a low aspect ratio of $R/a \approx 1.5$. Figure 2.1a shows a schematic cut-away of the cylindrical stainless steel vacuum vessel, which is 4.4m high and 4m in diameter. There are 24 rectangular toroidal field coils, a central solenoid and five pairs of horizontal ring-shaped coils for shaping and plasma vertical position control. All the coils are water-cooled. The vacuum vessel has an open design, with no close-fitting first wall on the outboard side of the plasma. This allows access for a wide range of plasma diagnostics, through three rings of diagnostic ports, also shown

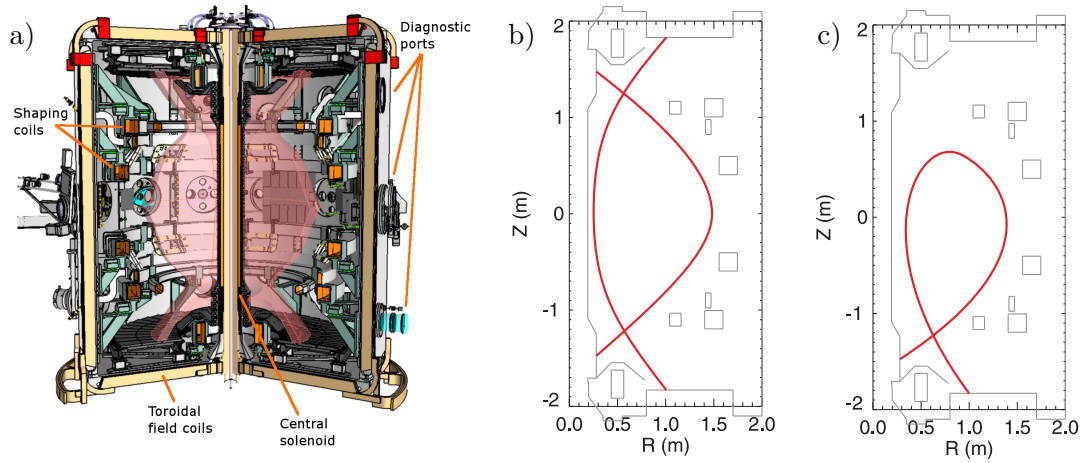

FIGURE 2.1: **a)** A schematic cut-away of the MAST vacuum vessel with toroidal field coils, central solenoid, shaping coils (also for plasma vertical position control) and three rings of diagnostic ports indicated. **b)** The Double Null Divertor (DND) configuration. **c)** The (lower) Single Null Divertor (SND) configuration.

in figure 2.1a. A selection of MAST's diagnostics are described in section 2.3. Some of MAST's key parameters are displayed in table 2.1.

Parameter	Value
Maximum plasma current (MA)	1.3
Major radius, R (m)	0.9
Minor radius, a(m)	0.6
Toroidal field (T)	0.55 (at R_0)
Maximum shot length (s)	0.7
NBI heating power (MW)	5 (2 $\times$ 2.5 MW)
Typical core T_e (keV)	0.5-1.5
Typical core n_e (m^3)	1-5 $\times$ 10^{19}
Typical core velocity (km/s)	300
Inverse aspect ratio, ϵ	0.75
Elongation, κ	$1.6 \leq \kappa \leq 2.5$
Triangularity, δ	$\delta \leq 0.5$
Record β	15%

TABLE 2.1: MAST's key parameters [23].

MAST is equipped with both an upper and a lower divertor, which allows the tokamak to operate in a number of configurations. Figures 2.1b and 2.1c show the Double Null Divertor (DND) and (lower) Single Null Divertor (SND) configurations, which are the most commonly used. Mainly DND discharges are used in this thesis as they are a more attractive operating scenario for an ST.

The plasma is heated both ohmically and by two neutral beams, providing a maximum of 2.5MW each. Conventional microwave heating, such as ECRH and ICRH are not readily applied to spherical tokamaks, which tend to operate at high density and low

outboard magnetic field making them over-dense to cyclotron radiation in the required frequency ranges. The neutral beams also provide current drive, angular momentum injection and a source of light from within the plasma due to charge exchange reactions with impurity carbon ions or line emission from injected neutral deuterium, which can be used to diagnose the plasma (see sections 2.3.4 and 2.3.5).

2.3 Diagnostics

One of MAST's strengths is its large number of plasma diagnostic systems. This section covers the key diagnostics used to measure NTMs on MAST but starts with a brief overview of the systems used to trace the time history of the different stages of a discharge, which is an important tool for interpreting NTM behaviour.

2.3.1 Basic global discharge diagnostics

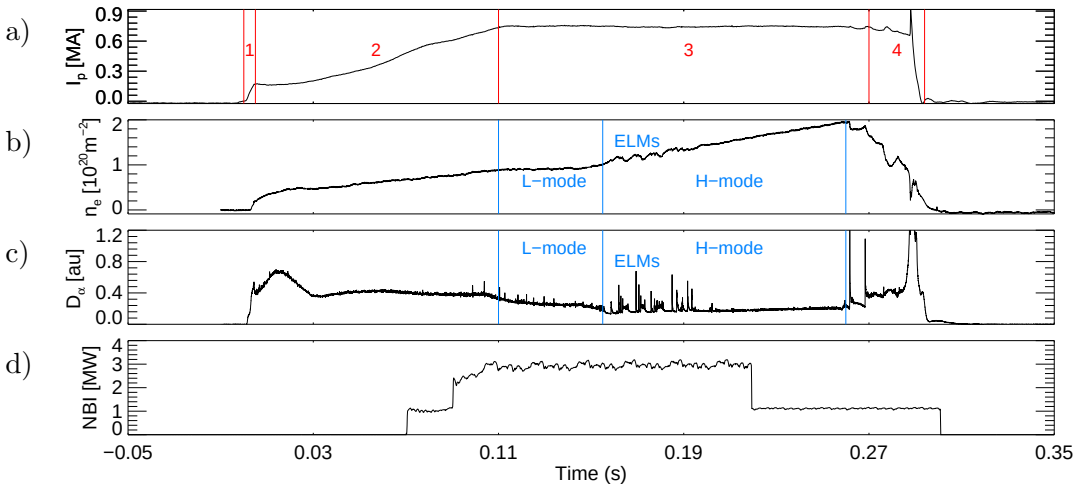

FIGURE 2.2: Time traces for MAST discharge 24081. **a)** I_p, the plasma current. **b)** Line integrated electron density, n_e. **c)** Line integrated D_α emission showing L-H and H-L transitions and ELMs. **d)** Summed power from MAST's two neutral beams

A measurement of the total plasma current, I_p shows a clear picture of the key stages of a typical MAST discharge. This is demonstrated by the upper trace shown in figure 2.2, produced using a Rogowski coil diagnostic. The stages are;

1. *Plasma breakdown.* The deuterium gas is ionised and a small plasma current begins to flow.

2. *Current ramp-up.* The plasma current is increased, mainly by ramping flux through the central solenoid.

3. *Flat top.* The plasma current is held at a constant level. By this point, the plasma has reached the required size and shape. NTMs usually occur in the second half of this stage, when the highest temperatures and densities are achieved.

4. *Termination.* Plasma confinement is lost and the discharge terminates. This may occur relatively quickly due to some large plasma instability such as a locked NTM or sawtooth crash. Alternatively, if plasma stability can be maintained, this may occur when it is no longer possible to ramp any more flux through the solenoid.

Another key diagnostic trace is the line integrated density, also shown in figure 2.2. This is provided by the interferometer, which uses the relation between the electron density integrated along a line through the plasma and the phase shift of a laser beam directed along that line. This can be used to provide 'density feedback' control in order to avoid over-fueling the plasma and also provides a useful calibration for the Thomson scattering electron density profile measurement (discussed in section 2.3.3). During the current ramp-up phase, the density gradually increases as the plasma is fueled. The rate of density increase then drops due to low confinement during the L-mode phase. At about 0.15s there is a sudden transition to H-mode and the density begins to increase rapidly. During this stage, edge localised modes (ELMs, described in Chapter 1) periodically erupt from the plasma edge and cause sharp but temporary decreases in density.

Deuterium D_α emission is line radiation that occurs in the edge plasma and SOL, where the plasma is cooler and there are more neutral particles, which can be excited by the flux of heat and particles leaving the plasma. This light is measured with a series of cameras and can be used for diagnostic purposes. If there is an improvement in confinement at the plasma edge, the measured D_α emission decreases due to the reduction in the losses of heat and particles from the plasma, which results in a reduction in excited neutrals. Similarly the emission increases if the confinement decreases. This means that L-H transitions and ELMs are also visible on the D_α trace, shown in figure 2.2. The D_α emission during the L-mode period is quite high and consistently 'fuzzy', due to characteristic filaments leaving the edge of the plasma [24]. The H-mode period is characterised either by periodic spikes in D_α emission (ELMs) or a low level of quiescent D_α emission (ELM-free or inter-ELM H-mode).

Another important trace, also shown in figure 2.2, is the NBI injected power. As MAST has only limited microwave heating capabilities, the NBI injected power is the main form of β_p control (gas puffing can also be used to control the particle density).

As it is often necessary to rapidly increase and decrease β_p during NTM experiments (see section 2.5 and Chapters 3 and 5), it is very important to monitor the NBI power. Furthermore, two important diagnostic systems make use of the light emitted when neutral particles are injected by the NBI system (see sections 2.3.4 and 2.3.5), which provides another reason for monitoring this trace.

2.3.2 Mirnov coil array

A Mirnov coil is a simple multi-turn loop of wire that measures the rate of change of magnetic field in the direction perpendicular to the plane of the loop via Faraday's law. A signal can be registered either because the field strength is varying in time or there is a spatially varying magnetic field moving relative to the coil. In the case of a magnetic island, changes in this signal come from both the rotation around the torus at about 50km/s and a slower variation due to growth of the magnetic island width on the order of 1m/s.

MAST's Mirnov coils are arranged in both poloidal and toroidal arrays of coils. The locations of the poloidal array coils, which measure B_Z, are indicated as blue circles in figure 2.3a. The coils have a high time resolution of $1.25\mu s$, limited by the digitisation rate of the analogue-to-digital converter (ADC), and can provide spatial and spectral information about rotating MHD activity in a tokamak plasma. It is possible to identify the toroidal and poloidal mode number of a particular mode by using a combination of several spatially separated Mirnov coils, which can help to distinguish between different modes and localise them to specific rational surfaces. For example, a simple way of identifying modes with n equal to an odd number is to subtract the signals of two coils separated by a toroidal angle of $\phi = \pi$. Figures 2.3b, 2.3c and 2.3d show Mirnov coil data for a 2/1 NTM located on the $q = 2$ surface, shown as a red line on 2.3a.

Figures 2.3b shows the NTM data on a magnetic island width evolution timescale (determined by resistive diffusion) and 2.3c shows the same data over a single island rotation period (at a time indicated by the red line on figure 2.3b). The two timescales differ by approximately two orders of magnitude, which allows the assumption that the magnetic island structure does not change during a single rotation period. By using this assumption, identifying this mode as having an $n = 1$ structure and measuring the mode rotation frequency, it is possible to transform the temporal Mirnov data into spatial data in the ϕ direction, as shown in figure 2.3d. This figure shows data from the

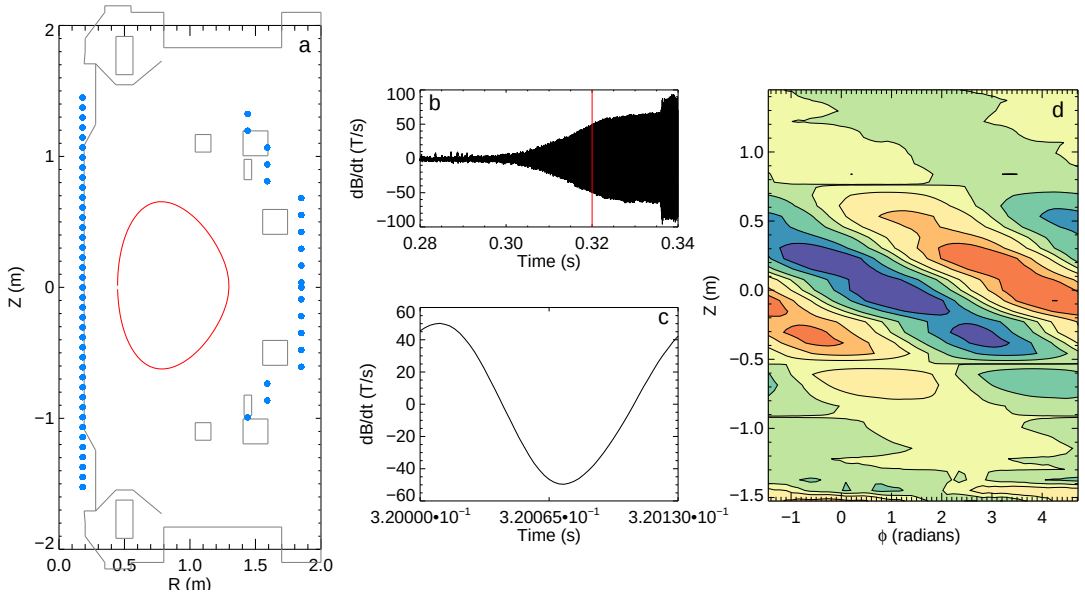

FIGURE 2.3: MAST Mirnov coil data for discharge 23447. **a)** Locations of the poloidal array of Mirnov coils (blue dots) relative to the $q = 2$ surface location (red line). **b)** Data from a Mirnov coil over island growth timescales (0.01s). Red line shows the time used for figure c. **c)** Data from the same Mirnov coil as figure b over island rotation timescales (0.1ms). **d)** Data from the inboard poloidal Mirnov coil array over the same timescale as figure c.

whole inboard Mirnov array (the vertical line of coils on the centre column, or left hand side of figure 2.3a) and reveals the spatial structure of the instability.

A variety of plasma instabilities, such as NTMs, ideal MHD modes and chirping fast particle modes, can be identified by their characteristic time traces on a Fourier transform spectrogram of a Mirnov coil signal (see figure 2.4). MAST's neutral beams create a population of fast particles that often gives rise to instabilities known as fishbones, which chirp down in frequency as they lose energy. Figure 2.4 shows how chirping fishbones can drive another mode unstable; the ideal $n = 1$ Long-Lived Mode (LLM) [25]. The LLM has only been observed on MAST although ideal modes with similar characteristics have been observed on the spherical tokamak, NSTX [26]. This mode is often present simultaneously with 2/1 NTMs on MAST and can alter the rotation profile (see section 2.5).

Mirnov coils provide a useful source of information on a number of other key parameters. For example, it is possible to obtain some information about the magnetic island width from Mirnov coil data by making certain assumptions about the magnetic island structure, the perturbed current and the additional Mirnov signal due to eddy currents in the vessel wall. A method for doing this is discussed in Chapter 6. Also,

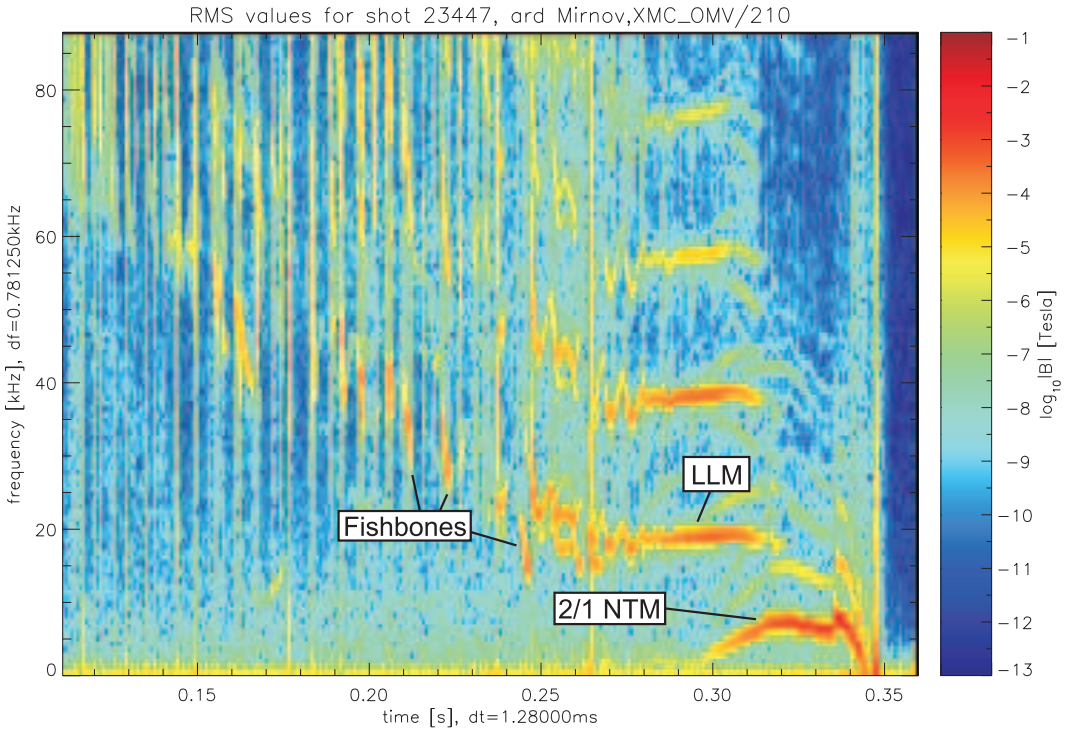

FIGURE 2.4: Running Fourier transform spectrogram from a Mirnov coil for discharge 23447. Plasma instabilities indicated.

when combined with plasma flow velocity diagnostics (see section 2.3.4) this information can be used to work out if there is a difference in rotation frequency between the magnetic island and the plasma at the rational surface, which can have implications for NTM stability (see Chapter 3).

2.3.3 Thomson Scattering (TS)

Thomson scattering is the elastic scattering of electromagnetic radiation by charged particles, discovered by J. J. Thomson in 1906 [27]. The scattering can either be coherent or incoherent, depending on the size of the Debye length relative to the scattering **k** vector (which depends on the angle of observation and the radiation wavelength). If the Debye length is short and collective behaviour is important, the Thomson scattering will be coherent. If the Debye length is large relative to **k** and the radiation scatters off individual particles, as is generally the case in MCF plasmas, then the Thomson scattering will be incoherent. The electric field of the incident radiation causes the charged particle to oscillate and emit radiation at the same frequency as the incident radiation. The resulting dipole radiation is polarised along the direction of the particle's oscillating motion and is strongest in the direction perpendicular to the plane of oscillation. By measuring the spectrum of the scattered light, and comparing it to a theoretical

spectrum, information about the plasma in the scattering volume can be obtained. The theoretical spectrum can be derived by considering the motion of individual particles, including relativistic effects, which become significant over a temperature of 1-10keV. The two main parameters that can be obtained are the particle temperature, which is a function of the spectrum width (through Doppler broadening) and the particle density, which is a function of the area under the spectrum (the emission increases with the number of particles in the scattering volume).

In fusion plasma diagnostics, this incident radiation comes from a well characterised external laser and scatters off electrons. The temperature and density are perhaps the most important parameters in determining fusion success and the Thomson scattering diagnostic plays a key role due to the relative simplicity of its data interpretation, its reliability and its lack of dependence on other measurements. This importance was demonstrated in 1968 when a team of British physicists transported a Thomson scattering system to measure the temperature in the T3 tokamak in Moscow. The maximum measured temperature of 1keV was record breaking at the time and established the tokamak as the most promising MCF configuration.

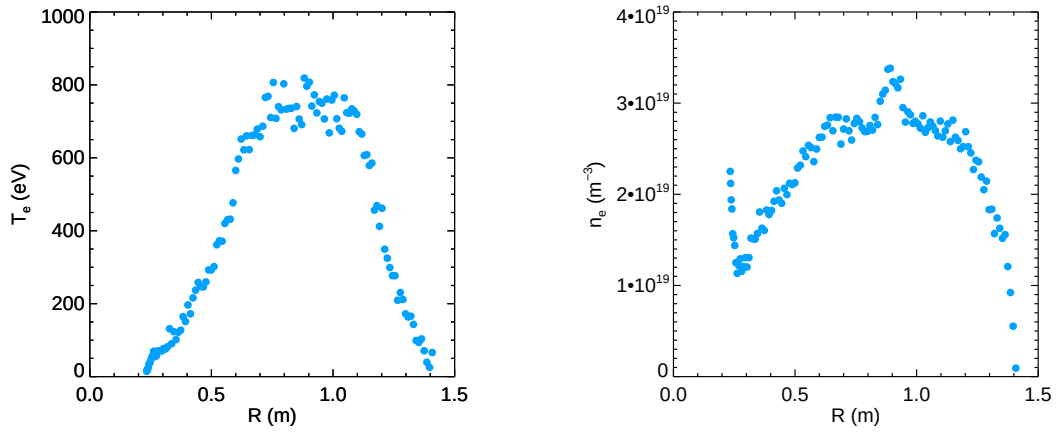

FIGURE 2.5: Thomson scattering T_e and n_e profiles for a MAST standard ohmic discharge 26945.

The MAST Thomson scattering diagnostic provides high spatial (∼1cm) and temporal (>240Hz) resolution T_e and n_e profiles (n_e normally calibrated against the line-integrated interferometer measurement). MAST's electron temperature tends not to exceed 2keV, so though relativistic effects are included in the diagnostic analysis, they are generally small for the MAST plasmas considered in this thesis (though they are significant for hotter tokamaks, such as JET). Core electron densities are typically

$\approx 1 - 5 \times 10^{19} m^{-3}$. Figure 2.5 shows example T_e and n_e profiles for a MAST standard ohmic discharge. The increased density towards the inboard edge is due to the location of the inboard fueling valve.

The main system consists of eight 30Hz 1.6J Nd:YAG lasers fired along approximately the same beam line into a beam dump and a set of collection optics covering 130 spatial points across a full range of major radii within the plasma [28] (see figure 2.6). From the collection optics, the light is guided to 130 polychromators, which each measure the Thomson scattering spectrum over five spectral channels. Figure 2.7 shows a cartoon plan view of MAST with the beam line in red, tangential to the central column, and the viewing angle of the collection optics in green. The separation of the spatial points tangentially, δr_{tan}, projected onto the tokamak major radius gives a better radial resolution, δr_{rad}, on the inboard side than on the outboard side (also illustrated in figure 2.7).

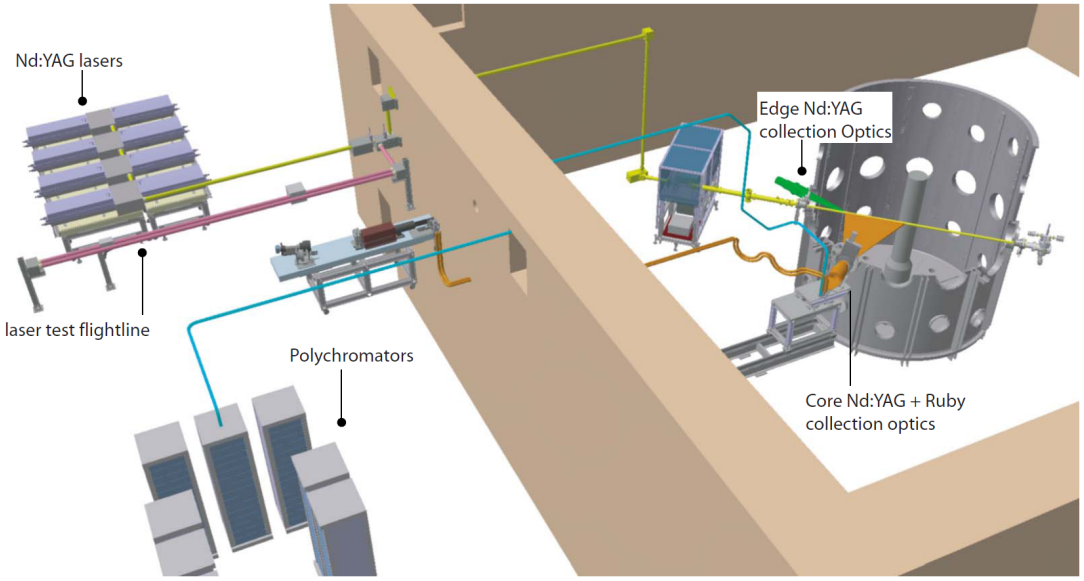

FIGURE 2.6: A schematic diagram of the MAST TS system. [28]

The scattering volume has a sub-cm width and, as the instrument functions for individual spatial points do not overlap at the radii considered in this thesis (typically $R = 0.3 - 0.5$m), the emission is assumed to come from a point source. A secondary set of collection optics allows investigation into phenomena at the plasma edge, but this system will not be considered here. There is also a single ruby laser with 240 spatial points providing a higher spatial resolution but this is only able to fire once per discharge.

The Nd:YAG system can operate with a large range of laser time spacings. For NTM studies, it is usually operated in one of two temporal modes. In continuous mode the

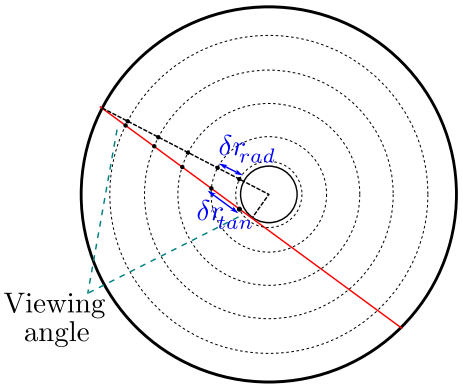

FIGURE 2.7: A cartoon plan view of the MAST TS system. The red line indicates the tangential laser beam line. The dashed green lines indicate the collection optics viewing angle. The black dots and black dashed line illustrate the projection of the spatial points onto the tokamak major radius. The radial resolution is better on the inboard than the outboard side.

eight lasers are spaced equally in time, with ∼4ms between each laser, which is beneficial for constraining the plasma equilibrium at regular intervals. In burst mode the eight lasers are temporally bunched together in bursts, each separated by 33ms. This is useful for measuring fast phenomena, such as the L-H transition or an NTM rotating around the torus. Figure 2.8 shows these two temporal modes in operation while an NTM is present in the plasma.

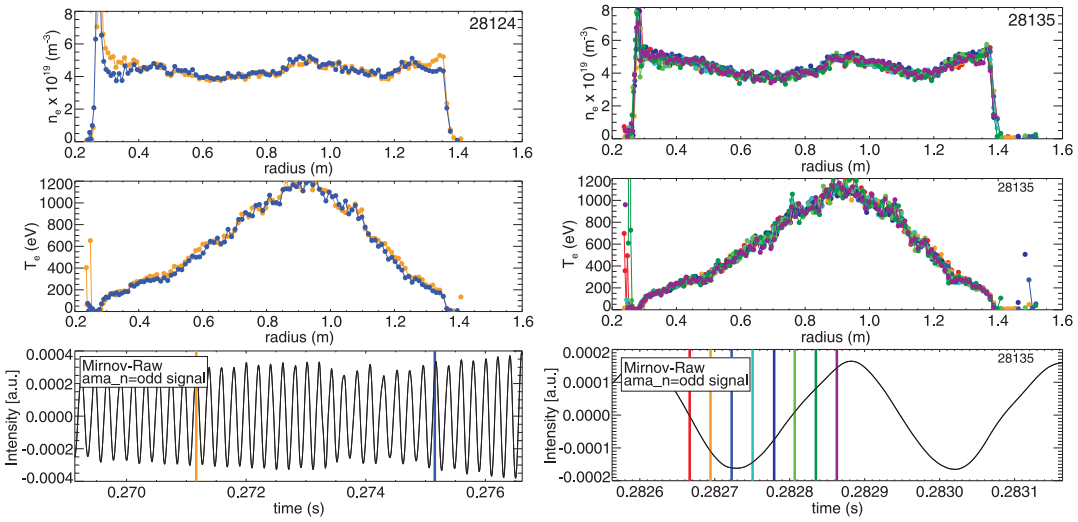

FIGURE 2.8: TS temporal modes. *Top*: n_e profiles. *Middle*: T_e profiles. *Bottom*: Mirnov time trace with color coded TS time slices indicated as vertical lines. *Left*: Continuous mode. *Right*: Burst mode.

2.3.3.1 TS triggering

A real-time triggering system has been developed so that the TS lasers can be fired at specific times, such as stages of an NTM's evolution or points of its transit around the torus [23]. The system uses a Mirnov coil on the midplane to detect the frequency, phase and magnetic amplitude of the NTM in real-time. A Hilbert transform is used so that continuous phase information can be gathered if the rotation frequency changes during a single period of oscillation.

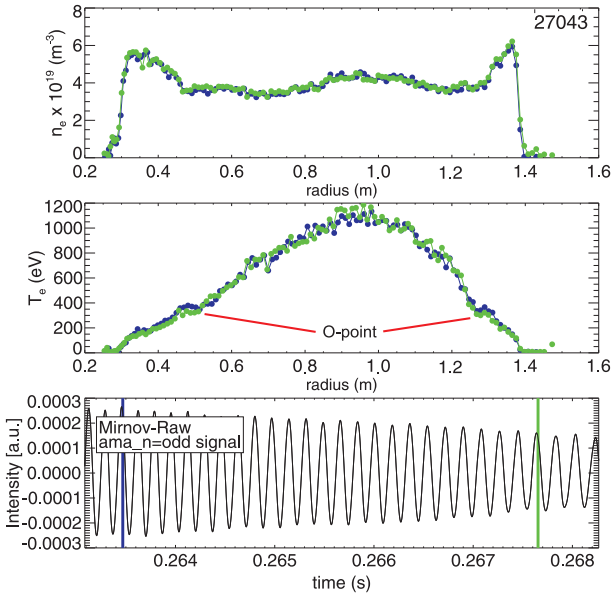

FIGURE 2.9: TS profiles from triggered measurements. The triggering system is set to fire the TS lasers across the magnetic island O-point. The flat regions, which can be seen in the T_e plot (middle) indicate the two magnetic island cross sections which cut across the poloidal plane for this $m = 2$ mode.

There are two TS triggering options available. The first makes use of continuous mode, making small adjustments to the laser's fire time so that it locks to a particular phase of the NTM. The phase is continually monitored by the triggering unit but there is a delay of around 400μs in calculating the phase and firing the lasers so that this method only works if the frequency does not vary significantly over a couple of oscillation periods. For example, the system can be set to a phase of π, triggering the lasers on the island O-point and obtaining a series of measurements of the width of the island temperature flattening (see figure 2.9).

The second option is to trigger a burst of lasers on a particular NTM magnetic amplitude for either a growing or shrinking magnetic island. First of all the triggering unit detects the presence of an NTM when the Mirnov amplitude reaches a certain threshold, which arms the TS lasers. The unit then tracks the island amplitude and

whether it is growing or shrinking and fires the laser burst at the desired point, which provides a 2D temperature profile of the magnetic island at that particular amplitude.

The measurement of NTMs with the Thomson scattering system is a key part of this thesis and is discussed in more detail in Chapters 5 and 6.

2.3.4 Charge Exchange Recombination Spectroscopy (CXRS)

Neutral deuterium atoms injected by the NBI system undergo charge exchange reactions with the impurity carbon C^{6+} ions to produce C^{5+} ions, which emit a characteristic spectrum of light. The Doppler broadening of a particular peak in the spectrum gives the temperature of the C ions and the Doppler shift gives their velocity. It is often assumed that the energy transfer between C ions and D ions occurs on a faster time scale than the energy confinement and so the temperature and velocity can be taken to be the same. In some circumstances the differences between the main ion and impurity ion species can be important [29], but a full discussion of these effects is beyond the scope of thesis.

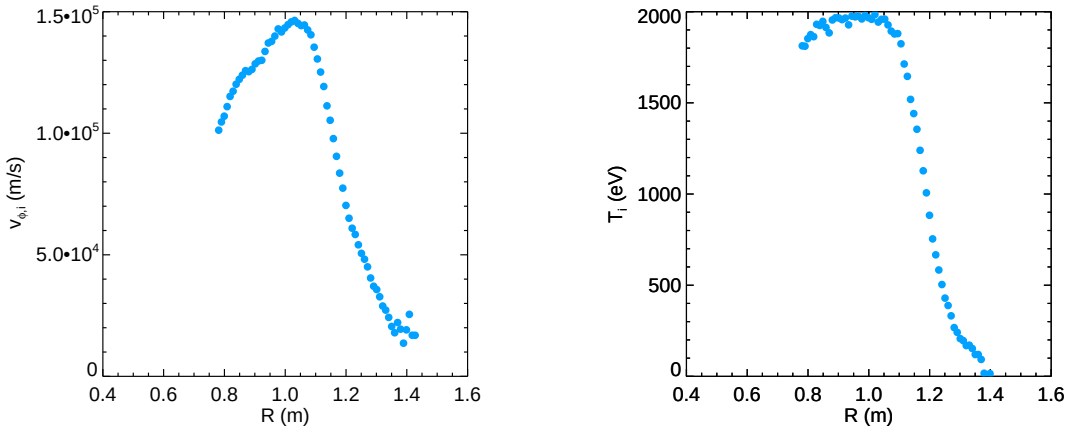

FIGURE 2.10: CXRS v_i and T_i profiles for an NBI heated MAST discharge 23447 in ELM-free H-mode.

As these reactions and emission of light occur in a localised volume, looking along a line of sight that intersects the neutral beam line can provide a localised emission measurement, which allows the construction of v_i and T_i profiles. The MAST CXRS system has a spatial resolution of ∼1cm over a range $R = 0.8 - 1.4$m and a temporal resolution of 5ms [30]. These measurements are clearly not possible if the NBI system is not injecting neutral deuterium. Similarly, if the beam voltages are too low, the amount

of emitted light will be too low to infer a reliable measurement. Figure 2.10 shows example v_i and T_i profiles.

The v_i profile can be converted to a toroidal rotation frequency profile by the simple formula $f = v_\phi/2\pi R$. If the radial location of an NTM can be determined, it is possible to compare the rotation frequency at this point to the rotation frequency of the magnetic island, as measured by the Mirnov coil array. Section 2.5 covers the phenomenology of the typical discharges used in this thesis and includes a plot comparing these two frequencies.

2.3.5 EFIT

In Chapter 1 the concept of plasma force balance was introduced. If the plasma is in equilibrium, it is possible to calculate the balance of forces contributing to that equilibrium and to reconstruct the magnetic flux surfaces. Most models of plasma stability and transport require knowledge of flux surface locations and the associated q profiles to calculate many of their key results, so finding the locations of the surfaces experimentally allows these models to be tested. Calculating the equilibrium force balance is commonly done using an equilibrium code. On MAST, the EFIT code is used to calculate the equilibrium, making use of extra information from a range of diagnostics to help constrain the results.

The equilibrium is primarily dependent on the balance of three spatially varying parameters; the magnetic flux due to the poloidal field, Ψ, the toroidal field function, $f = RB_\phi$ and the total pressure, p. The equilibrium force balance equation, $\nabla p = \mathbf{J} \times \mathbf{B}$, can be written in terms of Ψ, p and f. The dimensionality can be reduced by assuming toroidal axisymmetry and treating p and f as poloidal flux functions. In this form it is known as the *Grad Shafranov equation* (equation 2.1).

$$R\frac{\partial}{\partial R}\left[\frac{1}{R}\frac{\partial \Psi}{\partial R}\right] + \frac{\partial^2 \Psi}{\partial Z^2} = -\mu_0 R^2 \frac{\partial p}{\partial \Psi} - f\frac{\partial f}{\partial \Psi} \tag{2.1}$$

The EFIT code solves this equation to fully reconstruct the equilibrium magnetic field, current and pressure profiles, usually assuming that the profiles are described by a set of polynomial basis functions. There are often significant uncertainties, but if measurements of the plasma edge location, the externally applied magnetic field, the pressure profile and current density profile can be made, it is possible to find a well constrained solution. A version of EFIT, called EFIT++, allows the introduction

of such experimentally measured parameter values and usually produces more reliable results. On MAST, the current density profile can be inferred using the Motional Stark Effect (MSE) diagnostic, which uses the polarisation of certain light from NBI particle interactions to reveal the pitch of the magnetic field. This is also often used as a constraint in EFIT++. EFIT also calculates the time evolution of various useful global parameters such as β_p (shown in figure 2.2) and the magnetic axis position. Typical EFIT ouput for MAST is plotted in figure 2.11.

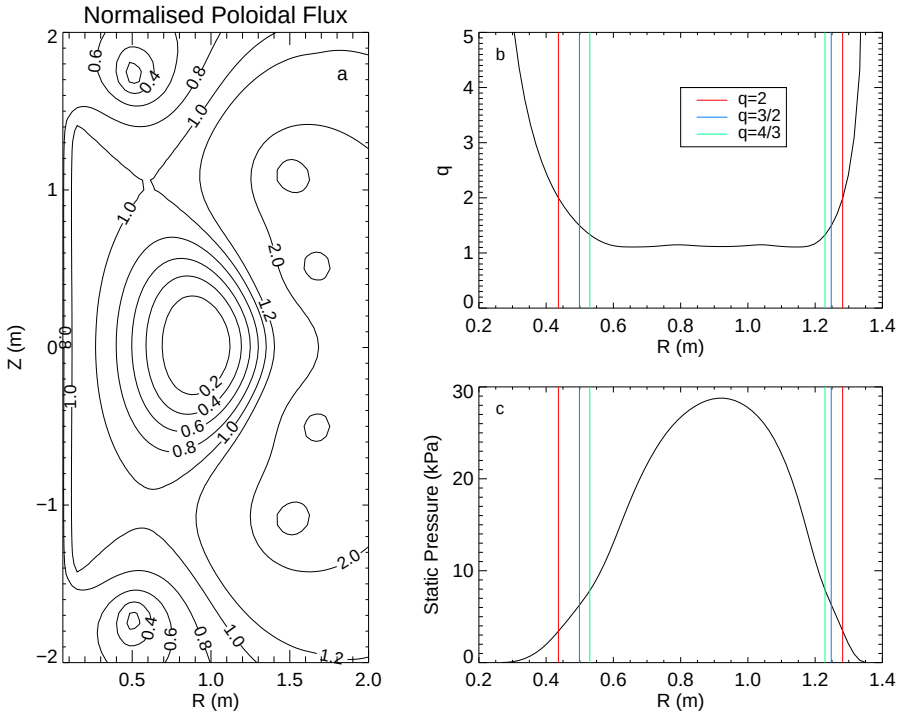

FIGURE 2.11: MAST discharge 23447. **a**) The reconstructed, normalised poloidal flux $\Psi_n = (\Psi - \Psi_{axis})/(\Psi_{boundary} - \Psi_{axis})$. **b**) The reconstructed q profile with various rational surfaces indicated. **c**) The reconstructed p profile with various rational surfaces indicated.

When studying NTMs, it is sometimes of interest to switch between real space and flux space coordinates. For radial locations around $m/n = 2/1$ magnetic islands, which are the main subject of this thesis, it is approximately the case that $\Psi(r) \propto r$ so this transform is usually made using a constant factor for the inboard side and another factor for the outboard side.

2.4 NTM occurrence in the MAST operational parameter space

NTMs occur regularly on MAST and can often cause plasma disruptions if they lock to the vessel wall. NTMs with mode number $m/n = 2/1$ are common and usually have a large amplitude, growing to a typical saturated size of $W \approx 10$cm (about 20% of the minor radius). The 2/1 mode is the focus of this thesis, partly due to its regular occurrence and partly due to its large saturated size, which makes it easier to measure using the TS system. Other mode number NTMs, such as 3/2 and 4/3, do occur and will be discussed in more detail in Chapter 6. As was mentioned in Chapter 1, NTMs usually need a seed island, caused by some kind of triggering perturbation, but in some cases apparently 'triggerless' NTMs can grow. The NTMs examined in this thesis are thought to be triggerless and possible mechanisms to explain their growth are described in Chapter 3.

In order to identify the optimum MAST scenarios for studying NTMs, an investigation into the MAST operational parameter space has been conducted. Data-mining several key tokamak parameters over a large number of discharges has made it possible to examine their achievable values in a MAST plasma. The following parameters were considered; β_N, β_p, l_i, q_0 (the q value at $\Psi_n = 0$), q_{95} (the q value at $\Psi_n = 0.95$), n_e/n_{Grwld} (where $n_{Grwld} = \frac{I_p}{\pi a^2} \times 10^{20}$ is the Greenwald density limit, above which the plasma usually terminates [31]), δ (the triangularity), κ (the elongation) and the Z position of the magnetic axis. A database has been constructed by examining 6300 consecutive discharges, retaining only those discharges that reach plasma current 'flat top', splitting the discharge time history into 10ms slices and retaining only those time slices which occur during the plasma current 'flat top' stage of the discharge. For each time slice, the parameters listed above are entered into the database and an algorithm is run to decide whether a 2/1 NTM is present or not (based on Mirnov amplitude and typical rotation frequency range). Using a Mirnov coil signal, the magnetic island width was then estimated (the method for doing this is described in Chapter 6). The results are plotted in figure 2.12.

Figure 2.12 shows contour plots of MAST discharge time slices in different cross sections of the parameter space. White space indicates regions of parameter space that were not accessed in the existing MAST database, black space indicates regions that MAST has accessed but where the likelihood of a 2/1 NTM growing is negligible and

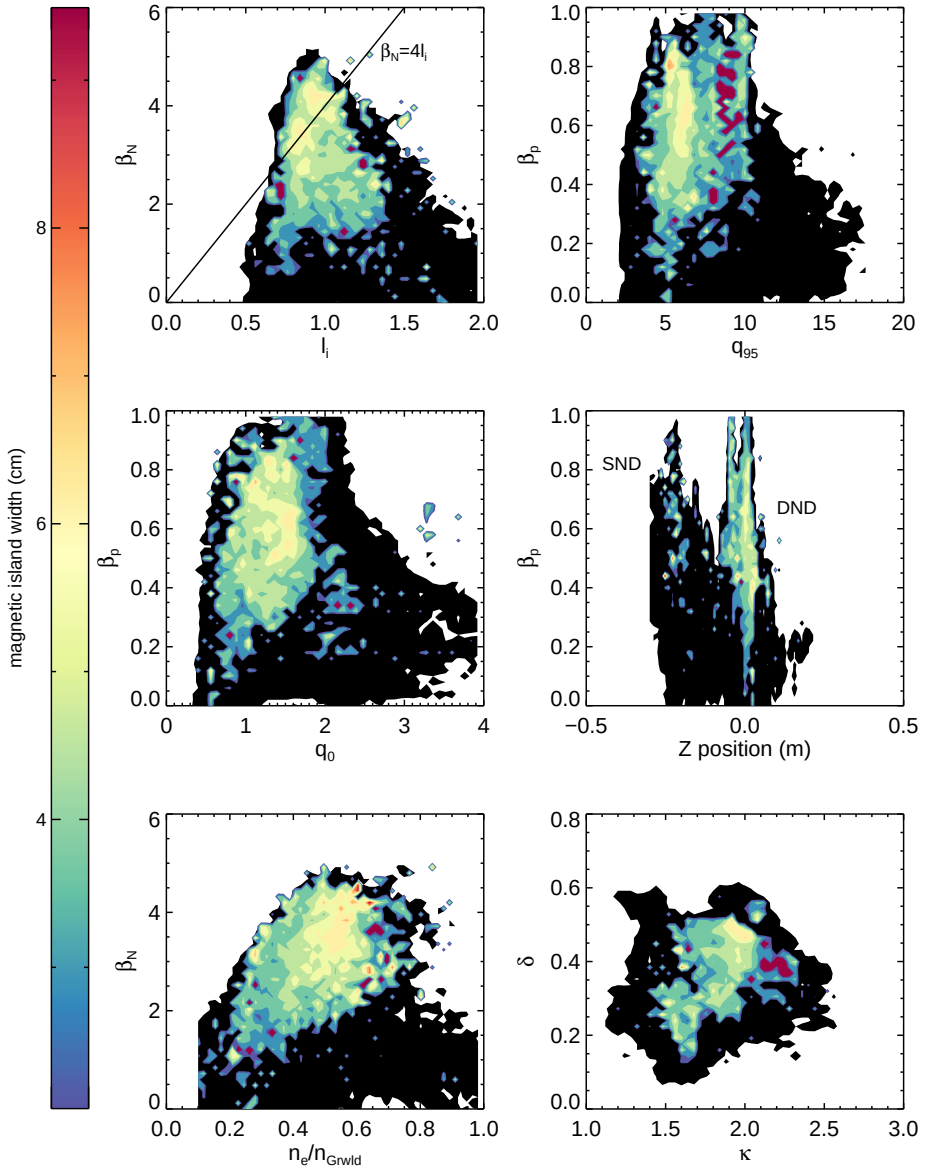

FIGURE 2.12: Database of MAST discharges with NTM magnetic island width superimposed. White space indicates regions of parameter space that were not accessed in the existing database, black space indicates regions that MAST can access but where the likelihood of a 2/1 NTM growing is negligible and the colour contour region indicates the average magnetic island width of an NTM if it occurs at that point in parameter space.

the colour contour region indicates the average magnetic island width of an NTM if it occurs at that point in parameter space. As the plotted island width is a binned average, the maximum width on most of the plots is around 6-7cm but it is worth noting that island widths of up to 10 or 12 cm are possible. The plot of β_N against l_i also has a black line indicating the approximate ideal β_N limit of $4l_i$. From this plot it is clear that the largest NTMs occur close to the ideal limit (a potential reason for this is explained in Chapter 3). Another trend illustrated by a number of these plots, is that large magnetic

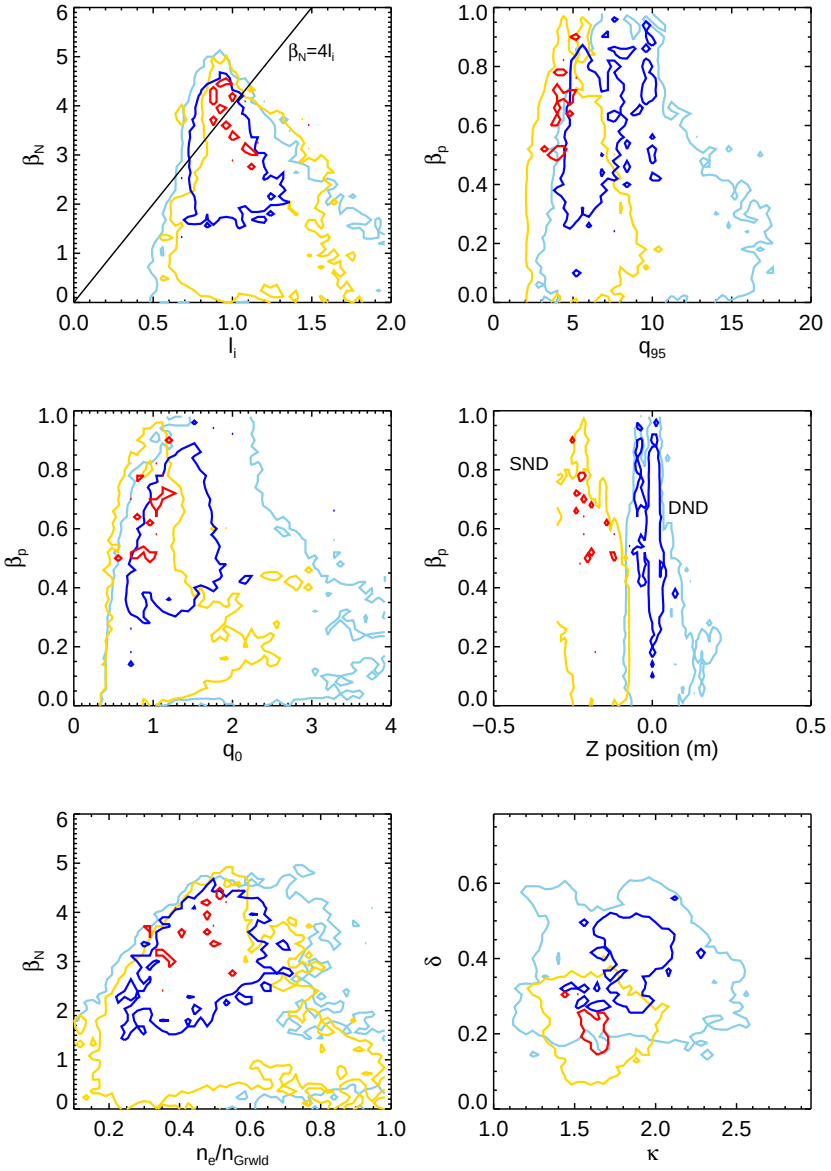

FIGURE 2.13: Database of MAST discharges. Space within the pale blue line indicates a DND discharge. Space within a dark blue line indicates a DND discharge with a 2/1 NTM. Space within the yellow line indicates an SND discharge. Space within a red line indicates an SND discharge with a 2/1 NTM.

island formation seems to be more sensitive to the current profile through l_i, q_0 and q_{95} than the pressure through parameters β_N and β_p. In this case, a high level of sensitivity to a particular parameter is heuristically characterised by the large island width region being constrained to a narrow range of values for that parameter. The values $q_0 \approx 1$ and $q_{95} \approx 5$ are most favourable to the growth of large 2/1 magnetic islands. It should be noted that large magnetic island formation is also relatively sensitive to n_e/n_{Grwld}. Both the diffusion of the current profile towards $q_0 \approx 1$ and $q_{95} \approx 5$ and the increase in density towards the Greenwald limit tend to occur towards the end of a discharge, so

the effects are correlated and it is a challenge to isolate these sensitivities and deduce which is the most important.

Another point of interest in figure 2.12 is the plot of β_p against magnetic axis Z position, which shows that DND discharges are more likely to have large NTMs than SND discharges. The effect of SND plasmas being lower in the vessel and therefore slightly further away from the Mirnov array has been investigated but this cannot explain the difference. In figure 2.13, figure 2.12 is replotted with a focus on the differences in the DND and SND NTM populations. One potential explanation for this is that the lower magnetic axis position of SND plasmas leads to the peak NBI current drive being shifted off-axis. This off-axis current drive could lead to an increase in magnetic shear at the $q = 2$ surface, which would reduce the likelihood of NTM growth, although conclusive evidence of this effect is yet to be found.

2.5 Phenomenology of discharges used in this thesis

Though tokamak scenarios are usually theoretically planned, they are rarely executed perfectly and some experimental development of scenarios is normally required. This section provides an overview of the properties and phenomena observed in the typical discharges used in this thesis. Some of these phenomena, though not well understood, must be described in order to account for the resulting NTM behaviour. However, a detailed investigation of all of the plasma conditions is beyond the scope of the thesis.

As was demonstrated in section 2.4, the likelihood of an NTM growing increases with the plasma β (this is more fully explained in Chapter 3). For this reason, discharges used in this thesis usually aim to achieve as high β as possible, using a high NBI power input of $>$ 3MW and a high level of fueling to increase the plasma density.

Profiles and time traces from discharge 23447, a typical example, are shown in figure 2.14. There are several important features in these plots that may be related to or may influence NTM behaviour:

1. There is a tendency for the q profiles in these discharges to have reversed shear towards the core but this usually becomes less pronounced later in the discharge, ending with very broad, almost flat profiles. It is thought that the steep temperature gradients (resembling an internal transport barrier), the very strong flow shear (which could reduce turbulent transport) and reversed magnetic shear at 0.2s are

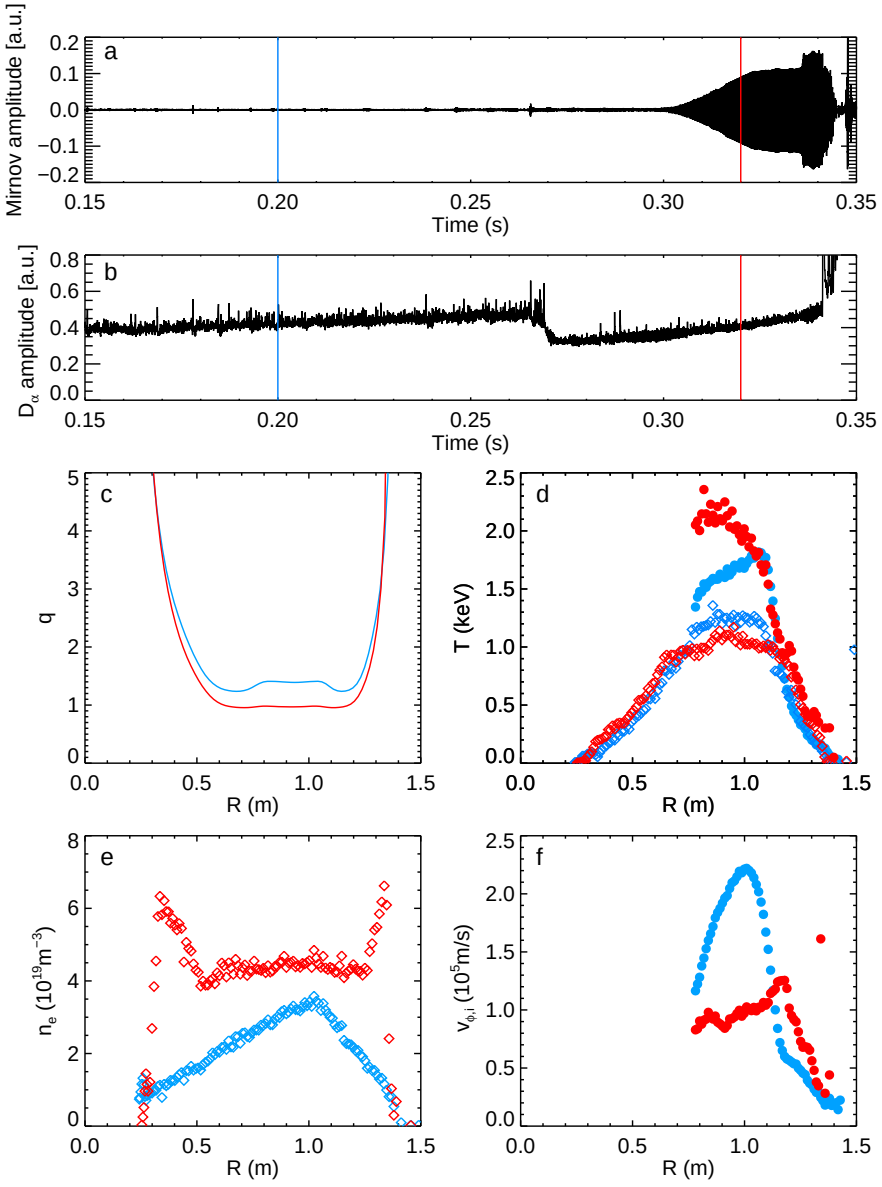

FIGURE 2.14: Example profiles and time traces for typical high β NTM discharge, 23447. Blue indicates the time slice at 0.2s. Red indicates the time slice at 0.31s. **a**) $n = 1$ Mirnov amplitude. A 2/1 NTM grows at about 0.29s. **b**) Line integrated D_α emission. L-H transition is at 0.27s. **c**) EFIT++ q profiles. **d**) TS T_e profiles (diamonds) and CXRS T_i profiles (circles). **e**) TS n_e profiles. **f**) CXRS v_i profiles.

all associated and that this is approaching a so-called 'advanced' tokamak scenario with a significant bootstrap current at the location of the strong gradients. This effect is reduced later as the flow shear is lost and the density profile flattens.

2. T_e and T_i differ significantly in the core due to the NBI heating. An explanation of the difference between these temperatures would require an energy balance calculation, taking into account the NBI particle slowing down time, the confinement times of the different species and the effect of any fast particle or micro-instabilities

that can redistribute their energy. This is beyond the scope of this thesis. However, in the region close to the $q = 2$ surface ($R \approx 0.45m$ and $R \approx 1.3m$), which is the region of interest for this thesis, both temperatures and their gradients are similar and it is therefore assumed that $T_i = T_e$. Neither T_i nor T_e changes significantly between L-mode and H-mode, other than a small temperature pedestal being formed.

3. At 0.2s, the plasma is in L-mode and the electron density gradient, $\frac{dn_e}{dr}$ is negative across the profile. However, at 0.31 when the plasma is in H-mode, the edge confinement increases significantly and there is an accumulation of electrons close to the plasma edge; so-called 'edge density ears', which are commonly observed in MAST H-mode discharges. These ears are thought to be due to an accumulation of impurity carbon ions but conclusive evidence for this is yet to be found. This type of density profile is unusual in a tokamak and is likely to influence the bootstrap current in that region.

4. v_i drops significantly in the core as the discharge progresses but momentum is transferred outwards causing v_i to increase around the $q = 2$ surface and towards the plasma edge. There is some evidence that a potential mechanism for this momentum transfer is toroidal coupling between an $n = 1$ LLM in the core and the $n = 1$ NTM at the $q = 2$ surface, although the LLM is not always present when this is observed. Figure 2.15 illustrates this phenomenon in more detail.

Figure 2.15 shows a Mirnov spectrogram with CXRS plasma rotation data overplotted. The upper CXRS line follows the point in the profile with the maximum rotation frequency, f_{max}. This decreases in line with the fishbone instabilities, which also chirp down in frequency. At about 0.28s the fishbones drive a LLM unstable, which follows the same constant frequency as f_{max}. Shortly after this, a 2/1 NTM grows with no obvious triggering perturbation, initially at a slower frequency than the $q = 2$ plasma rotation frequency (this is a common feature of the triggerless NTMs observed on MAST). As the NTM grows it reaches the same frequency as the $q = 2$ plasma rotation frequency. Then the LLM rotation begins to slow and the NTM rotation simultaneously speeds up; momentum seems to be magnetically transferred from the LLM to the NTM. By the time the NTM has reached its saturated size, the LLM has disappeared.

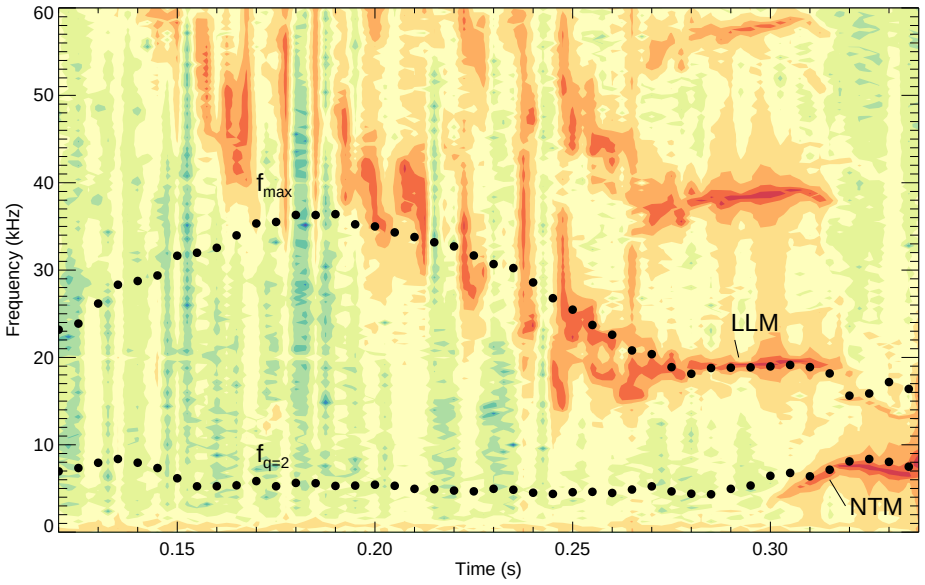

FIGURE 2.15: Comparison of CXRS plasma rotation data and Mirnov MHD rotation data for discharge 23447. The colour contour is a Mirnov spectrogram for an outboard, midplane Mirnov coil. The black dots are the time evolution of the maximum of the CXRS rotation frequency profile and the rotation frequency at the $q = 2$ surface.

2.5.1 β ramp-down discharges

For the NTM stability studies conducted in Chapter 6, it was necessary to find a scenario where the β is decreased while an NTM is present. This so-called 'β ramp-down' scenario, which is explained in more detail in Chapters 3 and 6, allows the behaviour of a shrinking NTM magnetic island to be investigated, as the saturated island width is roughly proportional to β_p. This is a difficult scenario for MAST to achieve for a number of reasons. Firstly, due to the amount of flux available in the central solenoid, MAST pulses are relatively short compared to those in other tokamaks and it can take a significant fraction of the discharge length to reach the β required to generate an NTM. In a β ramp-down scenario, the β then has to be reduced by removing the NBI power, as this is the only easily controlled heating input available in these discharges. It can take around 100ms for the β to drop sufficiently so, if this is to happen before the end of the discharge, it is necessary to initially increase the β as quickly as possible, using gas-puff fueling and NBI heating, in order to drive an NTM unstable .

Furthermore, when removing the NBI power, the plasma rotation is also reduced, which can lead to mode-locking and disruption if there is a large 2/1 NTM present. Some NBI systems used on other tokamaks are capable of versatile real-time power and rotation control, but power control capabilities are not sufficiently well developed to

implement this on MAST. Furthermore, stepping the NBI power down gradually, one beam at a time, does not allow the β to drop quickly enough for the magnetic island to disappear before the end of the discharge. It was therefore necessary to find the optimum NBI 'turn-off' time for both beams that allowed the β to rise and fall sufficiently quickly without reducing the rotation too early. Fortuitously, this was assisted by momentum transfer phenomenon (possibly assisted by the 1/1 mode) described above, which appeared to keep the $q = 2$ surface rotating even after the NBI system has been removed.

The discharges used in this thesis are a mixture of β ramp-downs and discharges where the NBI remains switched on until the plasma disrupts, but most of the features described in section 2.5 are common to both. In Chapters 5 and 6, data from these discharges are analysed and the influence of these phenomena on NTM behaviour are considered.

2.6 Summary

This chapter has provided a brief overview of the MAST tokamak. This included a description of some of MAST's many diagnostic systems, with a focus on those systems important to the study of NTMs and those used for plasma equilibrium and discharge monitoring. An introduction to the behaviour of NTMs on MAST was also presented, including an investigation into the parameter regimes in which NTMs are most likely to grow. Details of the time evolution and typical profiles of the discharges used throughout this thesis were also presented. Further physics, necessary to understand this behaviour in more detail, is discussed in Chapter 3. In Chapters 4 and 5, the Thomson scattering diagnostic is used to probe the structure of NTM magnetic islands on MAST. Chapter 6 describes an analysis of the time evolution of NTMs on MAST using data from the diagnostics discussed in this chapter.

Chapter 3

An introduction to neoclassical tearing modes

3.1 Introduction

This chapter gives an overview of the theory of neoclassical tearing modes (NTMs) and notable experimental observations of their behaviour in tokamaks. The formation of the magnetic island associated with the NTM and the various stabilising and destabilising contributions that can exist in a tokamak are considered. Section 3.2 covers the classical tearing mode theory developed by Rutherford over 40 years ago. The subsequent sections describe a number of modifications that have been added to Rutherford's theory since then. The result is the modified Rutherford equation, which describes the balance of stabilising and destablising terms that govern the evolution of the magnetic island width.

3.1.1 Magnetic islands

A magnetic island can form around a filamented current perturbation in a region susceptible to magnetic reconnection, such as the sheet current shown in figure 3.1. The current filament generates an encircling magnetic field, given by Ampère's law, which causes the equilibrium field lines to reconnect in a new topology. There are a variety of possible mechanisms that can provide such a current perturbation and cause a magnetic island to grow. This chapter considers those mechanisms important to tokamaks.

In a tokamak, a magnetic island can grow on a rational surface where field lines form simply connected helical loops. For a current perturbation to be destabilising (i.e. for instability growth), it must be directed along magnetic field lines. As an island

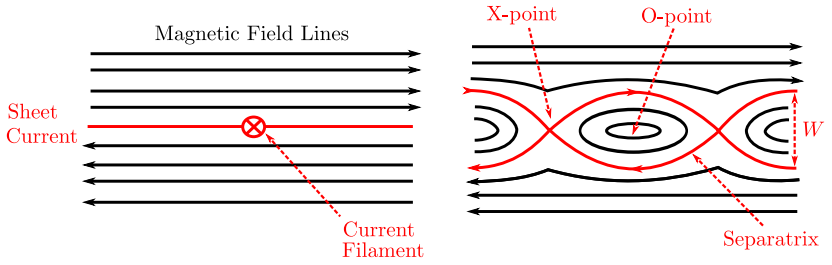

FIGURE 3.1: Left: A sheet current and the resulting magnetic field. A current filament is imposed. Right: The new reconnected field configuration: a magnetic island. The island X-point, O-point, separatrix and island width, W, are indicated.

forms around a field line it also has this helical structure, with X-points and O-points following closed field lines. A magnetic island is a normal mode of the rational surface, with periodic boundary conditions in the poloidal and toroidal directions. In the poloidal cross section there are an integer number, m, of islands in a joined up chain and in the toroidal cross section there are n islands, where m and n are the poloidal and toroidal mode numbers.

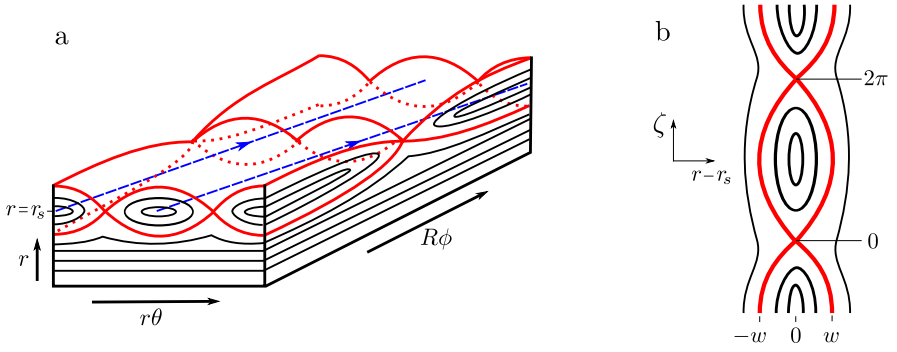

FIGURE 3.2: a) A $m/n = 2/1$ magnetic island in the slab geometry. b) The magnetic island transformed into the X, ζ coordinate system.

The magnetic island geometry used for this thesis is now considered. Figure 3.2a shows an $m/n = 2/1$ magnetic island in the 'slab' geometry. This geometry is an approximation to the toroidal geometry, which is less valid for finite aspect ratio tokamaks. However, working in this geometry helps to make a number of interesting problems tractable and it is therefore used with the caveat that some physics may be missing from the final results. Figure 3.2b shows the same island transformed into a coordinate system in which the poloidal and toroidal angles, θ and ϕ, have been combined into a helical angle, given by:

$$\zeta = m\left(\theta - \frac{\phi}{q_s}\right) \tag{3.1}$$

A shifted radial coordinate $r - r_s$ (equal to 0 at the rational surface r_s) and the island half width, w (not to be confused with the full width W) are also introduced.

The equilibrium helical field is given by [32]:

$$B_\zeta = B_\theta \left(1 - \frac{q(r)}{q_s}\right) \tag{3.2}$$

This is the normal equilibrium field minus a single helicity field with the same helicity as the rational surface. The helical field changes sign as the rational surface is crossed. The Taylor expansion of the q profile about r_s is $q(x) = q_s + q'_s(r - r_s) + ...$ (where $q'_s = \frac{dq}{dr}\Big|_{r=r_s}$). This can be inserted into equation 3.2:

$$B_\zeta = B_\theta \frac{q'_s}{q_s}(r - r_s) \tag{3.3}$$

The magnetic island introduces an additional radial magnetic field component, which can also be expressed as a perturbed island flux:

$$B_r = \tilde{B}_r \sin\zeta \tag{3.4}$$

$$\psi = \tilde{\psi} \cos\zeta \tag{3.5}$$

The direction of the perturbed field lines is given by:

$$\frac{m}{r_s}\frac{dr}{d\zeta} = \frac{B_r}{B_\zeta} \tag{3.6}$$

Equations 3.3 and 3.4 are then substituted in to equation 3.6:

$$(r - r_s)dr = \frac{r_s q_s \tilde{B}_r}{m q'_s B_\theta} \sin\zeta d\zeta \tag{3.7}$$

The equation for the island half width is the radial amplitude of this sinusoidal perturbation:

$$w = \sqrt{4\frac{r_s q_s \tilde{B}_r}{m q'_s B_\theta}} \tag{3.8}$$

Note that a high magnetic shear or a high poloidal mode number leads to a smaller island width. Including this in equation 3.7, integrating and multiplying by 4 gives:

$$2(r - r_s)^2 = w^2 \cos\zeta + w^2\Omega \tag{3.9}$$

Here Ω is a constant of integration, constant on a perturbed island flux surface. The equation defining the island flux surfaces then becomes:

$$\Omega = \frac{2(r - r_s)^2}{w^2} - \cos\zeta \tag{3.10}$$

The value of Ω is 1 on the separatrix and -1 at the island O-point. The $2(r-r_s)^2/w^2$ part of equation 3.10 is due to the equilibrium helical flux. In assuming that the q profile could be described by the zeroth and first order terms of the Taylor expansion, a quadratic form has been obtained. The inclusion of higher order terms to give a more realistic q profile would introduce more corrective terms to this equilibrium part. In calculating the perturbed flux term, $\cos\zeta$, it has been assumed that the amplitude of the perturbed helical flux, $\tilde{\psi}$ is independent of r; the so-called 'constant ψ approximation'. Alternatives to the constant ψ approximation are considered in section 3.2.

3.2 Classical tearing mode theory

Classical tearing modes can grow spontaneously as the result of unfavourable current and pressure profiles. As was described in Chapter 1, magnetic reconnection can only occur in regions where the resistive and ideal parts of Ohm's law become comparable. There is a thin resistive layer of width l around a rational surface, within which ideal MHD becomes invalid and resistive MHD must be used [33]. Whether the region is stable or unstable depends on global profiles and this is usually determined for a large aspect ratio tokamak by solving the cylindrical tearing mode equation (equation 3.11) for the resultant perturbed flux, $\psi(r)$.

$$\frac{d^2\psi}{dr^2} + \frac{1}{r}\frac{d\psi}{dr} - \left(\frac{m^2}{r^2} + \frac{\mu_0 \frac{dj}{dr}}{B_\theta(r)\left[1 - q(r)\frac{n}{m}\right]}\right)\psi = 0 \tag{3.11}$$

The solution method is as follows. Outside the layer, ideal MHD can be used with appropriate boundary conditions far from the rational surface. Inside the layer resistive MHD is used. The solutions must then be matched at either side of the layer but this cannot, in general, happen without a discontinuity in the first radial derivative, $\frac{d\psi}{dr}$ [34]. This discontinuity is characterised by the Δ' parameter, given by:

$$\Delta' = \frac{1}{\psi}\left[\left.\frac{d\psi}{dr}\right|_{r=r_s+l} - \left.\frac{d\psi}{dr}\right|_{r=r_s-l}\right] \tag{3.12}$$

Figure 3.3 shows an approximate analytic solution to 3.11, which assumes an equilibrium current profile of the form $j(r) = j_0(1 - (r/a)^2)$ [35]. The plot of ψ has a discontinuity at the rational surface, the location of which is indicated by the dashed black line.

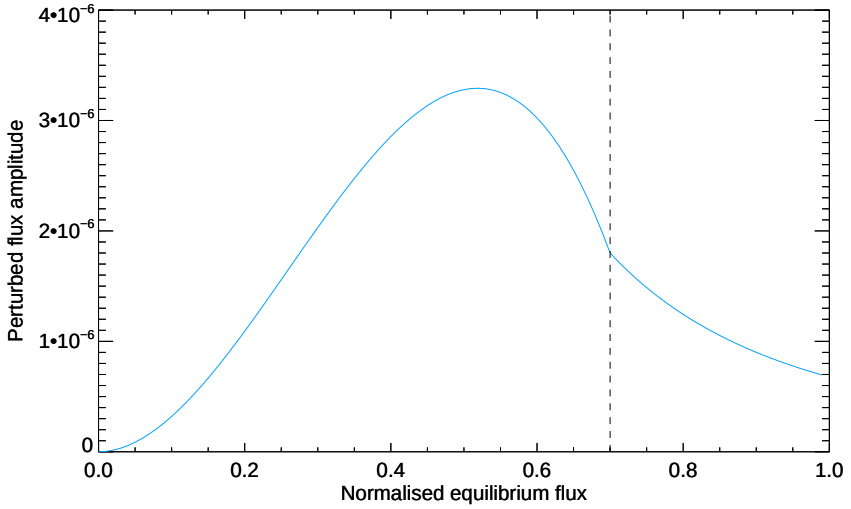

FIGURE 3.3: An approximate analytic solution to the cylindrical tearing mode equation; the perturbed flux amplitude, ψ. The rational surface location is indicated by the dashed black line.

It is important to note that the peak of the perturbed flux is typically inside the rational surface ($r < r_s$) for the cylindrical geometry. This means that there is a gradient in ψ either side of the rational surface and demonstrates that use of the constant ψ approximation does not allow for a realistic island geometry. This form of the perturbed flux gives rise to magnetic islands that are radially asymmetric, with a wider side in the region $r < r_s$, which is observed experimentally [35]. Asymmetric islands can also be explained by a more complex equilibrium flux function, with the inclusion of higher order terms in the q profile Taylor expansion [36]. A 'realistic' formula for the island flux surfaces (both perturbed and equilibrium) can be derived using the cylindrical tearing mode equation and a realistic q profile but a number of new unknown free parameters are introduced [35]. This presents its own set of difficulties and is covered in more detail in Chapter 4, where a quasi-linear correction for asymmetric magnetic islands is used (equation 3.13). Here a single free parameter, A, is introduced to capture the asymmetric geometry but avoid an excess of unknown free parameters.

$$\Omega = \frac{2(r-r_s)^2}{w^2} - \left[\frac{A(r-r_s)}{w} + 1\right]\cos\zeta \tag{3.13}$$

For the rest of this chapter, the constant ψ approximation is assumed, in order to present a simple description of the essential physics of each mechanism.

3.2.1 The Rutherford equation

A highly localised jump in $\frac{d\psi}{dr}$ also means a spike in $\frac{d^2\psi}{dr^2}$, which, by Ampere's law, gives a parallel current perturbation. This can either stabilise or destabilise a tearing mode depending on the sign of the discontinuity. The time evolution of such a mode can be evaluated by considering the resistive diffusion of the perturbed radial field in Ohm's law:

$$\frac{\partial B_r}{\partial t} = \frac{\eta}{\mu_0}\nabla^2 B_r \tag{3.14}$$

Since the mode is narrow in r compared to ζ, it can be approximated that $\nabla^2 \approx d^2/dr^2$. Equation 3.14 is then integrated across the full island width:

$$\int_{-W/2}^{+W/2} \frac{dB_r}{dt} dr \approx \frac{\eta}{\mu_0} \int_{-W/2}^{+W/2} \frac{d^2 B_r}{dr^2} dr \tag{3.15}$$

Assuming the constant ψ approximation, B_r is independent of r and we have:

$$W\frac{dB_r}{dt} \approx \frac{\eta}{\mu_0}\left[\frac{dB_r}{dr}\right]_{-W/2}^{+W/2} \tag{3.16}$$

Since $B_r \propto W^2$, the substitution $W\frac{dB_r}{dt} = 2B_r\frac{dW}{dt}$ can be made. Also, making the substitution $B_r = \frac{m\psi}{r}$:

$$\frac{2\mu_0}{\eta}\frac{dW}{dt} \approx \frac{1}{\psi}\left[\frac{d\psi}{dr}\right]_{-W/2}^{+W/2} \tag{3.17}$$

Using the equations for Δ', assuming the island width is about the same as the resistive layer, and the timescale for resistive diffusion, $\tau_R = 1.22\frac{\mu_0 r^2}{\eta}$ (where the 1.22 comes from flux surface averaging in a large aspect ratio, circular cross section geometry), the Rutherford equation for the time evolution of the classical tearing mode width, W, can be obtained. The equation from the original paper, which has a derivation more complicated than the one presented above is shown below:

$$\frac{\tau_R}{r^2}\frac{dW}{dt} = \Delta' \tag{3.18}$$

From equation 3.18 it is clear that $\Delta' > 0$ gives island growth. Also, it can be shown that the magnetic energy change due to the presence of a tearing mode is proportional to $-\Delta'$ [37], which again indicates that positive Δ' makes the island the most energetically favourable state and the tearing mode unstable. Δ' is normally considered to be constant, giving rise to linear growth or decay in time from this contribution. In most modern tokamaks, the current profile is tailored such that Δ' is negative for the rational surfaces in the plasma. However, there are circumstances when it is possible for Δ' to become positive even with this profile tailoring. This is discussed in more detail in section 3.7.

3.3 The bootstrap current drive

As described above, a tearing mode consists of a helical magnetic island with its own internal flux surfaces. This provides a route for transport of heat and particles along field lines from one side of the island to the other. This fast parallel transport serves to flatten the pressure profile across the island. In a high temperature tokamak, this produces a helical 'hole' in the pressure gradient dependent bootstrap current at the island O-point, providing a neoclassical drive for tearing mode growth. The Rutherford equation for this neoclassical tearing mode (NTM) is modified by an additional term, describing the bootstrap current perturbation. An early version of this modification is shown below [38].

$$\frac{\tau_R}{r_s^2}\frac{dW}{dt} = \Delta' - \varepsilon^{\frac{1}{2}}\frac{L_q}{L_p}\frac{\beta_p}{W} \tag{3.19}$$

Here, ε is the inverse aspect ratio and L_q and L_p are the gradient length scales for the safety factor, q and the pressure, p, defined as $q(dq/dr)^{-1}$ and $p(dp/dr)^{-1}$. This new drive term:

$$\Delta_{bs}(W) = -\varepsilon^{\frac{1}{2}}\frac{L_q}{L_p}\frac{\beta_p}{W} \tag{3.20}$$

predicts spontaneous growth of NTMs from zero size, with no perturbation required. This is usually positive due to the negative pressure gradient in L_p and positive magnetic

shear in L_q. If this description were accurate no tokamak would be able to maintain a stable plasma, which implies that some additional physics must be included. In 1995, neoclassical tearing modes were observed experimentally on the TFTR tokamak and compared with theory for the first time. Measurements made with the electron cyclotron emission (ECE) diagnostic showed that there was a threshold island width above which NTMs grew, observed to be just larger than 1cm [39]. It was shown that large island evolution agreed well with the bootstrap current model in equation 3.19 but that there was deviation from this as the mode decayed, indicating the presence of additional small island effects. Later that year, Fitzpatrick published a paper describing a transport model for a magnetic island, which provided an explanation for the NTM threshold and small island physics [1]. It was shown that small islands do not completely flatten the pressure profile and therefore have a reduced bootstrap drive.

This can be explained by considering the connection length, L_c, the length along a field line from one side of the island to the other. Appendix A outlines the numerical integration method for calculating L_c for a magnetic island. Figure 3.4 shows plots of L_c as a function of r for islands of different half widths. Field lines lying on the island separatrix do not wrap around the island so L_c increases asymptotically as the separatrix is approached.

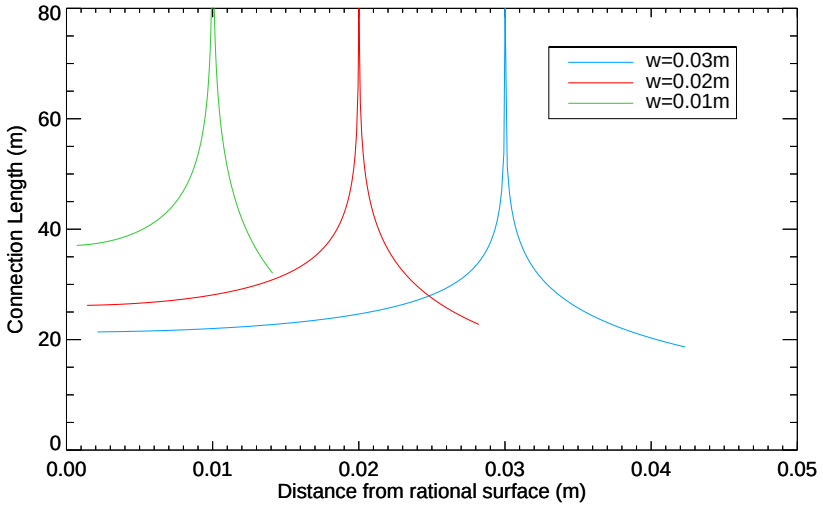

FIGURE 3.4: The connection length as a function of radius at $\zeta = \pi$ for islands of three different half widths, indicated in the key.

The result of this increasing field line length is that the parallel transport around the island is reduced to a level comparable to the perpendicular transport across the island. This gives rise to a boundary layer, in the vicinity of the island separatrix, in which the

pressure is not completely flattened. The width of this layer is a function of the ratio of perpendicular and parallel thermal diffusivities, $\chi_\perp/\chi_\parallel$. Figure 3.4 shows that, as the island width decreases, the separatrices get closer together and L_c increases with a $1/W$ dependence. Consequently, the flattening and bootstrap current perturbation are expected to be reduced for small islands. When $\Delta' < 0$ (i.e. classically stable) this gives rise to a threshold width, W_{th}, below which the bootstrap drive, Δ_{bs}, is less than $|\Delta'|$ and the island shrinks away. In this case a seed island, larger than W_{th}, is required for an NTM to grow (see section 3.3.1).

Fitzpatrick showed how equation 3.20 could be further modified to include this physics. The result is shown in equation 3.21.

$$\Delta_{bs}(W) = a_{bs} r_s \beta_p \frac{W}{W^2 + W_d^2} \tag{3.21}$$

The a_{bs} term contains information about the bootstrap current:

$$a_{bs} = a_1 L_{bs} \frac{L_q}{L_p} \tag{3.22}$$

L_{bs} is the bootstrap current length scale, defined in detail by Sauter [40]. The constant a_1 can be calculated for a given equilibrium and has a typical value of ~ -3 [41]. This is discussed in more detail in Chapter 6.

Also introduced in equation 3.21 is the characteristic length scale, W_d, given by equation 3.23.

$$W_d = 5.1 w_c = 5.1 \left(\frac{\chi_\perp L_s^2}{\chi_\parallel k_\theta^2} \right)^{\frac{1}{4}} \tag{3.23}$$

Here, L_s is the magnetic shear length scale and k_θ is the poloidal wavenumber. This term reduces the bootstrap drive for small islands and is related to the threshold island width. The critical width, w_c, was also introduced by Fitzpatrick [1] and is related to the width of the boundary layer in the pressure profile. The relation $W_d = 5.1 w_c$ comes from matching analytic small and large island limits. Chapter 4 describes a method for inferring w_c from experimental Thomson scattering data.

3.3.1 Seed islands

Seed islands with a width above W_{th} can be created by a variety of instabilities, fluctuations and external perturbations.

Instabilities located at different radial locations can perturb rational surfaces throughout the plasma, which can result in NTM growth if the perturbation is big enough. For example, a sawtooth instability is an internal kink mode at the $q = 1$ surface that can periodically 'crash', throwing heat and particles out of the core and perturb other rational surfaces. This is a common cause of NTM growth and can be ameliorated by using localised current drive to increase the sawtooth frequency, which decreases the size of the crash and the likelihood of NTM growth [42]. Another potential source of seed islands is the fishbone instability, also related to the $q = 1$ surface but is driven unstable by energetic, trapped particles. As was mentioned in Chapter 2, fishbones are common in NBI heated plasmas as they tend to have a large fast particle population. Edge localised modes (ELMs) are periodic edge-plasma eruptions caused by the steep pedestal pressure gradient in H-mode, which can also create seed islands. To avoid damage to the plasma facing components, future tokamaks will have to avoid ELMs or find ways of minimising their size, which should reduce the chance of creating seed islands bigger than W_{th}. Such instabilities have been observed to trigger NTM seed island formation on all of the large modern tokamaks, such as NSTX [26], DIII-D [43, 44] and ASDEX Upgrade [45].

In order to decouple the formation of a seed island from the interaction with its seeding instability, external perturbations can be applied in a controlled way to drive an NTM unstable. Resonant magnetic perturbation (RMP) coils have been used to apply a well described perturbations to the flux surfaces on COMPASS-D [46]. Similarly, a set of RMP coils on the TEXTOR tokamak have been used to grow well characterised NTMs for ECCD stabilisation experiments [47].

There is also a class of so-called 'spontaneous' or 'triggerless' NTMs which grow, apparently without a seed island, from an unknown small size below the background noise level. Explanations for the growth of such NTMs include coupling between an $(m-1)/n$ mode and the $q = m/n$ surface [26], proximity to a plasma β limit [48] or a removal of the threshold by a coupling to resistive wall modes [49]. Such triggerless NTMs have been observed to grow on MAST and are discussed in Chapter 4. Section 3.7 describes the β limit thought to cause the growth of these NTMs and describes their characteristics in more detail.

3.4 The curvature contribution

Curvature increases the energy it takes to bend the field lines in a tokamak and has a stabilising effect on perturbations. In 1975, Glasser, Greene and Johnson derived the mathematics to describe this stabilising contribution, which is often referred to as the GGJ effect [50]. For NTMs, the important term to emerge from this work was the resistive interchange parameter, D_R. This can be introduced as an additional contribution to the Rutherford equation of the form [51]:

$$\Delta_{GGJ}(W) = a_{GGJ} r_s \beta_p \frac{1}{\sqrt{W^2 + 0.65 W_d^2}} \tag{3.24}$$

The form of the a_{GGJ} term is shown in equation 3.25. The resistive interchange parameter can be calculated using equilibrium codes, such as CHEASE [52], or using a simplified analytic expression, also shown in equation 3.25 (see Chapter 6).

$$a_{GGJ} = a_2 \frac{D_R}{\beta_p} \approx a_2 \frac{\varepsilon^2}{s} \frac{L_q}{L_p} \left(1 - \frac{1}{q^2}\right) \tag{3.25}$$

Here, s is the magnetic shear. The curvature contribution scales as $\varepsilon^{3/2}\beta_p$ whereas the bootstrap contribution $\varepsilon^{1/2}\beta_p$. In large aspect ratio tokamaks the bootstrap drive tends to dominate over the curvature stabilisation but in spherical tokamaks this ε dependence results in the two terms being comparable. This would imply that STs are less susceptible to NTMs [41].

3.5 The polarisation current contribution

In Chapter 2 it was explained that magnetic islands rotate toroidally in the lab frame. Islands can also rotate in the frame of the plasma, at frequency ω. As an island rotates through the plasma, it pushes the electrons and ions out of the way. The inertia difference between electrons and ions means that they move at different speeds and there is a net flow of current perpendicular to the island. Charge conservation and quasineutrality mean that the current must obey $\nabla.\mathbf{J} = 0$ and there must be a return current parallel to the island (and the magnetic field). Depending on the direction of the current, this can either stabilise or destabilise an NTM. This 'polarisation current' effect can be included as another additional contribution to the Rutherford equation [53]:

$$\Delta_{pol}(W) = a_{pol} r_s \beta_p \frac{W}{\sqrt{W^4 + W_{b,i}^4}} \tag{3.26}$$

Here, $W_{b,i}$ is the ion banana orbit width, given by $W_{b,i} \approx \pi r_{L,i}/\sqrt{2\varepsilon}$. At present, polarisation current theory is only developed for $W > W_{b,i}$. In order to take account of this, the functional form $\Delta_{pol} \propto W/(W^4 + W_{b,i}^4)$ was adopted as a heuristic model [53]. Equation 3.27 gives the form of a_{pol}.

$$a_{pol} = a_3 \left(\frac{L_q}{L_p}\right)^2 W_{b,i}^2 \; g(\varepsilon, \nu_{ii}, \omega) \tag{3.27}$$

Here, a_3 is an order 1 constant, which will be discussed further in Chapters 6 and 7. The parameter g is a function of ε, the inverse aspect ratio, ν_{ii}, the ion collision frequency and ω, the island rotation frequency and must be determined by a kinetic calculation. However, analytic approximations, shown in equation 3.28, are available in the collisional [54] and collisionless [55] regimes.

$$g(\varepsilon, \nu_i, \omega) = \begin{cases} \varepsilon^{-1} & \text{for } \nu_{ii}/\varepsilon\omega \to \infty \\ 1.64\varepsilon^{\frac{1}{2}} & \text{for } \nu_{ii}/\varepsilon\omega \to 0 \end{cases} \tag{3.28}$$

The $1/W^3$ dependence of Δ_{pol} means that this effect is significant for very small islands, which means it should play a role in determining W_{th}. However, there is a great deal of uncertainty over the nature of this contribution due to the complex rotation and collisionality dependences of $g(\varepsilon, \nu_{ii}, \omega)$. Though there have been attempts to compare experimental data with the predictions of this model [56], islands must be very small to see a significant effect. For a thorough investigation, it must also be possible to control the rotation of the island relative to the plasma, which is only possible on a small number of tokamaks, such as DIII-D. These issues are discussed in more detail in Chapter 6.

3.6 The non-linear contribution from the current profile

The classical tearing stability parameter, Δ', describes linear growth for a small island. For islands that grow much larger than the resistive layer width, it is important to include the nonlinear effects due to the equilibrium current profile. As many of the magnetic islands considered in this thesis approach 20% of MAST's minor radius, this

contribution should be considered. A simple approximation for this contribution to the Rutherford equation is given by [57]:

$$\Delta_{nl} = -a_{nl} W \tag{3.29}$$

This term describes the nonlinear saturation of the classical tearing mode. The parameter, a_{nl}, can be calculated but is a function of the first and second radial derivatives of the equilibrium current density [58], which have very large errors experimentally. It is worth noting that this nonlinear physics is often described as being due to Δ' having a stabilising W dependence for larger islands [43, 57, 59], which essentially has the same effect as the term used here. This will be discussed further in Chapter 6.

3.7 The ideal β_N limit and positive Δ'

It has been shown that, close to the ideal β_N limit, there is a large, positive 'pole' in Δ' which can drive tearing modes unstable [48, 60]. 'Triggerless' NTMs have been reported close to the β_N limit in DIII-D hybrid scenarios [61] and similar NTMs, observed on MAST, are reported in Chapter 6 of this thesis.

When considering the positive Δ' case, it is important to point out that a tearing mode is defined as 'classical' if Δ' is the dominant driving term and 'neoclassical' if Δ_{bs} is the dominant driving term. It is entirely possible that the balance of these contributions could change during the lifetime of an NTM. For example, it has already been shown that Δ_{bs} decreases for islands smaller than W_d. It is possible that a small positive Δ' could make a classical tearing mode unstable from a very small size but that as it grew to a size comparable to W_d, Δ_{bs} would become dominant and the tearing mode would become neoclassical. Furthermore, it is also possible that the growth of a large magnetic island could cause Δ' to decrease, either by degrading confinement and reducing the β away from the ideal limit or by altering the equilibrium current profile. The balance of these terms will be discussed further in Chapter 6.

3.8 The modified Rutherford equation

The overall stability of an NTM is given by a sum of various contributions, known as the modified Rutherford equation (MRE). Here, only those contributions outlined above are

included but there are numerous other effects that can be added in, such as externally imposed ECCD stabilisation [59] or the effect of sheared plasma flows [62]. The version of the MRE used throughout this thesis is shown below:

$$\frac{\tau_r}{r_s}\frac{dW}{dt} = r_s\Delta' - a_{nl}W + \Delta_{bs}(W) + \Delta_{GGJ}(W) + \Delta_{pol}(W) \tag{3.30}$$

It is instructive to study the relative effects of each of the terms in a plot of dW/dt against W. Figure 3.5 shows pairs of dW/dt against W (top) and W against t (bottom) plots for different combinations of terms from the MRE.

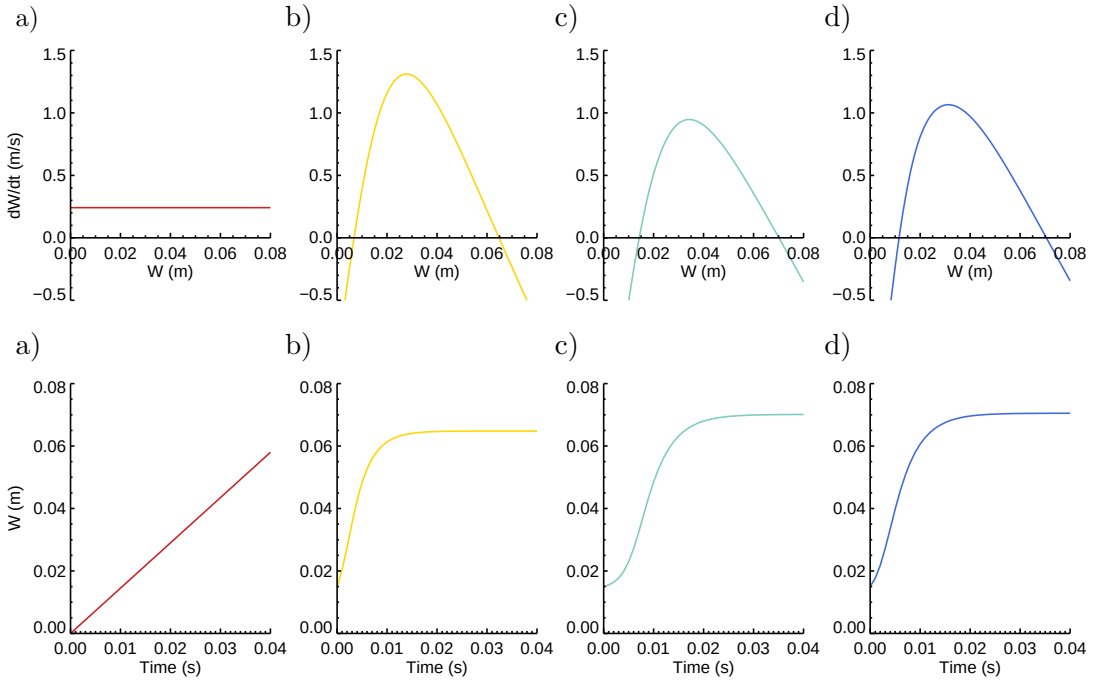

FIGURE 3.5: The MRE with different combinations of terms. **a)** Destabilising Δ' only. **b)** Stabilising Δ', $-a_{nl}W$ term and Δ_{bs} term. **c)** Marginally destabilising Δ', $-a_{nl}W$ term, Δ_{bs} and Δ_{GGJ} term. **d)** Marginally destabilising Δ', $-a_{nl}W$ term, Δ_{bs}, Δ_{GGJ} term and Δ_{pol} term.

For these examples, W_d is taken to be 3.5cm (approximately the value of this parameter calculated in Chapter 4). The sizes of other parameters are not discussed in detail but are typical for the MAST plasmas considered in Chapter 6. The four pairs of plots are described below:

a) This pair of plots has $r_s\Delta' = 1$ and no other terms included. It shows linear growth from zero starting size with no saturation.

b) This pair has $r_s\Delta' = -4$ but also includes the $-a_{nl}W$ term and the Δ_{bs} term. This is an illustrative example for a hypothetical large aspect ratio tokamak with

a strong bootstrap current drive and a small curvature term that can be neglected. Even with a stabilising Δ', the threshold island width is less than 1cm. With a 1.5cm seed island, dW/dt is immediately strongly positive and the island grows to saturation.

c) This pair has $r_s\Delta' = 0.1$ and the Δ_{GGJ} term is also included. This example is more representative of the MAST plasmas considered in this thesis. The curvature term is strongly stabilising so, for NTM growth from the 1.5cm seed island, a marginally destabilising Δ' is required. The lower plot shows that dW/dt initially small and linear, indicating that Δ' is initially the dominant driving term. As the island grows bigger than W_d, the bootstrap drive takes over and the growth rate increases.

d) This pair of plots is the same as in pair c but with the addition of a destabilising Δ_{pol} term. This only noticeably affects the early part of the island evolution. There are now two additional terms compared to the centre-left pair but the plots do not look significantly different. This is a heuristic illustration that distinguishing between the different contributions using the magnetic island width evolution can be a challenge. This issue is revisited more quantitatively in Chapter 6.

There have been several analyses of the MRE for NTMs in different tokamaks such as MAST [41], JET [63] and ASDEX-U [59]. The equation is usually fitted to experimental data with a number of free parameters, such as the coefficients a_1, a_2, a_3 [41, 59] and W_d [41]. Alternatively, comparisons of the quality of fit to data are made with some contributions not included. This can help to investigate, for example, whether the small island evolution is best described by the bootstrap current model, the polarisation current model or both combined [41, 63].

In these fitting procedures the value of W_d is often calculated using analytical formulae for $\chi_\perp$ and $\chi_\parallel$, which make assumptions about the nature of the heat transport. In this thesis W_d is inferred from experimental measurements of the island temperature profile, which avoids the need predict the formulae for $\chi_\perp$ and $\chi_\parallel$. This method is described in Chapter 4

3.8.1 β_p dependence

An important feature of the MRE is that the Δ_{bs}, Δ_{GGJ} and Δ_{pol} terms are all proportional to β_p. If Δ' is negative there is a value of β_p below which an NTM cannot

grow, regardless of the seed island size. Figure 3.6 shows plots for the MRE and the time-integrated MRE for two values of β_p; one in blue, above the marginal value, and one in red, just below the marginal value.

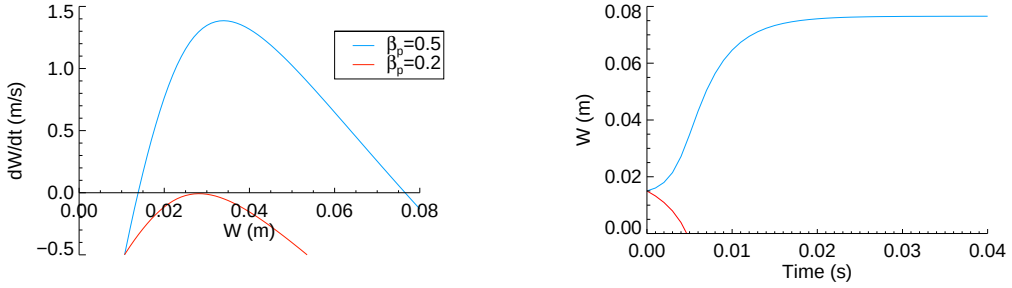

FIGURE 3.6: Left: The MRE. Right: The time-integrated MRE. The blue curve is above the marginal β_p and therefore an island grows to saturation. The red curve is just below the marginal β_p and islands of all widths have a negative growth rate.

Equation 3.31 for the saturated island width ($dW/dt = 0$) can be written down, assuming that the saturated island size is much larger than W_d, assuming the Δ_{pol} term is negligible for large islands and ignoring the $-a_{nl}W$ term for the sake of simplicity.

$$W_{sat} \approx r_s \beta_p \frac{a_{bs} + a_{GGJ}}{-\Delta'} \tag{3.31}$$

Equation 3.31 shows that W_{sat} is approximately proportional to β_p. This dependence has enabled a series of 'β ramp-down' experiments, which allow investigation of the balance of stabilising and destabilising terms in the MRE for different sized islands (see figure 3.7). Three stages of the island evolution are defined; growth, saturation and decay. The growth and saturation stages usually occur spontaneously after an NTM is driven unstable but the decay stage is usually externally imposed by a reduction in global β_p via a reduction in the applied heat power. For instability triggered NTMs, the growth stage can start at any island size bigger than W_{th} and depends on the size of the initial seed island. As the timing and size of the triggering instability is in some sense 'random', small island physics in the growth stage can be difficult to investigate. To some extent, the decay stage is more externally controllable and can allow observations of small island physics, which is the main advantage of β ramp-down experiments. Figure 3.7 shows that towards the end of the decay phase, as the island shrinks below $W_d = 3.5cm$, the decay rate increases as the Δ_{bs} drive term rapidly shrinks.

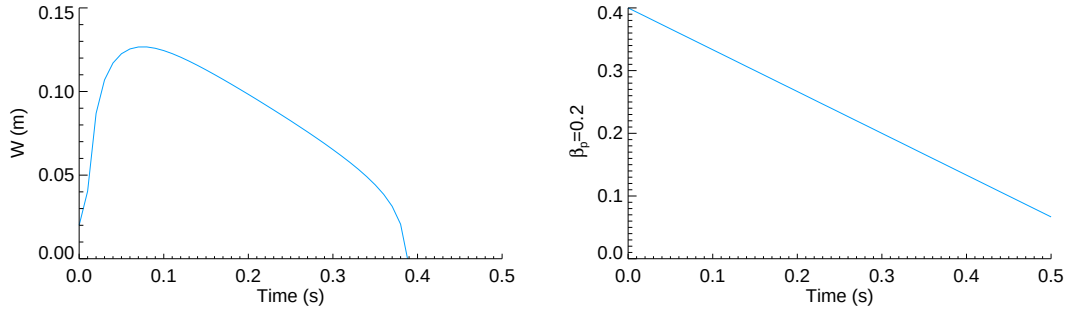

FIGURE 3.7: A simulated β ramp-down. The MRE is integrated while β_p is made to decrease linearly in time.

As was mentioned above, W_d is inferred from experimentally measured temperature profiles in Chapter 4 and this is then compared to the experimentally measured W evolution for a β ramp-down experiment in Chapter 6.

3.9 Summary

This chapter has described a range of stabilising and destabilising contributions affecting NTM evolution. These particular contributions are thought to be most relevant to NTMs on the MAST tokamak, but there are other contributions that are worthy of consideration. These terms have been included in a version of the modified Rutherford equation, which will be used in Chapter 6 for a study of magnetic island evolution on MAST. One particular parameter in this equation, $W_d(= 5.1w_c)$, is thought to be of particular importance in determining the physics of small islands and the threshold island width for NTM growth. In Chapter 4, a method for experimentally determining w_c, and hence W_d, will be presented. This will then be used in Chapter 6's analysis of NTM evolution.

Chapter 4

A heat transport model for a magnetic island

4.1 Introduction

In Chapter 3, the theories that describe NTM evolution were outlined, including Fitzpatrick's transport model, which provides a potential explanation for the observed threshold island width [1]. The model allows the geometry of the NTM temperature perturbation to be studied by solving a heat transport equation for the associated magnetic island. This chapter investigates a version of Fitzpatrick's equation, modified to account for the radially asymmetric magnetic islands observed on MAST. Similar transport model schemes have been investigated previously by Meskat [35] and Hölzl [64] but here a fast solution method is presented, which uses Fourier series for one dimension and a finite difference scheme for the other. Appropriate boundary conditions are then derived by taking analytic limits of the equation. The solutions are model temperature profiles, the geometry of which is described by a set of six parameters, including w, the island half width, and w_c, a key parameter in the transport threshold model. In Chapter 5, these temperature profiles are fitted to data from the MAST Thomson scattering system, in order to experimentally infer the value of w_c.

4.2 The heat transport model

Recall that an NTM induced magnetic island provides a route for the transport of heat and particles along a field line from one side of the island to the other. This flattens

the temperature profile across the island and produces a helical 'hole' in the bootstrap current at the island O-point, providing a drive for NTM growth. The connection length, L_c, along a field line from one side of the island to the other increases towards the separatrix, which leads to a boundary layer where the temperature is not completely flattened. For small islands, the boundary layer takes up a significant fraction of the island width, which means that both the amount of temperature flattening and the size of the bootstrap current perturbation are reduced. In Chapter 3 it was shown that this gives rise to threshold width, w_{th}, below which the island shrinks away.

This boundary layer can be measured in electron temperature (T_e) profiles within and around islands. With a suitable model for heat transport this can be used to infer the critical width, w_c [1, 65, 66]. If this model is correct then w_c inferred from experimental T_e profiles can be used to estimate w_{th}, which can then be compared to the value of w_{th} evaluated using a β ramp-down experiment (see Chapter 6). One of the key aims of this thesis is to make this comparison.

A 2D coordinate system is used for the magnetic island, in which $\zeta = m\left(\theta - \frac{\phi}{q_s}\right)$ is the helical angle (with θ and ϕ the poloidal and toroidal angles), $X = \frac{(\Psi - \Psi_s)}{w}$ is a normalised poloidal flux coordinate and $w = W/2$ is the island half-width. As was shown in Chapter 3, the flux surfaces are described by flux function Ω:

$$\Omega = 2X^2 - (AX + 1)\cos\zeta \tag{4.1}$$

Example island flux surfaces are plotted in figure 4.1. Fitzpatrick's original equation assumed constant ψ whereas here a quasi-linear correction to the perturbed flux is used, parameterised by A [36]. In Chapter 3 it was shown that the perturbed flux solution to the cylindrical tearing mode equation has a gradient $d\psi/dr < 0$, which means that the larger side of the island is usually on the side of the rational surface nearest the core and that $A > 0$. More complicated flux functions are available but, in order to avoid over-fitting, a form has been chosen which both passes a quality of fit to data test, described in section 5.3.1, and has the fewest free parameters.

Assuming divergence-free, diffusive heat flow, the model can be written down as a heat transport equation of the form $\chi_\parallel \nabla_\parallel^2 T + \chi_\perp \nabla_\perp^2 T = 0$. Appendix B outlines the derivation of the parallel derivative, $\nabla_\parallel$, using equation 4.1. The perpendicular derivative is given by $\nabla_\perp = \frac{1}{w}\frac{d}{dX}$. The thermal diffusivities parallel and perpendicular

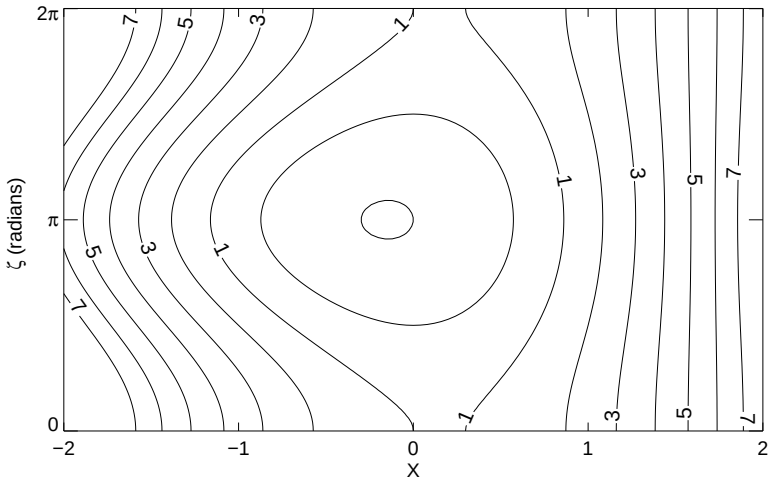

FIGURE 4.1: Surfaces of constant Ω in the (X, ζ) coordinate system. X is a dimensionless coordinate.

to the magnetic field are $\chi_\perp$ and $\chi_\parallel$. The resulting heat transport equation is shown in equation 4.2.

$$\left[\left(X + \frac{A\cos\zeta}{4}\right)\left.\frac{\partial}{\partial\zeta}\right|_X + \frac{AX+1}{4}\sin\zeta\left.\frac{\partial}{\partial X}\right|_\zeta\right]^2 T + \frac{w_c^4}{w^4}\frac{\partial^2 T}{\partial X^2} = 0 \tag{4.2}$$

A divergence-free model is thought to be justified at typical MAST $q = 2$ surface minor radii as they are neither in the core, where the NBI heating power is predominantly deposited, or close to the edge, where large heat losses can occur [67]. Here, w_c is given by:

$$w_c = \left(\frac{\chi_\perp L_s^2}{\chi_\parallel k_\theta^2}\right)^{\frac{1}{4}} \tag{4.3}$$

where L_s is the magnetic shear length scale and k_θ is the poloidal wavenumber. For simplicity $\chi_\perp$ and $\chi_\parallel$ are taken to be constant over the region of interest. When $w \sim w_c$, the perpendicular derivative term in equation 4.2 becomes important and a gradient is supported across the island. Note that w_c, as defined in this framework, is a factor of $\sqrt{8}$ smaller than the parameter defined in Fitzpatrick [1].

Previous work on ASDEX-U [35], in a low collisionality regime with electron mean free path $\lambda_e >> L_c$, used a collisional model with a correction factor to approximate convective heat transport. The relatively low temperature ($\sim$ 350 eV) and high density ($\sim 4 \times 10^{19}\mathrm{m}^{-3}$) at the MAST $q = 2$ surface cause λ_e and L_c to be comparable at $\sim$30m, putting it in a much more collisional regime and justifying our diffusive parallel

transport model. A kinetic approach, beyond the scope of this thesis, is required to treat lower collisionality regimes properly but such a model is currently under development at the University of York and future comparisons between this model and experimental data are discussed in Chapter 7.

Previous studies of NTM stability [41, 59, 63] have used analytic approximations to $\chi_\perp$ and $\chi_\parallel$ to estimate w_c. Choosing appropriate formulae for these diffusivities is not trivial as the nature of transport in a tokamak is not well understood. The advantage of absorbing all the transport physics into w_c and using it as an experimental fit parameter is that no specific models for $\chi_\perp$ and $\chi_\parallel$ need to be chosen. Indeed, the ratio $\chi_\perp/\chi_\parallel$ can also be calculated from the inferred value of w_c, although the uncertainties on this value are significant as it is proportional to w_c^4.

4.3 Solving the heat transport equation

In this section, the different stages of the method for solving equation 4.2 are presented. This is complemented by the full derivation of a required set of matrix elements in Appendix C and the derivation of the equation boundary conditions in Appendix D.

4.3.1 Solution method

Equation 4.2 is solved using a trial $N+1$ mode Fourier series solution of the form:

$$T(X,\zeta) = \sum_{n=0}^{N} T_n(X)\cos n\zeta \tag{4.4}$$

This trial solution is substituted into equation 4.2, which is then multiplied by an arbitrary $\cos k\zeta$ (integer k) and integrated over $\frac{1}{2\pi}\int_{-\pi}^{\pi}\ldots d\zeta$, resulting in an equation of the form:

$$\sum_{n=0}^{N}\left[a_{kn}\frac{d^2T_n}{dX^2} + b_{kn}\frac{dT_n}{dX} + c_{kn}T_n\right] = 0 \tag{4.5}$$

i.e. $N+1$ coupled equations for the $N+1$ Fourier mode amplitudes. The matrix elements a_{kn}, b_{kn} and c_{kn}, are given by the following formulae (derived in Appendix C):

$$a_{k,n} = -\frac{1}{128}\left(AX+1\right)^2\left(\delta_{k,n-2} + \underline{\delta_{k,2-n}} + \delta_{k,n+2}\right) + \left(\frac{1}{64}\left(AX+1\right)^2 + \frac{1}{2}\frac{w_c^4}{w^4}\right)\left(\delta_{k,n} + \underline{\delta_{k,-n}}\right) \tag{4.6}$$

$$b_{k,n} = \frac{AX+1}{16}\left[-\frac{An}{4}\left(\delta_{k,n-2} + \underline{\delta_{k,2-n}} - \delta_{k,n+2}\right) + X\left(\delta_{k,n-1} + \underline{\delta_{k,1-n}} + \delta_{k,n+1}\right) - 2nX\left(\delta_{k,n-1} + \underline{\delta_{k,1-n}} - \delta_{k,n+1}\right) + \frac{A}{2}\left(\delta_{k,n} + \underline{\delta_{k,-n}}\right)\right] \tag{4.7}$$

$$c_{k,n} = -\frac{A^2n^2}{128}\left(\delta_{k,n-2} + \underline{\delta_{k,2-n}} + \delta_{k,n+2}\right) + \frac{A^2n}{128}\left(\delta_{k,n-2} + \underline{\delta_{k,2-n}} - \delta_{k,n+2}\right) - \frac{An^2X}{8}\left(\delta_{k,n-1} + \underline{\delta_{k,1-n}} + \delta_{k,n+1}\right) - \frac{n}{16}\left(\delta_{k,n-1} + \underline{\delta_{k,1-n}} - \delta_{k,n+1}\right) - \left(\frac{1}{2}n^2X^2 + \frac{A^2n^2}{64}\right)\left(\delta_{k,n} + \underline{\delta_{k,-n}}\right) \tag{4.8}$$

Here, $\delta_{k,n}$ is the Kroneker delta function, equal to 1 for $k = n$ and equal to 0 otherwise. The underlined terms are only included for certain n, as k and n must be positive.

A second order finite difference scheme is used to solve equation 4.5. The Fourier coefficients $T_n(X)$ are discretised onto a radial grid with grid point index i and grid spacing Δ (there are $2I+1$ of these points, $-I \leq i \leq I$). The domain considered is the radial range $-X_{end} \leq X \leq X_{end}$, which covers about 40% of the minor radius, although typically only about half of this region is used when fitting to data. Equation 4.9 shows the equations used to approximate the derivatives.

$$\begin{aligned} \frac{d^2T_n}{dX^2} &= \frac{T_n^{i+1} - 2T_n^i + T_n^{i-1}}{\Delta^2} \\ \frac{dT_n}{dX} &= \frac{T_n^{i+1} - T_n^{i-1}}{2\Delta} \\ T_n &= T_n^i \end{aligned} \tag{4.9}$$

Substituting equation 4.9 into equation 4.5 gives:

$$\sum_{n=0}^{N} \left[a_{k,n} \frac{T_n^{i+1} - 2T_n^i + T_n^{i-1}}{\Delta^2} + b_{k,n} \frac{T_n^{i+1} - T_n^{i-1}}{2\Delta} + c_{k,n} T_n^i \right] = 0 \tag{4.10}$$

or:

$$\sum_{n=0}^{N} \left[P_{kn} T_n^{i-1} + Q_{kn} T_n^i + S_{kn} T_n^{i+1} \right] = 0 \tag{4.11}$$

where P_{kn}, Q_{kn} and S_{kn} are linear combinations of a_{kn}, b_{kn} and c_{kn}, given by:

$$\begin{aligned} P_{kn} &= \frac{a_{k,n}}{\Delta^2} - \frac{b_{k,n}}{2\Delta} \\ Q_{kn} &= \frac{-2a_{k,n}}{\Delta^2} + c_{k,n} \\ S_{kn} &= \frac{a_{k,n}}{\Delta^2} + \frac{b_{k,n}}{2\Delta} \end{aligned} \tag{4.12}$$

The domain is split into two regions at an arbitrary reference point, X_r. Boundary conditions at the end of each of these regions give two pieces of the solution which must be matched at X_r. The details of these boundary conditions are outlined in section 4.3.2.

In order to find the Fourier coefficients T_n^i that satisfy equation 4.11, they are each written as the sum of a basis set (with the same number of terms as the Fourier series):

$$T_n^i = \sum_{m=0}^{N} g_m t_{nm}^i \tag{4.13}$$

Equation 4.11 can then be re-written:

$$\sum_{n=0}^{N} \sum_{m=0}^{N} \left[P_{kn} t_{nm}^{i-1} g_m + Q_{kn} t_{nm}^i g_m + S_{kn} t_{nm}^{i+1} g_m \right] = 0 \tag{4.14}$$

Equations 4.15 and 4.16 are used to relate t^i_{nm} to its radially neighbouring coefficients, t^{i+1}_{nm} or t^{i-1}_{nm}, assuming that the solution varies linearly from one grid point to the next.

- For $X > X_r$:

$$t^i_{nm} = \alpha^i_{nj} t^{i+1}_{jm} + \beta^i_{nm} \tag{4.15}$$

- For $X < X_r$:

$$t^i_{nm} = \alpha^i_{nj} t^{i-1}_{jm} + \beta^i_{nm} \tag{4.16}$$

- For $X = X_r$:

$$\alpha^i_{nj} = 0 \qquad \beta^i_{nm} = \delta_{nm} \tag{4.17}$$

Using equation 4.17 for α^i_{nj} and β^i_{nm} at X_r decouples the solution at this point from the solution elsewhere and allows the two pieces to be matched at X_r.

The equations for matrices $\underline{\underline{\alpha}}^i$ and $\underline{\beta}^i_m$ are obtained by substituting equations 4.15 and 4.16 into equation 4.11, which gives equations 4.18, 4.19, 4.20 and 4.21.

- For $X > X_r$:

$$\underline{\underline{\alpha}}^i = -\left[\underline{\underline{P}}^i . \underline{\underline{\alpha}}^{i-1} + \underline{\underline{Q}}\right]^{-1} \underline{\underline{S}} \tag{4.18}$$

$$\underline{\beta}^i_m = -\left[\underline{\underline{P}}^i . \underline{\underline{\alpha}}^{i-1} + \underline{\underline{Q}}\right]^{-1} \underline{\underline{P}} . \underline{\beta}^{i-1} \tag{4.19}$$

- For $X < X_r$:

$$\underline{\underline{\alpha}}^i = -\left[\underline{\underline{Q}} + \underline{\underline{S}}^i . \underline{\underline{\alpha}}^{i+1}\right]^{-1} \underline{\underline{P}} \tag{4.20}$$

$$\underline{\beta}^i_m = -\left[\underline{\underline{Q}} + \underline{\underline{S}}^i . \underline{\underline{\alpha}}^{i+1}\right]^{-1} \underline{\underline{S}} . \underline{\beta}^{i+1} \tag{4.21}$$

Initially, $\underline{\underline{P}}$, $\underline{\underline{Q}}$ and $\underline{\underline{S}}$ are calculated at each grid point using equation 4.12. Then, starting at X_r, where $\underline{\underline{\alpha}}^i$ and $\underline{\beta}^i_m$ have known values (given by equation 4.17), $\underline{\underline{\alpha}}^i$ and $\underline{\beta}^i_m$ for the whole domain can be calculated by working outwards in either direction.

Equation 4.11 is then satisfied everywhere except at X_r. The condition for satisfying the equation at this point is:

$$P^r_{kn} t^{r-1}_{nm} g_m + Q^r_{kn} t^r_{nm} g_m + S^r_{kn} t^{r+1}_{nm} g_m = 0 \tag{4.22}$$

This can be written as an eigenvalue equation of the form $\underline{\underline{M}}.\underline{g} = 0$ where $M_{km} = P^r_{kn} t^{r-1}_{nm} + Q^r_{kn} t^r_{nm} + S^r_{kn} t^{r+1}_{nm}$. If a particular $\underline{\underline{M}}$ with a zero eigenvalue can be found, the equation will be satisfied everywhere. This zero eigenvalued $\underline{\underline{M}}$ is found by iterating over the boundary condition $T_n(X_{end}) = T^I_n$.

4.3.2 Boundary conditions

The boundary conditions are obtained by considering the behaviour of equation 4.2 at large X. The terms that decay at large X, are tracked by tagging them with a small parameter, ε:

$$\left[\left(X + \varepsilon\frac{A\cos\zeta}{4}\right)\left.\frac{\partial}{\partial\zeta}\right|_X + \varepsilon\frac{AX+1}{4}\sin\zeta\left.\frac{\partial}{\partial X}\right|_\zeta\right]^2 T + \varepsilon^2\frac{w_c^4}{w^4}\frac{\partial^2 T}{\partial X^2} = 0 \tag{4.23}$$

The temperature at large X, T, is expanded as a linear sum of basis functions, shown in equation 4.24. It is assumed that higher order terms are smaller at large X and are tagged with increasing order ε.

$$T = \varepsilon^0 t_0 + \varepsilon^1 t_1 + \varepsilon^2 t_2 + \ldots \tag{4.24}$$

Equation 4.24 is then substituted into equation 4.23. The terms that are tagged with matching order ε (denoted by $\mathrm{O}(\varepsilon)$) are considered independently and solved as separate equations. For example, the $\mathrm{O}(\varepsilon^0)$ equation is given by:

$$X^2\frac{\partial^2 t_0}{\partial\zeta^2} = 0 \tag{4.25}$$

Each $\mathrm{O}(\varepsilon)$ equation is solved in turn, eventually revealing the functional forms of t_0 and t_1 at large X. Terms of higher order than t_1 are ignored as they are assumed to be negligible at large X. The calculation for each order ε is shown in detail in Appendix D but the results of the calculation are outlined here. First, the $\mathrm{O}(\varepsilon^0)$ equation is solved

and it is found that t_0 is purely a function of X. Then, using the $O(\varepsilon^1)$ equation, the following equation for t_1 is obtained:

$$t_1 = \left(\frac{1}{4X} + \frac{A}{4}\right)\frac{dt_0}{dX} + \bar{t}_1(X) \tag{4.26}$$

where $\bar{t}_1(X)$ is an unknown function of X. Next, the solution to the $O(\varepsilon^2)$ equation is found, which shows that t_0 is linear in X. Finally, the $O(\varepsilon^3)$ equation is solved and $\bar{t}_1(X)$ is also found to be linear, so it can be absorbed into t_0.

The result of this calculation is that the appropriate boundary conditions for the zeroth and first order temperature basis functions are given by:

$$\begin{aligned} t_{0m} &= t_{end} \\ t_{1m} &= \left(\frac{1}{4X} + \frac{A}{4}\right)\frac{dt_{0m}}{dX} \end{aligned} \tag{4.27}$$

As was previously stated, it is assumed that all higher order terms in the t_{nm} basis set decay away at large X. In terms of the discretised basis set, the values of t_{1m} at X_{end} and at $-X_{end}$ are given by:

$$t_{1m}^{I} = \frac{\left(1 - \alpha_{00}^{I-1}\right)t_{end} - \beta_{0m}^{I-1}}{\alpha_{01}^{I-1} + 4\Delta\left(\frac{1}{X^I} + A\right)^{-1}} \tag{4.28}$$

$$t_{1m}^{-I} = \frac{\left(\alpha_{00}^{-I+1} - 1\right)t_{end} + \beta_{0m}^{-I+1}}{4\Delta\left(\frac{1}{X^{-I}} + A\right)^{-1} - \alpha_{01}^{-I+1}} \tag{4.29}$$

Recall that the index I is for the grid point at X_{end}. The final boundary conditions is then:

$$\underline{t}_m^{\pm I} = \begin{pmatrix} t_{end} \\ t_{1m}^{\pm I} \\ 0 \\ \vdots \end{pmatrix} \tag{4.30}$$

The value of the zeroth order term, t_{end}, is varied until the solution is convergent at the matching point. The $\underline{\underline{M}}$ which satisfies the matching condition is found by linear

interpolation of the smallest eigenvalue with respect to t_{end} to find the zero crossing. At each step of the iteration, the t^i_{nm} are recalculated from the new boundary condition, giving a different $\underline{\underline{M}}$ each time, until the eigenvalue converges to zero. The associated eigenvector, $\underline{g}$, is then used to reconstruct T^i from the basis set. Finally, the full Fourier series solution can be reconstructed and the 2D temperature profile obtained.

Once the equation is solved, the whole solution is multiplied by a factor that sets the temperature gradient far from the island, $T'_{end} = T'(-X_{end}) = T'(X_{end})$, and summed with the rational surface temperature, T_0, usually to match experimental data.

4.3.3 Solution summary

In summary the solution method is as follows:

1. Calculate P_{kn}, Q_{kn} and S_{kn} at every point in the domain.
2. Starting from $X = X_r$, work outwards in either direction calculating $\underline{\underline{\alpha}}^i$ and $\underline{\beta}^i_m$ using equations 4.18, 4.19, 4.20 and 4.21.
3. Starting at the boundaries, $X = -X_{end}$ and $X = X_{end}$ (with boundary condition $t^{\pm}_{end}$), work inwards calculating t^i_{nm} using equations 4.15 and 4.16.
4. Check to see if $\underline{\underline{M}}$ has a zero eigenvalue. If not, change the value of $t^{\pm}_{end}$ and go back to step 3. Iterate on the boundary condition until a zero eigenvalue is found.
5. Reconstruct the T profile using the associated eigenvector, g.

The method has been implemented in a FORTRAN 90 routine called *ntmtemp*, which can be called by other routines to quickly generate model temperature profiles in order to fit them to data using a least-squares minimisation, described in Chapter 5. The speed of the solution depends on the number of Fourier harmonics used but is usually around 1s per solution. This fast implementation has also been quasi-parallelised, using OpenMP, to enable a comprehensive set of data simulation runs, also described in Chapter 5.

4.4 Characterising the solutions

Figure 4.2 shows an example of the first four Fourier harmonic amplitudes of the solution, $T_n(X)$ (for $n = 0, 1, 2, 3$), for a symmetric magnetic island ($A = 0$). The zeroth harmonic is the dominant component at large X and has to be reduced by a factor of ten to fit

onto this plot. The first harmonic tends towards a constant value at large X, set by the boundary condition. The higher harmonics play a role close to the island separatrix (where the T profile has sharp changes in gradient) but decay to zero at larger values of X.

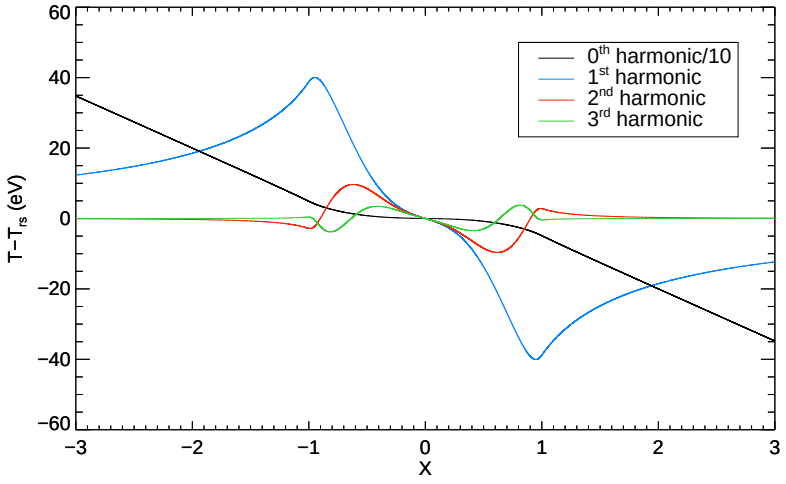

FIGURE 4.2: The first four Fourier harmonics of the magnetic island temperature perturbation, $T_n(X)$ (where $n = 0, 1, 2, 3$).

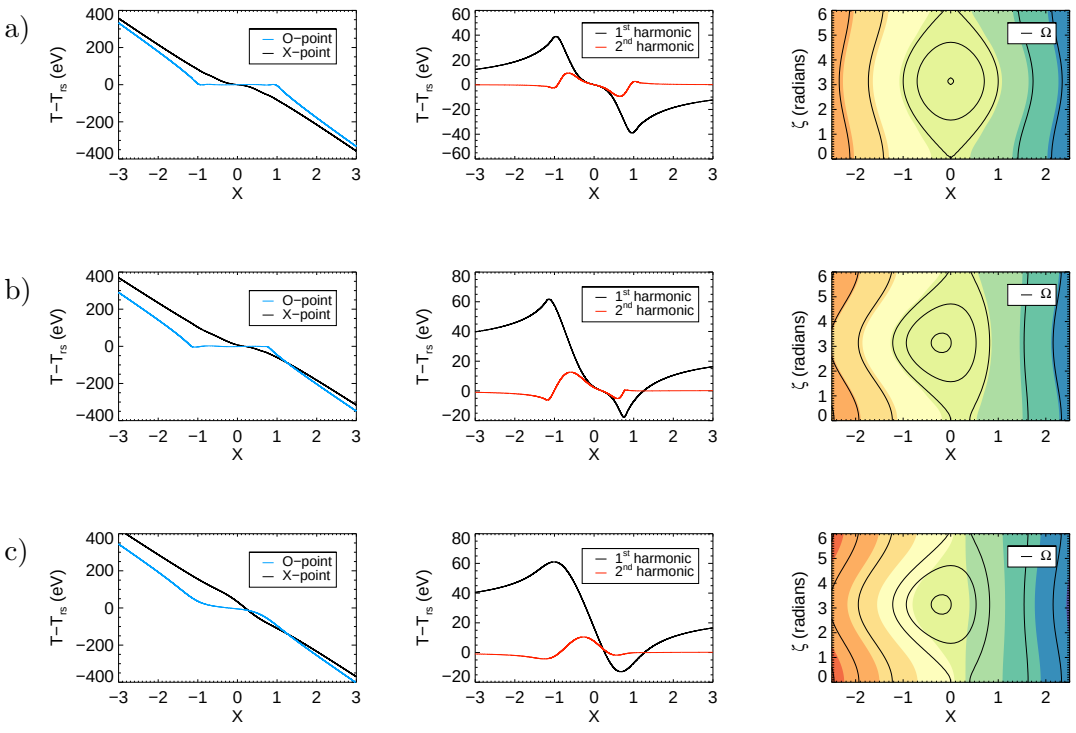

FIGURE 4.3: T_e around an NTM island. O and X point profiles (left), X dependence of 1st and 2nd harmonic of the helical temperature perturbation (middle) and 2D profile of $T(X, \zeta)$ (right). **a)** $A = 0$, $\frac{w_c}{w} = 0.1$ **b)** $A = 0.8$, $\frac{w_c}{w} = 0.1$ **c)** $A = 0.8$, $\frac{w_c}{w} = 0.4$.

Further examples of harmonics and reconstructed T profiles are plotted in figure 4.3. The plots in row **a** have $w_c/w = 0.1$ and $A = 0$. In row **b**, w_c/w remains at 0.1 but A is increased to 0.8. In row **c**, A remains at 0.8 but w_c/w is increased to 0.25. The increase in A between rows **a** and **b** causes the island and its T profile to become asymmetric. The Fourier harmonics also become asymmetric and the first harmonic now tends towards two different values at positive and negative large X, as given by the derived boundary condition. It can also be seen from the differences between the black line flux contours and the block colour temperature contours that there is indeed a region, close to the separatrix, in which perpendicular diffusion becomes important and the temperature is not a function of the island flux surfaces. From row **b** to row **c**, the width of this region can be seen to increase with w_c as shown by an increased 'smoothing out' of the sharp regions in the T profile. The increased perpendicular diffusion has a similar smoothing effect on the Fourier harmonics, which also become less sharp from row **b** to row **c**. In order to obtain a smooth solution, typically 12 Fourier harmonics are used to solve the heat transport equation but this is increased up to 24 for smaller values of w_c or larger values of A in order to resolve sharp gradient changes.

In order to compare to experimental data, the geometry of the model solutions can be described by a set of six free parameters; w, w_c, T'_{end} (the temperature gradient at large X), T_0 (the temperature at the rational surface), A and X_0 (a small shift in the X axis to correct for an inaccurate rational surface position). In Chapter 5, it is shown that the value of w_c can be inferred by fitting the solutions of the heat transport equation to experimental data, using these six free parameters.

4.4.1 Boundary layer width

Another point illustrated by the colour contour plots in figure 4.3 is that the boundary layer is wider at the X-point than at the O-point. This can be demonstrated by considering an approximation to the balance of parallel and perpendicular diffusion [1]:

$$\begin{aligned} \nabla_\parallel^2 T &\sim \frac{\chi_\perp}{\chi_\parallel}\nabla_\perp^2 T \\ \frac{k_\theta^2 X_T^2}{L_s^2} T &\sim \frac{\chi_\perp}{\chi_\parallel}\frac{T}{\delta_b^2} \end{aligned} \tag{4.31}$$

Here X_T is a length scale for the flattened region and δ_b is the boundary layer width. Rearrange to find δ_b:

$$\delta_b \sim \frac{L_s}{k_\theta X_T}\left(\frac{\chi_\perp}{\chi_\parallel}\right)^{\frac{1}{2}} \tag{4.32}$$

At the island O-point, $X_T \sim w$, which gives:

$$\delta_{b,O} \sim \frac{L_s}{k_\theta w}\left(\frac{\chi_\perp}{\chi_\parallel}\right)^{\frac{1}{2}} \sim \frac{w_c^2}{w} \tag{4.33}$$

At the island X-point, $X_T \sim \delta_{b,X}$, which gives:

$$\delta_{b,X} \sim \left(\frac{L_s}{k_\theta}\right)^{\frac{1}{2}}\left(\frac{\chi_\perp}{\chi_\parallel}\right)^{\frac{1}{4}} \sim w_c \tag{4.34}$$

As expected $\delta_{b,X} > \delta_{b,O}$. This result suggests that measuring the island X-point is important for inferring w_c. Similarly, as the island is at its widest at the O-point, a measurement at this phase is important for inferring w. This result will be revisited in Chapter 5.

4.5 Summary

This chapter described a heat transport equation for an asymmetric magnetic island, based on Fitzpatrick's transport threshold model [1]. The method for solving the 2D equation uses Fourier series for the helical direction and a finite difference scheme for the radial direction. Boundary conditions were derived by taking analytic limits of the equation far from the rational surface. The solutions of this equation are magnetic island temperature profiles, described by a set of six free parameters. The solution method was implemented in a FORTRAN routine that can be called repeatedly and quickly so that the temperature profiles can be fitted to both experimental and simulated Thomson scattering data. The data simulation and fitting procedures are described in Chapter 5.

Chapter 5

First measurements of the NTM temperature perturbation with Thomson scattering

5.1 Introduction

Chapter 4, described a heat transport equation for a magnetic island, the solutions of which are profiles of the NTM temperature perturbation. This chapter demonstrates a method for fitting these model profiles to experimental Thomson scattering data from the MAST tokamak using a set of six free parameters that describe the geometry of the perturbation, including w_c, which is an important parameter in the modified Rutherford equation for island evolution. The best fit value of this parameter can then be used as an experimentally measured estimate, avoiding the approximate analytic formula for w_c used in previous studies [41, 59, 63]. In section 5.3, this parameter estimation method is validated by fitting the model to simulated temperature profiles with a known value of w_c in a comprehensive set of simulated experimental scenarios. In section 5.4, an ensemble of NTM data from similar MAST discharges is used to provide a best estimate of w_c for these plasmas. This is the first time such a measurement has been made with Thomson scattering and on a spherical tokamak.

5.2 Thomson scattering data around a magnetic island

In conventional tokamaks, electron cyclotron emission (ECE) systems have previously been used to compare electron temperature profiles in the vicinity of magnetic islands to those predicted by transport models [35, 64]. In spherical tokamaks (STs), which have low outboard magnetic field, low ECE harmonics meet the cut-off density before leaving the plasma. Therefore, Thomson scattering (TS) is the preferred electron temperature diagnostic. In Chapter 2, MAST's eight Nd:YAG TS system was described [28]. It has 130 spatial points, a radial resolution of $\sim$ 1cm and can be fired in a burst to measure fast rotating phenomena [65]. The high spatial and temporal resolution has enabled this study of the temperature profiles of rotating NTM magnetic islands; the first investigation of its kind on an ST.

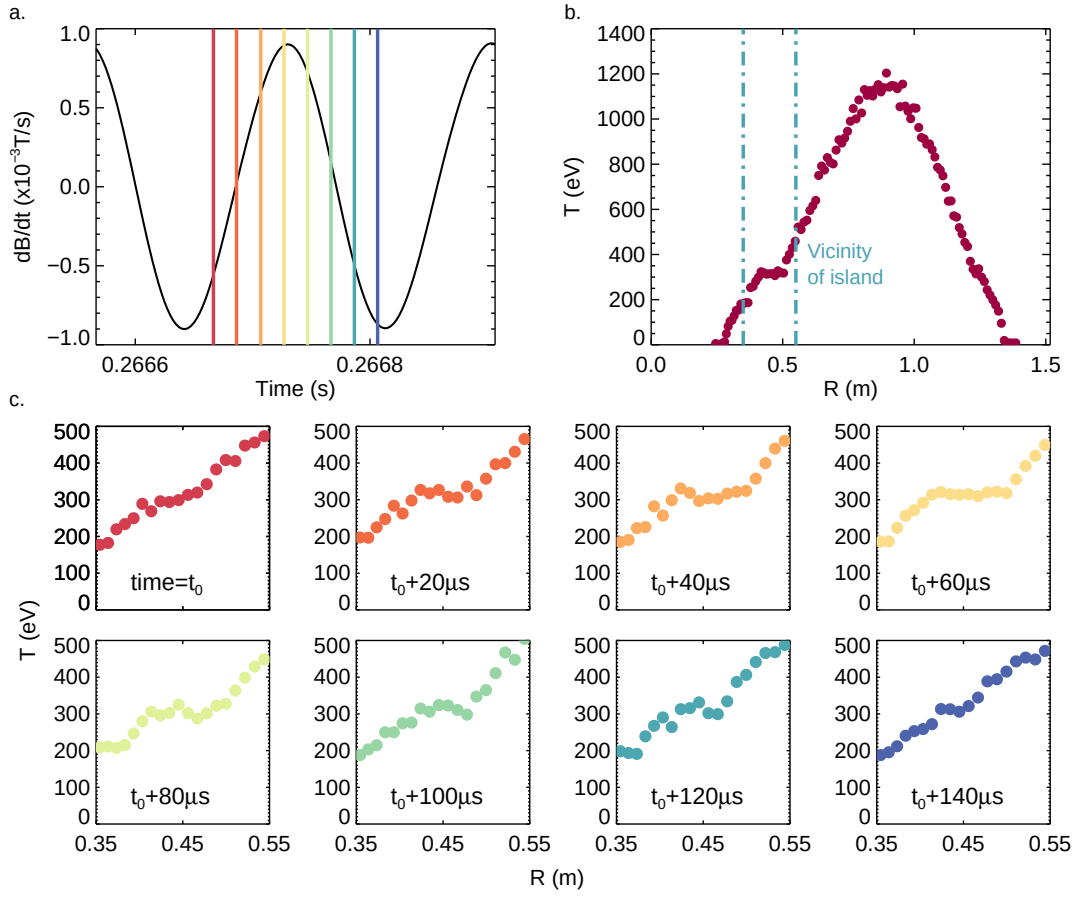

FIGURE 5.1: MAST discharge 24623. **a)** Mirnov coil signal with T_e profile timing indicated by coloured lines. **b)** Full T_e profile indicating region sectioned in c, around inboard $q = 2$ surface. **c)** Thomson scattering T_e profile sections in an 8 laser burst around a 2/1 NTM period. Laser 4 (yellow) is closest to the O-point and laser 8 (blue) is closest to the X-point.

Figure 5.1 shows an example of data from a burst of TS lasers around a 2/1 NTM in a MAST discharge and an example of the Mirnov coil signal induced by the magnetic island rotating past. The timing of the eight TS lasers is overlaid on the Mirnov signal to demonstrate the positions of the lasers at different phases of the island.

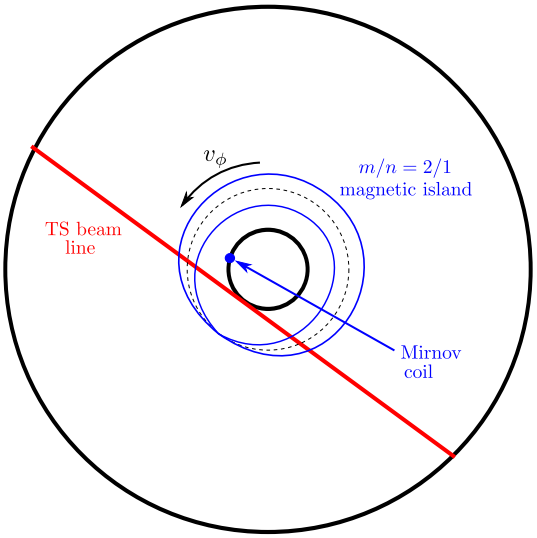

FIGURE 5.2: Plan view of the TS system and its inboard view of a rotating 2/1 magnetic island.

Figure 5.2 shows a cartoon plan view of the TS system and its inboard view of a 2/1 magnetic island. As was shown in Chapter 2, a Mirnov coil's signal varies sinusoidally in time as different phases of the magnetic island rotate past in the toroidal direction. Mirnov coil signal minima occur when the island X-point is closest to the coil and maxima occur when the O-point is closest. Using the relative positions of a Mirnov coil, situated on the tokamak midplane, and the TS beam line, the island phase at each TS measurement position can be calculated. The radial position of each point can be translated into equilibrium flux space, given by Ψ, using the EFIT equilibrium reconstruction (see Chapter 2). If the rational surface position, Ψ_s, and the island half-width, w, can be estimated then the Ψ data can be translated to the transport model radial coordinate, X, by subtracting Ψ_s and dividing by w. The parameter w is varied from its initial estimate during the fitting procedure as the TS data contains information about its value. Also, the parameter, X_0, introduced in Chapter 4, can be added to the X grid as a global correction to the initial estimate of Ψ_s.

Assuming the island structure grows on a much slower time scale than the rotation period, which was shown to be the case in Chapter 2, the process described above translates the TS data into a 2D temperature profile in the (X, ζ) coordinate system so that it can be compared to solutions of the transport model.

5.3 Thomson scattering data simulation

There are six parameters that define the geometry of a particular magnetic island temperature perturbation: w, w_c, T'_{end}, T_0, A, and X_0. The values of these parameters can be inferred from a particular measured temperature profile by performing a least-squares fit of the model profiles to the data, varying the six parameters to find the best-fit solution. In order to validate this approach to parameter estimation, the parameter uncertainties have been characterised by fitting solutions of the heat transport equation to simulated TS temperature profiles. The fitting procedures for the simulated data and real data share many of the same features and are therefore described in tandem.

The first step of the data simulation is to choose a scenario to be tested. Values must be picked for the six free parameters and the number and ζ locations of the lasers must be chosen. The X locations are set by the radial resolution of the system and are typically 15-20 points covering 15-20cm in real space. The heat transport equation is then solved to produce a 2D temperature profile with the geometry defined by the chosen set of parameters and sampled at the X and ζ locations of each TS measurement point. The final step of the data simulation is to add random Gaussian noise with a standard deviation of 5% to T at each TS measurement point (errors of this size are predicted for the TS system). The noise is produced using the Box-Muller method [68]. The simulated data is now complete and can be stored as $T_{\mathrm{data}}(X, \zeta)$ (an example of this simulated data is shown in figure 5.4).

Next, the best fit solution to the data is found. This step is the same whether simulated or real TS data is being used. First, an initial estimate of the expected best fit values of the six free parameters is required. The heat transport equation is then solved using these parameter values and spatially sampled to get $T_{\mathrm{model}}(X, \zeta)$. It is then necessary to calculate χ^2 using the formula:

$$\chi^2 = \sum_i \frac{(T_{\mathrm{data},i} - T_{\mathrm{model},i})^2}{\sigma_i^2} \tag{5.1}$$

where σ_i are the uncertainties on the measurements. The minimum of χ^2 in 6D free parameter space is then found using a Marquadt-Levenberg routine [69]. The best fit values of w, w_c, T'_{end}, T_0, A and X_0 are then recorded.

If real data is being used, the procedure is now complete and the best-fit parameter values can be used as experimental estimates. If simulated data is being used, a

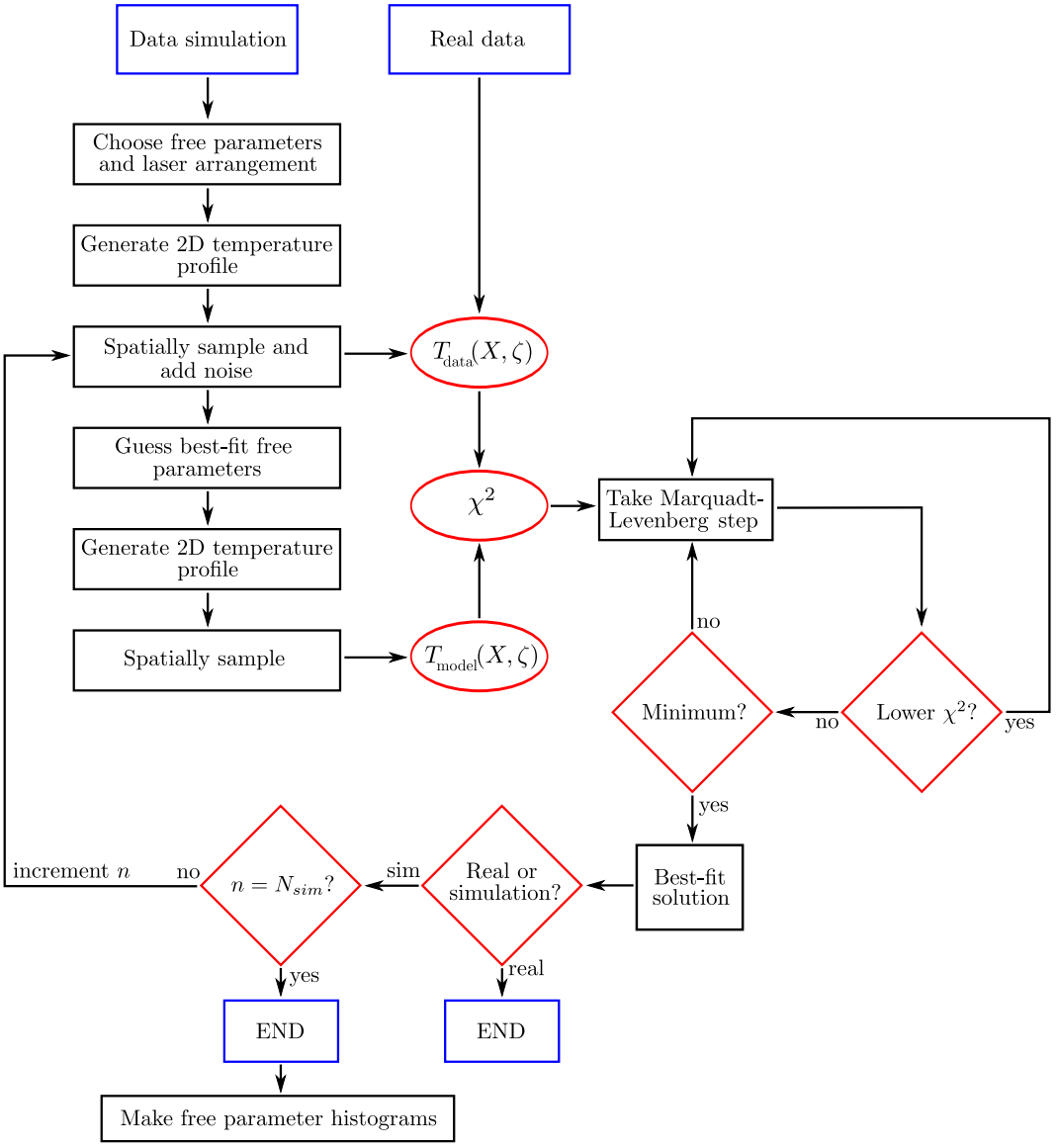

FIGURE 5.3: Flow chart for data simulation and least-squares fitting procedure.

new $T_{\text{data}}(X,\zeta)$ is created by generating a new set of random noise and repeating the subsequent stages. This is repeated several hundred times to build six free parameter value distributions. The number of repeated simulations in a distribution is denoted as N_{sim}. Finally, histograms for the free parameter value distributions are generated and Gaussian curves are fitted to estimate the mean and standard deviation values for the distributions. The mean values are compared to the initial parameter values chosen earlier. The proximity of the mean to this initial value gives an indication of how accurately the 'true value' of the parameter can be inferred from the data at this particular point in parameter space and with this particular arrangement of lasers. The standard

deviation gives the expected uncertainty on the measurement.

The process described above is summarised by the flow chart in figure 5.3.

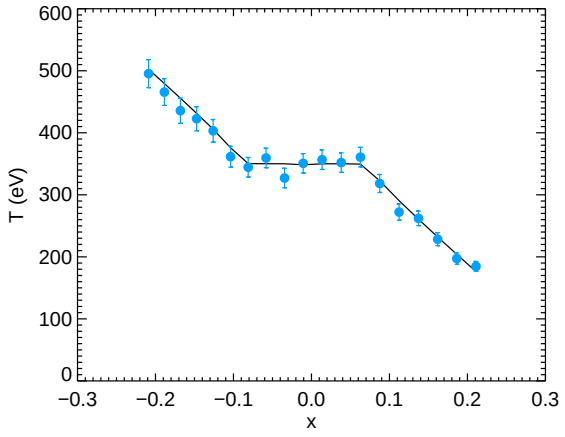

FIGURE 5.4: O-point profile across model solution (black line) which has been spatially sampled and had noise added (blue dots).

5.3.1 Contours of χ^2

The reduced χ^2 is defined as $\chi^2_{red} = \chi^2/\nu$ where ν is the number of degrees of freedom; the number of data points minus the number of free parameters. A standard indicator of a good quality of fit is that the minimum value of χ^2_{red} should be ≈ 1. It is of interest to examine the contours of χ^2_{red} for an individual fit to simulated data in various 2D slices through the 6D parameter space (see figure 5.5). The minimum values are all ≈ 1, showing that the quality of fit to the simulated data is as expected.

The forms of the χ^2_{red} contours around the minima reveal which parameters are well constrained and which parameters are correlated with one another. Correlations can also be investigated by calculating the Pearson's correlation coefficient for the simulated parameter distributions, obtained using the method above. Pearson's coefficient for parameters a and b, is given by:

$$\rho_{a,b} = \frac{\mathrm{cov}(a,b)}{\sigma_a \sigma_b} \tag{5.2}$$

where $\mathrm{cov}(a,b)$ is the covariance of a and b and σ_a and σ_b are the standard deviations. $\rho_{a,b}$ has a value of 1 for perfectly positive correlation between a and b.

Figure 5.5a shows the contours in the w, w_c plane. The angled minimum reveals a strong correlation between these two parameters, confirmed by a high Pearson coefficient

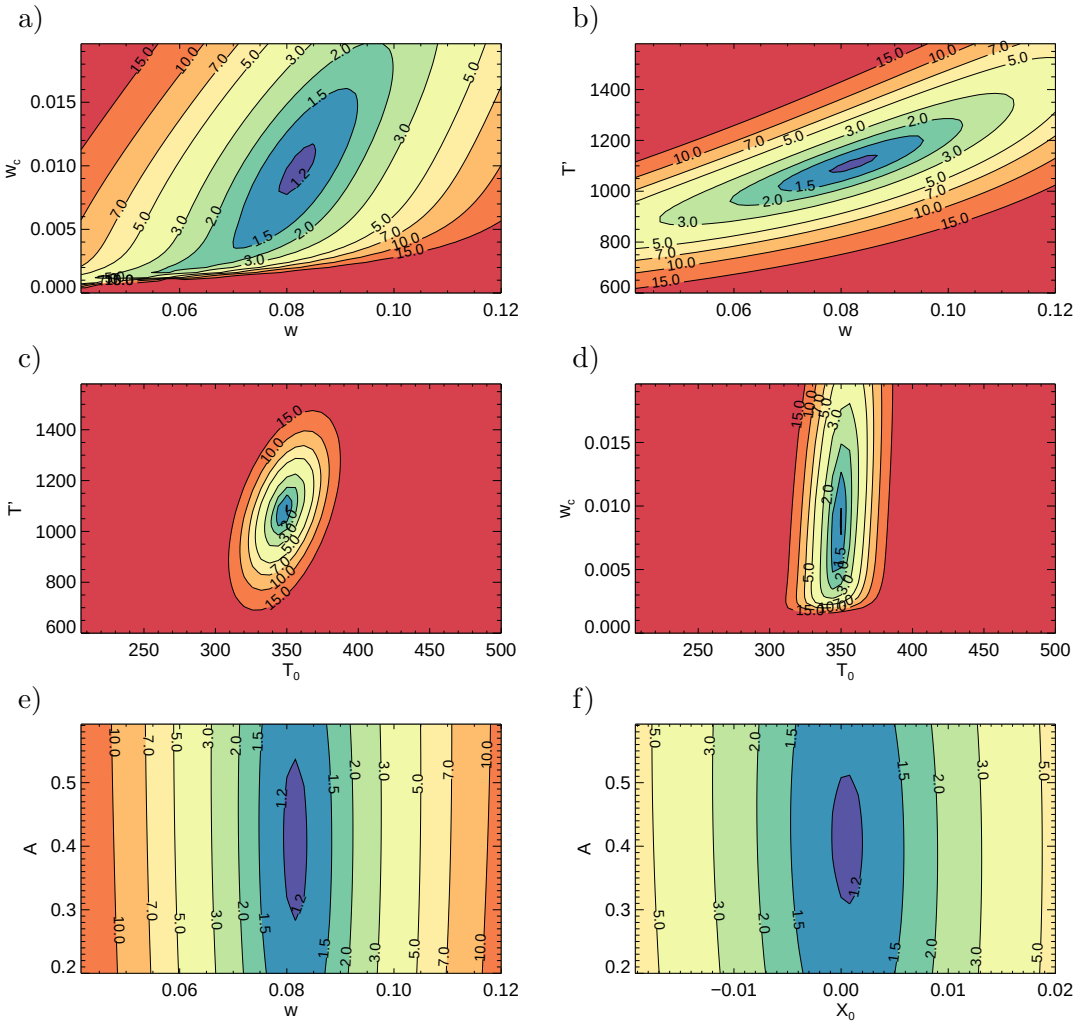

FIGURE 5.5: Contours of χ^2_{red} for an individual data simulation. **a)** w and w_c - input values are $w = 0.08$ and $w_c = 0.01$. **b)** w and T'_{end} - input values are $w = 0.08$ and $T'_{end} = 1100$. **c)** T_0 and T'_{end} - input values are $T_0 = 350$ and $T'_{end} = 1100$. **d)** T_0 and w_c - input values are $T_0 = 350$ and $w_c = 0.01$. **e)** w and A - input values are $w = 0.08$ and $A = 0.4$. **f)** X_0 and A - input values are $X_0 = 0$ and $A = 0.4$. Lengths are in units of normalised flux and temperatures in eV. A is dimensionless.

of $\rho_{w,w_c} \approx 0.85$ (the exact value depends on the arrangement of the lasers and the initial input values of the parameters for the simulated data). This correlation has important consequences for the inference of parameter values and will be revisited later. Figures 5.5c, d and f show that, as global parameters influenced by all data points, T_0 and X_0 are well constrained and have narrow χ^2_{red} minima. T'_{end} is also semi-global (all of the data points outside the island influence its value) and figures 5.5b, c show that it is quite well constrained. The broad minima in the A direction of figures 5.5e and f show that the parameter is quite poorly constrained. These qualitative descriptions inferred from the shapes of the χ^2_{red} surfaces are complemented by quantitative estimates of the parameter uncertainties in section 5.3.3.

The correlation between w and w_c can be understood by considering the geometry of the temperature perturbation. The cartoon in figure 5.6 gives a heuristic illustration of the origin of this correlation. The total width of the temperature perturbation, W_T, is defined as the horizontal distance between the two straight line sections of $T(X)$, either side of the island O-point. It can be seen that from the figure that W_T is related to the linear function $2w - 2w_c$. It is instructive to think of w_c as a measure of how much the equilibrium profile 'leaks' or diffuses into the island. An increase in w_c decreases the overall size of W_T as it causes the two straight line sections to move closer together. A given value of W_T can be obtained either by increasing both w and w_c or decreasing both w and w_c.

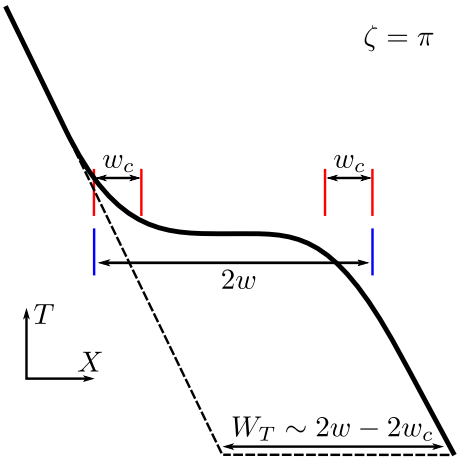

FIGURE 5.6: The origin of the correlation between w and w_c. W_T is the overall width of the temperature perturbation. An increase in w_c can decrease W_T.

Like T'_{end}, W_T is a well constrained semi-global parameter influenced by a large number of data points but, because of this correlation, the two parameters that contribute to it are less well constrained. This correlation means that an inaccurate estimate of w will lead to an inaccurate estimate of w_c. As the main reason for performing this analysis is to infer w_c, it is important to try and mitigate this effect. In fact, the correlation itself can be used to get a better estimate of w_c. If an independent estimate of w can be obtained from the amplitude of a Mirnov coil signal and introduced as a constraint on w, the uncertainties on w_c will be reduced. The method used to constrain w is described in section 5.3.2, below.

5.3.2 Constraining parameters

A parameter can be constrained using newly acquired information with a simple application of Bayes' theorem [70]:

$$P(\text{model}|\text{data}) \propto P(\text{data}|\text{model})P(\text{model}) \tag{5.3}$$

where $P(\text{model}|\text{data})$ is called the posterior probability density function (PDF), $P(\text{data}|\text{model})$ is called the likelihood PDF and $P(\text{model})$ is called the prior PDF. The likelihood is the probability that the observed data is described by a model with certain free parameters. The prior is a PDF of the model free parameters that has been previously obtained from some other information source. The posterior is the PDF for the model, which contains all the information from the data and any prior knowledge that has been obtained.

The information about w and w_c contained in the temperature data is accessed using the transport model. The likelihood for this system is given by:

$$P\left(T_{\text{data}}|T_{\text{model}}(w, w_c)\right) \propto \exp\left(-\frac{\chi^2}{2}\right) \tag{5.4}$$

where $\chi^2 = \sum_i (T_{\text{data},i} - T_{\text{model},i})^2/\sigma_i^2$, as before. An independent measurement of w can be obtained from a Mirnov coil, with a value w_{mag} and a standard deviation $\sigma_{w_{mag}}$. Assuming this measurement has a Gaussian uncertainty, the prior is given by:

$$P\left(T_{\text{model}}(w, w_c)\right) \propto \exp\left(-\frac{(w - w_{mag})^2}{2\sigma_{w_{mag}}^2}\right) \tag{5.5}$$

Thus the posterior probability density function describing the probability that w and w_c have particular values, given the temperature data and the prior magnetic measurement, is given by:

$$P\left(T_{\text{model}}(w, w_c)|T_{\text{data}}\right) \propto \exp\left(-\frac{\chi^2}{2}\right) \exp\left(-\frac{(w - w_{mag})^2}{2\sigma_{w_{mag}}^2}\right) \tag{5.6}$$

This PDF can now be turned into a modified χ^2 by taking the natural logarithm, ignoring the additional term due to taking the logarithm of the constant of proportionality and multiplying by -2:

$$\chi_{mod}^2 = \chi^2 + \frac{(w - w_{mag})^2}{\sigma_{w_{mag}}^2} \tag{5.7}$$

The $(w - w_{mag})^2/\sigma_{w_{mag}}^2$ term is the additional 'constraint' referred to in section 5.3.1. The effect of using such a constraint is demonstrated by two examples in section 5.3.3.

This method is also used to constrain free parameters in Chapter 6.

5.3.3 Data simulation results

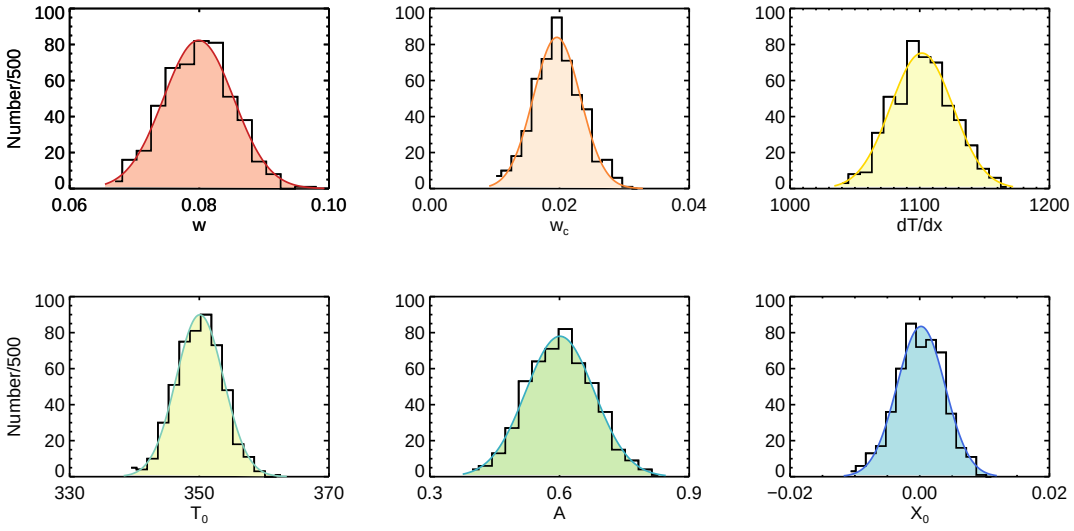

FIGURE 5.7: Histograms and fitted Gaussian functions for the six free parameters in a Thomson scattering data simulation with $N_{sim} = 500$. Input values are $w = 0.08$, $w_c = 0.02$, $T'_{end} = 1100$, $T_0 = 350$, $A = 0.6$, $X_0 = 0$. Lengths are in units of normalised flux and temperatures in eV.

Figure 5.7 shows an example of the six histograms of the best fit parameters for $N_{sim} = 500$. This example simulated eight lasers, evenly spaced across the interval $\zeta = 0$ to $\zeta = 2\pi$. The input values were $w = 0.08$, $w_c = 0.02$, $T'_{end} = 1100$, $T_0 = 350$, $A = 0.6$, $X_0 = 0$. The histograms are approximately Gaussian, with mean and σ obtained from a least-squares fit. The mean values of the histograms match their respective fitting parameter input values well. The calculated standard deviation values, as a percentage of the mean, are $\sigma_{w\%} = 7\%$, $\sigma_{w_c\%} = 19\%$, $\sigma_{T'_{end}\%} = 2.2\%$, $\sigma_{T_0\%} = 1.0\%$, $\sigma_{A\%} = 13\%$, $\sigma_{X_0\%} = 4.6\%$. The uncertainty on the rational surface position, $\sigma_{X_0\%}$, is taken as a percentage of w, as its mean value is close to zero. The relative sizes of these percentage errors match the qualitative estimates obtained from the χ^2 surfaces.

After estimating the uncertainty on the parameters at a single point in the 6D parameter space and with a single arrangement of lasers, a more detailed understanding of this inference method was obtained by repeating this process at different points in parameter space and with different numbers and arrangements of lasers. This analysis was conducted to find out whether there are optimum conditions under which to infer the values of the parameters. In particular, it is important to estimate the uncertainty on

measurements of w and w_c under different conditions, as they are the main parameters of interest for determining NTM stability.

Figure 5.8 shows the mean and σ of w and w_c for a series of $N_{sim} = 500$ simulation runs with varying numbers of lasers spread evenly over an island period. As before, the initial input values were $w = 0.08$, $w_c = 0.02$, $T'_{end} = 1100$, $T_0 = 350$, $A = 0.6$, $X_0 = 0$. Though the result is no surprise, it is important to note that the uncertainties on w and w_c decrease with increasing number of lasers, due to the increase in ζ resolution. Another point of interest is that the use of a single laser at the O-point constrains w reasonably well but leaves w_c poorly constrained, whereas a single laser at the X-point constrains w_c reasonably well but fails to constrain w. This is in agreement with the prediction from the boundary layer width calculation, made in section 4.4.1, that a measurement of the O-point is required to infer w and a measurement of the X-point is required to infer w_c.

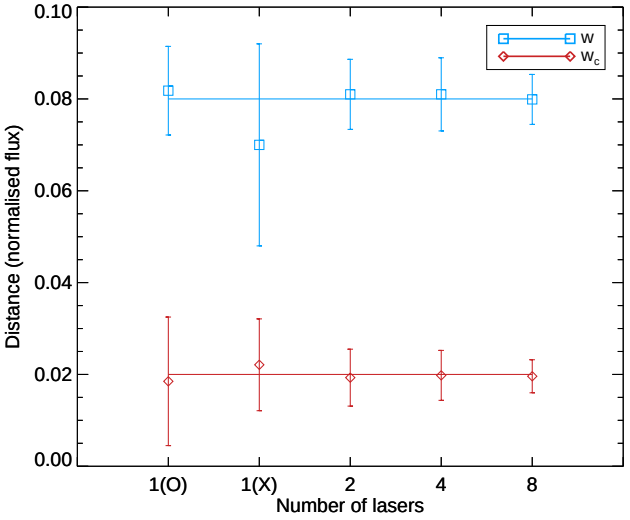

FIGURE 5.8: Errors on w (blue line with squares) and w_c (red line with diamonds) as a function of the number of TS lasers used (spread evenly over a 2π island period).

Although it is possible to obtain reasonable estimates of w and w_c with two or four lasers, eight lasers are typically used as this provides the best possible estimate available. Using fewer lasers could be favourable in future experiments, as it would allow more measurements of w and w_c to be made per discharge. However, it would have to be ensured, using the triggering system, that the lasers were fired over the X and O-points, in order to constrain w and w_c.

The different arrangements of the eight lasers, shown in figure 5.9, are now considered. Figure 5.10 shows the mean and σ of w and w_c for a series of $N_{sim} = 500$ simulation

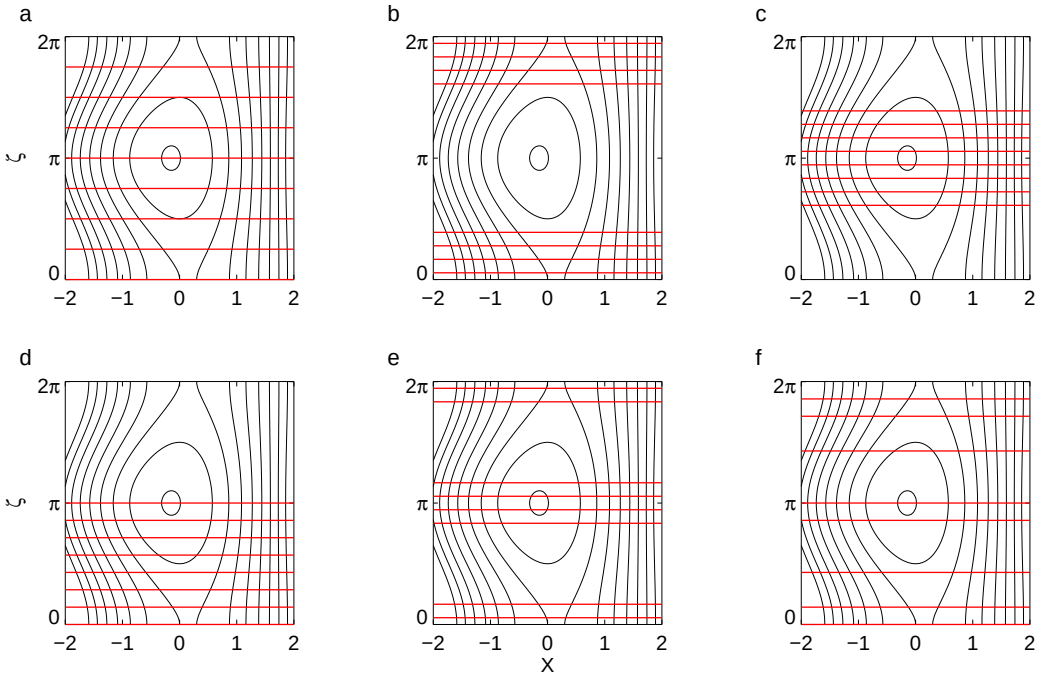

FIGURE 5.9: The eight TS lasers in a series of different arrangements of ζ values.

runs using these arrangements.

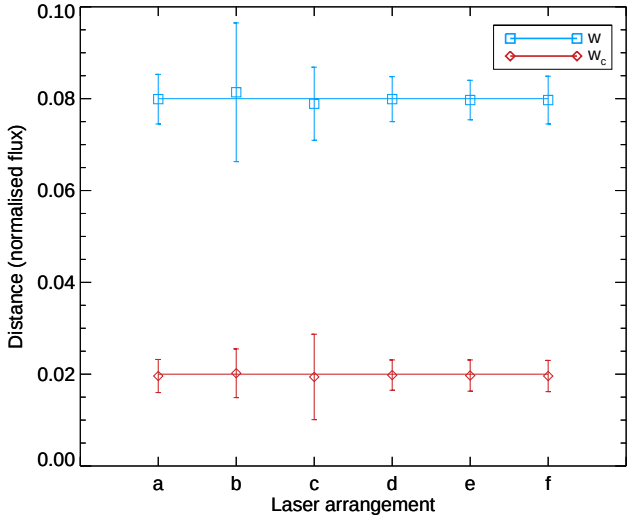

FIGURE 5.10: Errors on w (blue line with squares) and w_c (red line with diamonds) as a function of the laser arrangement. Laser arrangements shown in figure 5.9.

As in the previous example, the initial input values were $w = 0.08$, $w_c = 0.02$, $T'_{end} = 1100$, $T_0 = 350$, $A = 0.6$, $X_0 = 0$. Arrangements **b** and **c**, which miss out the O-point and X-point, respectively, have larger uncertainties. As with figure 5.8, the lack of O-point measurement means that w is poorly constrained and the lack of X-point measurement means that w_c is poorly constrained. Furthermore, due to the

correlation between w and w_c, arrangements **b** and **c** show that increased uncertainty on one parameter also increases the uncertainty on the other parameter. Overall, the other arrangements give similar results and it is difficult to say whether small differences between them are due to statistical fluctuations or marginal improvements. Most of the experimental data used in the rest of this chapter uses arrangements **a** and **d**.

As was mentioned earlier, the main parameter of interest is w_c as inferring its value experimentally means that the use of analytic approximations can be avoided. In Chapter 6, the value of w_c inferred from TS temperature profiles is compared to that inferred from a β ramp-down experiment. A further set of $N_{sim} = 500$ runs was conducted to simulate a β ramp-down experiment by reducing w while keeping w_c constant. The aim of this simulation is to see if there is an optimum w at which to measure w_c. The value of w_c chosen was 0.01 (flux units) as this is approximately the value obtained in fits to real data (see section 5.4). The results are shown in figure 5.11.

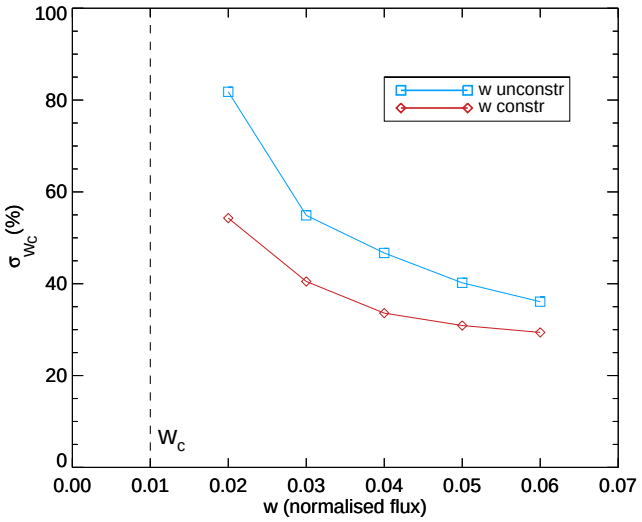

FIGURE 5.11: Error on w_c as a function of w. Simulation of a β ramp-down. Red line with diamonds is for a fit with constrained w, assuming w is known within 10% of the saturated w. Blue line with squares is for the unconstrained case. The reduced errors for the constrained case are due to the correlation between w and w_c.

As w approaches w_c, perpendicular diffusion becomes important and the blurred island edges make w difficult to determine, increasing its uncertainty (as was shown in the colour contour plots of the island temperature profile in Chapter 4). Since w and w_c are correlated, the uncertainty on w_c is also increased. This result shows that, though the effects of diffusion are most relevant for small islands, a combination of parameter correlation and spatial resolution make directly measuring those effects extremely challenging. In fact, counterintuitively, more reliable information about the threshold can

be gained by measuring larger islands, because w can be inferred more accurately. It is important to note that this is only the case if it is assumed that the thermal diffusivities do not change significantly between island saturation and island threshold. The red line in figure 5.11 shows that introducing a w constraint, such as an independent Mirnov coil measurement (see Chapter 6), can at least partially mitigate this effect.

A final set of $N_{sim} = 500$ simulation runs was conducted with varying w_c values. The aim of this simulation was to investigate the extent to which different sized w_c values can be resolved. The value of w was fixed at 0.08 (flux units). The results are shown in figure 5.12.

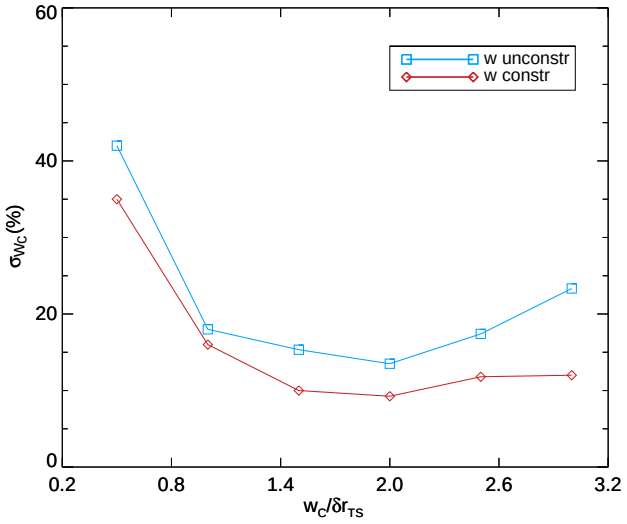

FIGURE 5.12: Error on w_c as a function of $w_c/\delta r_{TS}$ where δr_{TS} is the radial resolution of the MAST TS system ($\sim 1cm$). Red line with diamonds is for a fit with constrained w, assuming w is known within 10%. Blue line with squares is for the unconstrained case. The reduced errors for the constrained case are due to the correlation between w and w_c.

Again, when w_c gets large (beginning to approach w), the blurred island edges act to increase the uncertainty on both w and w_c. The error on w_c also increases as w_c gets smaller, due to the finite resolution of the TS system. These two error dependences, illustrated in figure 5.12, give rise to an optimum ratio w_c/w at which the errors on w_c are minimised. For this example, the optimum ratio is $w_c/w \approx 0.4$, which again suggests that w_c is best inferred when the island is not too close to the threshold. As with the previous example, figure 5.12 also demonstrates that the error on w_c can be reduced by constraining w using magnetic measurements. It is of interest to note that a useful estimate can be obtained even if w_c falls below the radial resolution of the TS system.

As w_c affects the T_e contours right across the profile, the extra information provided by multiple lasers in the ζ direction constrains the value of w_c when $w_c/\delta r_{TS} \lesssim 1$.

The conclusion of this analysis of synthesised data is that w_c can be inferred from TS data, assuming the model is valid, and provides an estimate of the uncertainty that can be used when analysing real data. For a reliable measurement of w and w_c, it is crucial that both the O-point and X-point are measured. It is also important that the measurement be made when w is not too small, as the increased uncertainty on w and the correlation between w and w_c act to increase the uncertainty on w_c. If a reliable constraint on w can be applied then this effect can be partially mitigated.

5.4 Results using real MAST Thomson scattering data

After validating this approach to estimating w_c, the model solutions, $T(X, \zeta)$, were fitted to experimental TS data in order to estimate w_c for a series of 13 similar MAST discharges with 2/1 NTMs, the characteristics of which are described in Chapter 2. The temporal evolution of magnetic island widths in a selection of these discharges is discussed in Chapter 6.

Data from both the inboard and outboard sides of MAST are available but this analysis focuses on the inboard data because the radial resolution is higher close to the central column, due to both flux expansion and the tangential trajectory of the TS laser beam line (see Chapter 2).

For this data set, the majority of the islands are measured in, or close to, their saturated state, with a full width in the range ∼7-10cm. Measuring the islands of this size provides a favourable ratio of w_c/w for minimising the uncertainty on w_c. Estimates of the magnetic island width taken from a Mirnov coil, with an assumed uncertainty of 10%, were used to constrain w and therefore reduce the uncertainty on w_c (the method for estimating w from Mirnov signals is described in Chapter 6). Two examples of the T_e data, in the vicinity of the island, along with the best-fit solutions are shown in figure 5.13.

In order to get a best estimate for w_c, data from multiple discharges in similar parameter regimes can be used. One method for estimating w_c is to use the formula $w_c = \left(\frac{\chi_\perp L_s^2}{\chi_\parallel k_\theta^2}\right)^{\frac{1}{4}}$ with analytic estimates for $\chi_\perp$ and $\chi_\parallel$. The perpendicular transport in tokamaks, although widely attributed to small scale turbulence [71], is not well described

23447

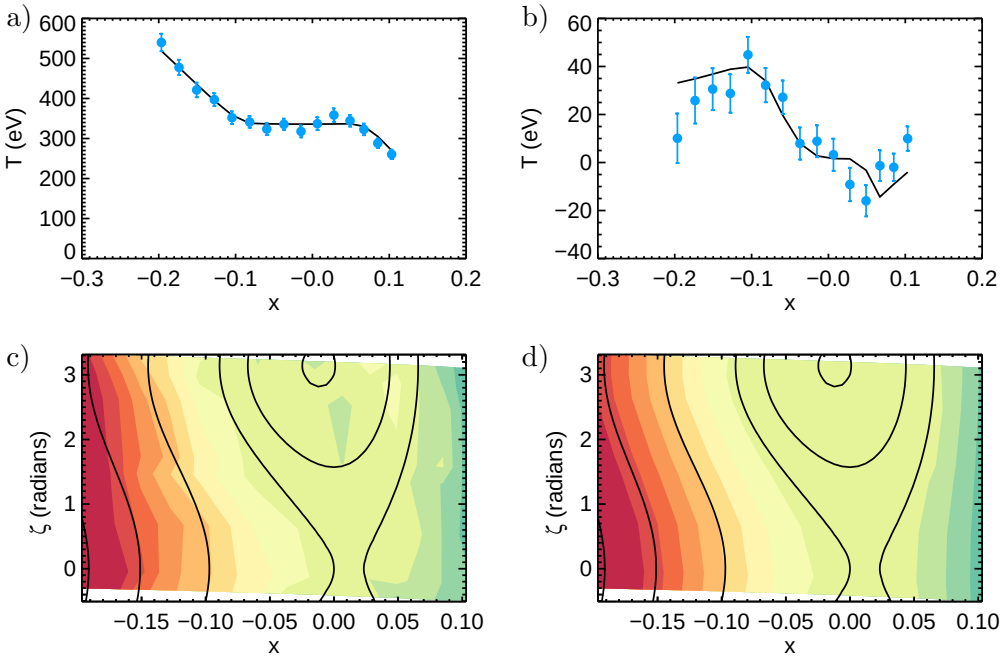

24623

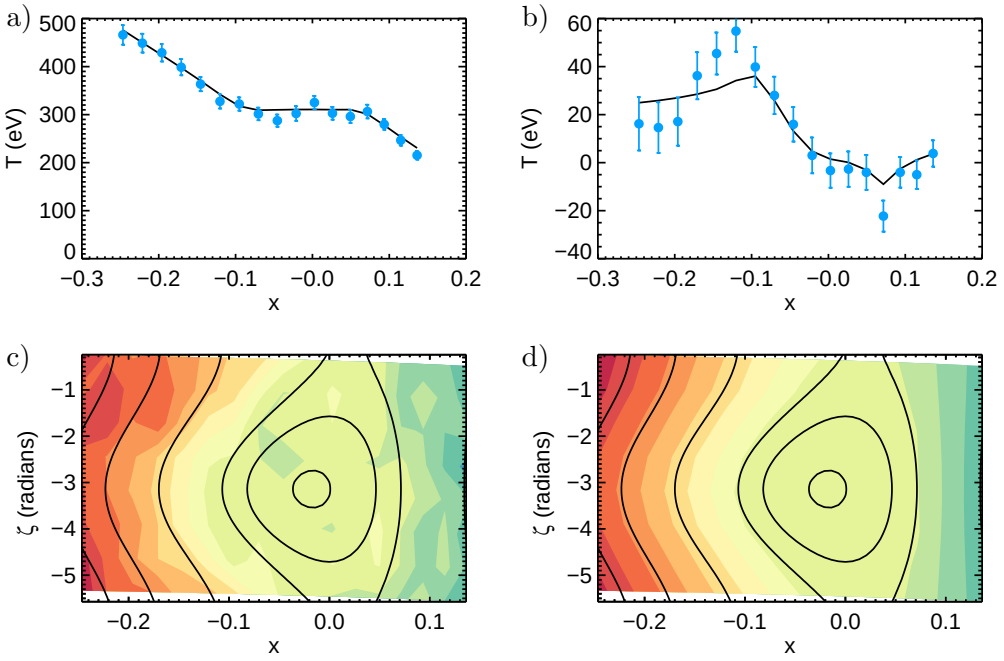

FIGURE 5.13: MAST discharges 23447 and 24623. A fit of model, $T(X, \zeta)$ to TS data. **a)** A profile close to the O-point of the island, black solid line showing best-fit model and blue dots showing data. **b)** The 1st Fourier harmonic of the helical T_e perturbation, black solid line showing best-fit model and blue dots showing data. **c)** Shaded contours of T_e data with best-fit contours of Ω over-laid. **d)** Shaded contours of best-fit model T_e with best-fit contours of Ω over-laid.

quantitatively and as such is known as 'anomalous transport'. Here, a gyro-Bohm model is used as a rough estimate for $\chi_\perp$, with the following forumla:

$$\chi_\perp \sim \rho_i^2 v_{th,i}/r \tag{5.8}$$

The parallel diffusivity, $\chi_\parallel$, is sometimes estimated using a formula which corrects the conductive Spitzer-Harm formula with a factor taking into account the ratio of the electron mean free path to L_c [35] to provide a pseudo-convective $\chi_\parallel$ given by equation 5.9 for MAST plasmas (n_{19} is the electron density in units of $10^{19}m^{-3}$).

$$\chi_\parallel \sim 1.2 \times 10^{10} T_{keV}^{\frac{5}{2}}/n_{19} \tag{5.9}$$

Using this method, the value of w_c is then estimated for the 13 discharges considered here. The mean of this distribution of w_c values is 0.5cm and the standard deviation is only 8% (recall that $\chi_\perp/\chi_\parallel$ has quarter power dependence in equation 4.3, which acts to reduce any variation). As there is a great deal of uncertainty in the validity of the models of $\chi_\perp$ and $\chi_\parallel$ used, the means value can only really act as an order of magnitude estimate, but the low standard deviation suggests that the transport properties in these discharges are similar. This standard deviation is smaller than the usual uncertainty on w_c, estimated in section 5.3.3, and it is therefore assumed that a better estimate for w_c can be obtained by combining the experimentally inferred values from the multiple discharges.

As the data simulation method for estimating σ_{w_c} described in section 5.3 provides a Gaussian probability density function (PDF) for w_c for each discharge, the joint PDF is obtained simply by multiplying together the individual PDFs to give a weighted mean. The final joint mean and error for the discharges is $w_c = 0.7 \pm 0.2$cm, consistent with the order of magnitude estimate described above.

Translating this measured w_c into a ratio of thermal diffusivities gives a value in the range $\frac{\chi_\parallel}{\chi_\perp} = 6 \times 10^6 - 7 \times 10^7$ (uncertainties are large as $\frac{\chi_\parallel}{\chi_\perp} \propto w_c^4$). This is somewhat lower than the values of $\frac{\chi_\parallel}{\chi_\perp} = 10^8 - 10^9$ found by Meskat [35] on ASDEX and $\frac{\chi_\parallel}{\chi_\perp} = 10^8$ found by Hölzl [64] on TEXTOR. TEXTOR generally operates at lower density than MAST and ASDEX is generally hotter and less dense than MAST. If equations 5.8 and 5.9 are assumed to be valid then $\chi_\parallel \propto T^{\frac{5}{2}}/n$ and $\chi_\perp \propto T^{\frac{3}{2}}$, which leads to the relation $\frac{\chi_\parallel}{\chi_\perp} \propto \frac{T}{n}$. This scaling of temperature and density fits qualitatively with the observation

that $\frac{\chi_\parallel}{\chi_\perp}$ is higher on hotter, less dense tokamaks. However, this is rather simplistic as the magnetic field strength and other equilibrium parameters are also likely to play a significant role in determining the turbulent perpendicular transport and therefore predictions for ITER on the basis of this observation are not included here.

The directly measured value of w_c, described above, has been used in an analysis of the modified Rutherford equation (see Chapter 3) for the evolution of the NTMs in these MAST discharges. This analysis is described in detail in Chapter 6.

5.5 Summary

This chapter has outlined a method of inferring w_c, an important parameter in determining NTM stability, from experimental Thomson scattering data. The advantage of this method is that it avoids the need to choose a model for $\chi_\perp$ and $\chi_\parallel$, which previous studies of NTM stability [41, 59, 63] have required. In Chapter 4, a heat transport equation for an asymmetric magnetic island, based on Fitzpatrick's transport threshold model, was presented. The solutions of this equation are magnetic island temperature profiles, described by a set of six free parameters. With spatial sampling and the addition of randomly sampled Gaussian distributed noise, these profiles can be used to generate synthetic MAST Thomson scattering (TS) T_e data. By fitting the solutions to the synthetic TS data, the uncertainties on the six free parameters can be estimated. A comprehensive set of simulation runs was conducted, investigating several regions within the parameter space as well as different numbers and arrangements of lasers. It was found that the geometry of the temperature perturbation causes the parameters w and w_c to be correlated and that, by constraining w with a magnetic amplitude estimate, the uncertainties on w_c can be reduced. Finally, the model T profiles were fitted to MAST T_e data for an ensemble of similar discharges with saturated 2/1 NTMs. From this analysis, an estimate of $w_c = 0.7 \pm 0.2$cm was inferred for these MAST discharges.

Chapter 6

Neoclassical tearing mode stability analysis on MAST

6.1 Introduction

A number of stabilising and destablising contributions govern NTM stability. The net effect of these contributions can be studied using the modified Rutherford equation (MRE), presented in Chapter 3, which describes the evolution of the magnetic island width, W. In this chapter, a method for estimating W is presented and the MRE is evaluated for a series of MAST discharges. The balance of the different contributions is characterised for the discharges and a possible explanation for the observed 'triggerless' NTMs is found. The uncertainties for the different contributions, which have been neglected in most previous analyses [41, 63, 72], are calculated by propagating the uncertainties on the measured parameters through the MRE analysis. This method also helps to keep track of correlations between terms in the MRE due to their shared dependences on measured parameters. Finally, a comparison is made between the NTM threshold predicted by the direct experimental estimation of w_c obtained in Chapter 4 and the threshold observed in two β ramp-down experiments. Though some adjustments are required to take account of interactions with other instabilities, the results from the MRE agree well with the observed behaviour. These comparisons indicate that the transport model outlined in Chapter 4, influenced by the measured w_c, plays an important role in explaining the observed threshold for these discharges. Uncertainties on the contribution from the polarisation current are significant and make it difficult to judge the importance of this threshold mechanism.

6.2 The modified Rutherford equation for NTM evolution

The modified Rutherford equation was presented in Chapter 3 as:

$$\frac{\tau_r}{r_s}\frac{dW}{dt} = r_s\Delta' - a_{nl}W + \Delta_{bs}(W) + \Delta_{GGJ}(W) + \Delta_{pol}(W) \tag{6.1}$$

Here, τ_r is defined as the current diffusion time and r_s as the minor radius of the rational surface. The first term on the right hand side of equation 6.1, $r_s\Delta'$, is related to the free energy available for magnetic reconnection in the current profile and is known as the classical tearing stability index [33]. The second term, $a_{nl}W$, describes the nonlinear evolution of the classical tearing mode, leading to saturation, and is related to higher order derivatives of the current profile [58]. Δ_{bs} is the contribution from the perturbation to the bootstrap current caused by the flattening of the pressure profile by the magnetic island associated with the mode. As has been shown in Chapters 3 and 4, islands smaller than a critical island width, w_c, do not completely flatten the profile, which leads to a threshold island width, w_{th}, above which the NTM grows [1]. Δ_{GGJ} is the contribution from the stabilising effect of magnetic field curvature [50]. This is particularly important in the MAST plasmas reported here due to the low aspect ratio and high level of plasma shaping [41]. The final term is due to the polarisation current, which is predicted to play a significant role when the island is small [55, 73, 74].

The evolution of the magnetic island width, W, is found by integrating the MRE with respect to time. One of the main aims of this chapter is to compare this theoretically predicted $W(t)$ with the experimentally observed $W(t)$. A method for experimentally inferring W from magnetic perturbation measurements is outlined below, in section 6.3.

6.3 Calculating the magnetic island width from Mirnov coil signals

Using the equation for the island half width in cylindrical geometry, which was presented in Chapter 3, the equation for the full-width, W, can be written down:

$$W = 4\sqrt{\frac{r_s q_s \tilde{B}_r}{m q_s' B_\theta}} \tag{6.2}$$

where q_s is the q value at the rational surface, $\tilde{B_r}$ is the amplitude of the perturbed radial magnetic field at the rational surface, m is the poloidal mode number, q_s' is the gradient of q with respect to r at the rational surface and B_θ is the poloidal field at the rational surface. The only part of this equation that cannot be evaluated from a simple mode number analysis and equilibrium construction is $\tilde{B_r}$. However, a number of measurements of the perturbed vertical field, $\tilde{B_z}$, are available at the locations of the Mirnov coil array, described in Chapter 2. As $\tilde{B_z} \propto \tilde{B_r}$ [75], an estimate for W can be obtained if the constant of proportionality relating $\tilde{B_r}$ at the rational surface to $\tilde{B_z}$ at a coil can be calculated, assuming the cylindrical approximation holds.

Following a similar method to that followed by Scarabosio [76] and in the TORFLD code [77], a routine was written to generate synthetic Mirnov coil array data using the magnetic field produced by a set of current filaments within the plasma. The filaments are assumed to be rotating toroidally at a constant frequency so that the time integrated Mirnov signal, $\int \frac{d\tilde{B_z}}{dt}.dt$, is equivalent to a series of toroidally separated measurements of $\tilde{B_z}$. The filaments lie in a sheet on the rational surface and follow equilibrium magnetic field lines, the trajectories of which are found using an equilibrium reconstruction. For R and Z points restricted to the rational surface, the field lines follow constant values of the helical angle:

$$\zeta = m\left(\theta^\star - \frac{\phi}{q_s}\right) \tag{6.3}$$

where the $\theta^\star$ coordinate replaces θ to provide a realistic field line trajectory. As magnetic field lines are straight in the $(\theta^\star, \phi)$ plane, this is often known as the straight field-line coordinate system. This is calculated by considering the local magnetic field pitch, given by equation 6.4, which is not constant on a flux surface.

$$\frac{d\theta}{d\phi} = \frac{B \cdot \nabla\theta}{B \cdot \nabla\phi} \tag{6.4}$$

The transform to $\theta^\star$ can be found by substituting the equation for the magnetic field, $\mathbf{B} = I(\Psi)\nabla\phi + \nabla\Psi \times \nabla\phi$, into equation 6.4, giving:

$$\underbrace{\nabla\Psi \times \nabla\phi \cdot \nabla\theta}_{J} \cdot \frac{\partial\theta^\star}{\partial\theta} = \frac{I(\Psi)}{qR^2} \tag{6.5}$$

Here, J is the Jacobian of the transform from toroidal coordinates into cylindrical coordinates, given by:

$$J = \frac{\partial \Psi}{\partial R}\frac{(R - R_0)}{r^2} + \frac{\partial \Psi}{\partial Z}\frac{Z}{r^2} \tag{6.6}$$

Then by integrating with respect to θ, equation 6.7 for $\theta^\star$ is obtained.

$$\theta^\star(\theta) = \frac{I(\Psi)}{q(\Psi)}\int_0^\theta \frac{d\theta}{R^2 J} + C \tag{6.7}$$

The unknown constant C is then found by normalising to 2π.

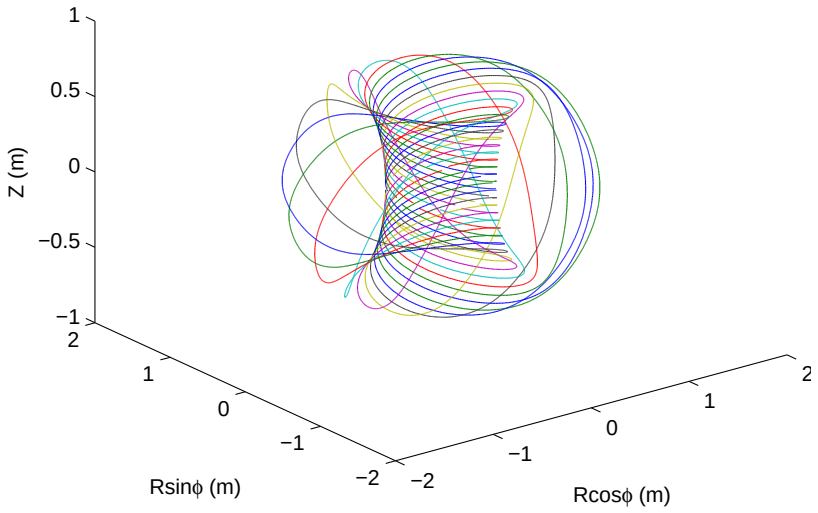

FIGURE 6.1: 16 $q = 2$ filaments following field lines on the MAST $q = 2$ surface.

Figure 6.1 shows 16 $q = 2$ filaments following field lines on the MAST $q = 2$ surface. Each filament carries current, $I_f(\zeta)$. The variation of I_f and therefore the island structure is given by $I_f = I_0 \sin\zeta$ for a single helicity perturbation. Using the Biot-Savart law, the magnetic field due to the current filaments can be found at the locations of the Mirnov coil array. The magnetic island current is not the only signal picked up by the real Mirnov coils. The rotating magnetic island induces eddy currents in the conducting wall that generate a reflection of the magnetic island signal. Scarabosio [76] used a full wall model and showed that, for rotation frequencies greater than 1kHz, the perturbation is reflected almost perfectly and the measured signal is effectively double that which would be measured without a conducting wall. As the magnetic islands on MAST typically rotate at about 10kHz, it is assumed the Mirnov signal due to the magnetic

island can be found simply by dividing the total measured signal by two. This approach has also been validated by previous modelling of the MAST vacuum vessel [78].

The Mirnov array data can then be simulated and fitted to experimental data (time integrated to give $\tilde{B}_z$), using a vector of N_I current filament values, $\underline{I}_f$, as free parameters. This method has been implemented in the MINERVA framework for Bayesian inference and has similarities to that used in Svensson 2008 [79]. This is a relatively simple model that does not take full advantage of the MINERVA framework but there is potential for developing it further and this is discussed in Chapter 7.

As there is a linear relationship between the current in an individual filament and the resulting magnetic field measured at a coil in the array, the entire system can be represented by the matrix equation:

$$\underline{P} = \underline{\underline{M}}\ \underline{I}_f \tag{6.8}$$

where $\underline{P}$ is a vector of N_M predicted Mirnov measurements and $\underline{\underline{M}}$ is a matrix of coefficients. If the vector of real Mirnov measurements, $\underline{\tilde{B}}_z$, has Gaussian uncertainties, and a covariance matrix, $\underline{\underline{\Sigma}}$, the probability density function (PDF) for the observed data, given the currents, is given by:

$$p(\tilde{B}_z|I_f) = \frac{1}{(2\pi)^{N_M/2}|\underline{\underline{\Sigma}}|^{1/2}} \exp\left(-\frac{1}{2}(\underline{\underline{M}}\ \underline{I}_f - \underline{\tilde{B}}_z)^T \underline{\underline{\Sigma}}^{-1}(\underline{\underline{M}}\ \underline{I}_f - \underline{\tilde{B}}_z)\right) \tag{6.9}$$

The mean of this multivariate normal distribution, given by equation 6.10, is taken as the best-fit of the currents [79].

$$\underline{m}_{I_f} = (\underline{\underline{M}}^T \underline{\underline{\Sigma}}^{-1} \underline{\underline{M}})^{-1} \underline{\underline{M}}^T \underline{\underline{\Sigma}}^{-1} \underline{\tilde{B}}_z \tag{6.10}$$

An example of the Mirnov array data and the best-fit simulated data is shown in figure 6.2.

Finally, it is possible to obtain the coefficient of proportionality between $\tilde{B}_z^{\text{coil}}$ and $\tilde{B}_r$ and make an estimate of W based on equation 6.2. For fits to real MAST data this gives perturbed current amplitudes on the order of I_0 =1kA for a saturated 2/1 NTM with $W \approx 10cm$.

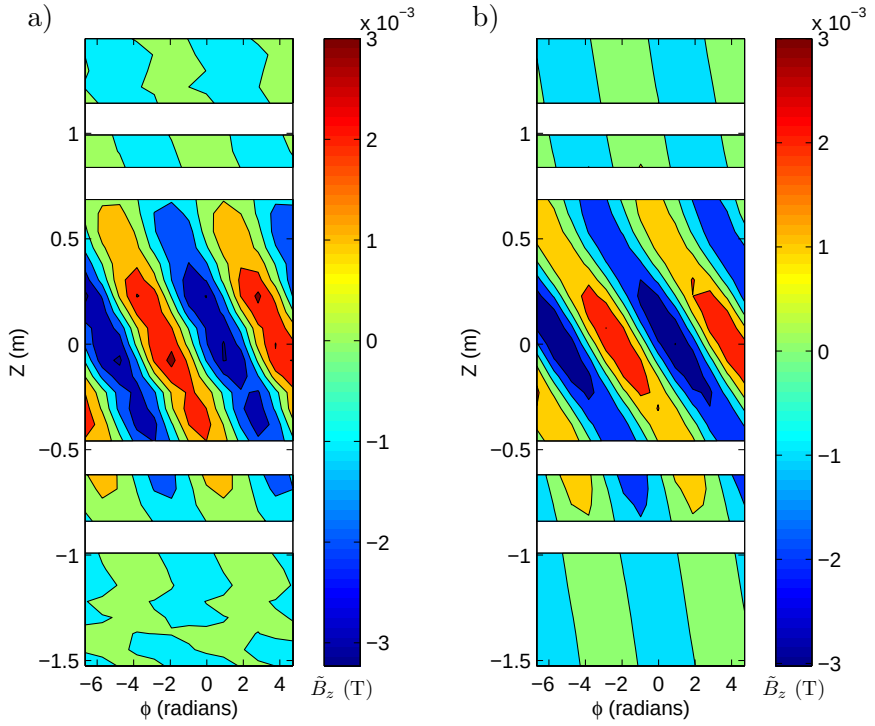

FIGURE 6.2: **a**) Real and **b**) simulated data from the MAST inboard Mirnov coil array for a saturated 2/1 NTM. White bands are broken coils.

There are limitations to this model, such as the approximation that the current perturbation lies in an infinitesimally thin sheet and the fact that it is a simple vacuum model that neglects any effect of the plasma itself. However, the values of W obtained with this method have been checked against successful measurements of large saturated island widths using all 8 lasers of the Thomson scattering system and are found to be in agreement. Errors on the calculated W calibration factor are estimated to be about 10%, which as Chapter 4 showed, can provide a useful constraint on the transport model. The rest of this chapter focuses on a study of the evolution of W, calculated using the method presented here, in a series of high performance MAST discharges.

6.4 High performance MAST discharges

Chapter 2 covered the basic characteristics of the high performance MAST discharges used in this thesis. In this chapter, the growth of 2/1 NTMs in three of these discharges is analysed in more detail. The discharges have similar electron pressure profiles and q profiles, with slightly reversed magnetic shear in the core and $q_0 > 1$ (see figure 6.3). The discharges are also characterised by reaching a high $\beta_N = \beta/(I_p/aB)$ of $\sim$4, usually in ELM-free H-mode. Figure 6.4 shows NTM evolution, from onset to saturation

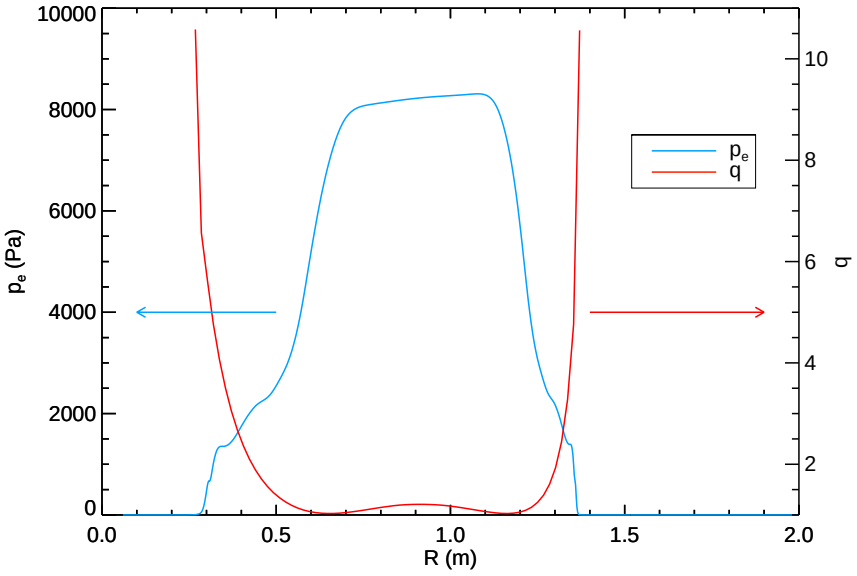

FIGURE 6.3: Fitted p_e and q profiles from motional stark effect and Thomson scattering constrained EFIT++ equilibrium reconstruction. Taken at 0.3s in discharge 23447.

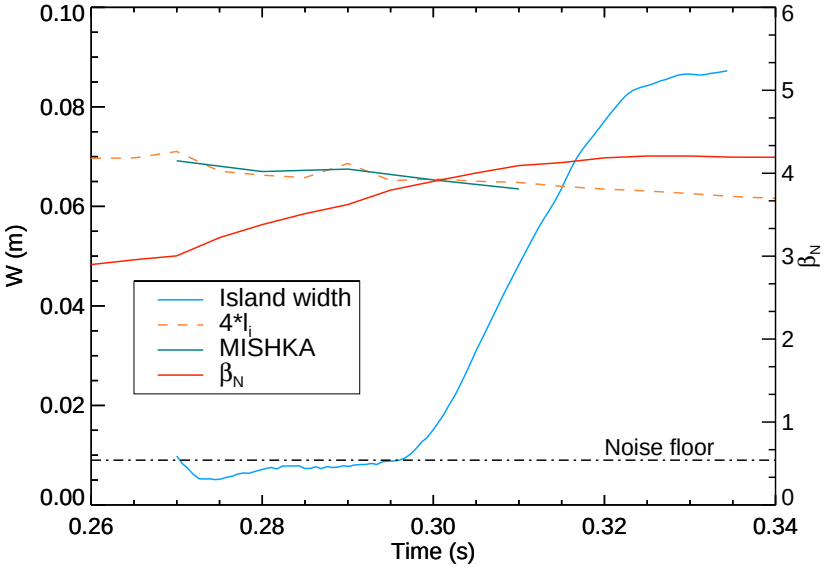

FIGURE 6.4: Evolution of 2/1 NTM width for discharge 23447. NTM onset coincides with β_N reaching the ideal no wall limit, calculated using MISHKA. The large aspect ratio estimation of the limit, $4l_i$ (where l_i is the plasma internal inductance), is also close to this result.

(and disruption at 0.345s), for discharge 23447. β_N increases and reaches the no wall, ideal limit calculated using ideal MHD stability code, MISHKA [80]. This matches surprisingly well with the large aspect ratio estimate for the limit, $4l_i$ (where l_i is $l_i(3)$, the plasma internal inductance obtained from EFIT). In all the discharges considered, the onset of the NTM coincides closely with reaching this β_N limit and obvious seed island triggers are often lacking. The onset characteristics of these 'triggerless' NTMs are consistent with those reported in similar scenarios on the DIII-D tokamak [61]. The origin of this triggerless destabilisation is investigated in section 6.6.

6.5 The MRE expressed in terms of basic tokamak plasma parameters

The terms in equation 6.1 can either be calculated using a variety of stability codes [72] or, assuming an idealised geometry, written down analytically in terms of measurable parameters [59, 63]. In this chapter the latter option is chosen, with the aim of attributing meaningful errors to the input parameters, which can be propagated through the full analysis. Equation 6.1 is rewritten as the following semi-heuristic model, based on those used in Buttery et al. (2002) [41] Sauter et al. (2002) [63] and Urso et al. (2005) [59]:

$$\begin{aligned}\frac{1.9\times10^4\mu_0 r_s T_{eV}^{\frac{3}{2}}}{\ln\Lambda}\frac{dW}{dt} &= r_s\Delta' - a_{nl}W \\ &+a_1 r_s\beta_p L_q\sqrt{\frac{r_s}{R_0}}\frac{1.4}{L_p}\frac{W}{W^2+W_d^2} \\ +a_2 r_s\beta_p\left(q^2-1\right)\frac{r_s L_q^2}{qR_0^2L_p}&\frac{1}{\sqrt{W^2+0.65W_d^2}} \\ -a_3 r_s\beta_p\frac{2mT_{eV}}{eB_\theta^2}\left(\frac{L_q}{L_p}\right)^2 g(\varepsilon,\nu_i,\omega)&\frac{W}{W^4+W_b^4}\end{aligned} \tag{6.11}$$

Here $W_d = 5.1w_c$; a relation that was mentioned in Chapter 3 and is obtained by matching of small and large island limits [1]. This is approximately the W for which $\frac{dW}{dt}$ is a maximum and is therefore considered to be the marginal value of W at marginal β_p. W is the magnetic island width, calculated using the method described in section 6.3. W_b is the ion banana width. L_q and L_p are the gradient length scales for the safety factor, q and the pressure, p, defined as $q(dq/dr)^{-1}$ and $p(dp/dr)^{-1}$. β_p is the local

poloidal β defined as $2\mu_0 p/\langle B_\theta \rangle$, where $\langle B_\theta \rangle$ is the flux surface averaged poloidal field. T_{eV} is the electron temperature in eV, which is found to be approximately equal to the ion temperature in the vicinity of the rational surface. The term $g(\varepsilon, \nu_i, \omega)$, where ε is the inverse aspect ratio, ν_i is the ion collisionality and ω is the island rotation frequency in the plasma frame, describes the magnitude of the polarisation current and is discussed in more detail later in this section. All parameters except W and β_p are measured at the time of NTM onset and assumed to stay constant during the period of interest. This approach has been used in previous studies [63] and in most cases there are only small changes in profiles during island evolution. The coefficients Δ', a_{nl}, a_1, a_2 and a_3 are also assumed to remain constant in time.

Following Urso et al. (2005) [59], the analytic large aspect ratio formulae for bootstrap current, j_{bs}, and resistive interchange parameter, D_R, are used in order to write them in terms of the measurable parameters mentioned above. This method not only has the advantage of facilitating error propagation but also allows the correlation that exists between some of the terms in equation 6.11, due to their dependence on these measureable parameters, to be captured in the analysis. Values of j_{bs} and D_R have also been obtained using the NCLASS [81] and CHEASE [52] codes respectively. Full propagation of experimental errors through these codes is non-trivial and beyond the scope of this thesis. All calculations of j_{bs} and D_R are very sensitive to the quality of the equilibrium reconstruction and the method chosen for calculating L_p (or L_n, L_{T_e} and L_{T_i}) from the TS data, which requires a smoothing or fitting procedure to avoid mistaking fluctuations for equilibrium gradients. Consequently, uncertainties on j_{bs} and D_R are large, whichever method is used. For the analytic method the uncertainties are estimated to be $\sigma_{j_{bs}} \sim 20\%$ and $\sigma_{D_R} \sim 30\%$ and are expected to be similar when using NCLASS and CHEASE, though calculating errors for this method is not simple. The NCLASS and CHEASE values calculated here typically differ from those calculated using the analytic formulae by less than a factor of two, depending on the equilibrium reconstruction used. Recent calculations of D_R for NSTX, using the NIMROD code, have also shown only a small difference of about 15% compared to an analytic, large aspect ratio calculation [82]. It should be emphasised that the limitations of using these analytic approximations are well understood but that this approach is taken in order to preserve the effects of the parameter correlations described above. Any necessary correction of j_{bs} and D_R due to plasma shaping should be captured in a_1 and a_2 during the fitting procedure described below.

Another term which cannot be determined simply from measurements is $g(\varepsilon, \nu_i, \omega)$, a function associated with the polarisation current. In order to evaluate this term, it is necessary to make a transform to the rotating frame in which the radial electric field, E_r, is zero at the rational surface [56]. This is done experimentally using the charge exchange recombination spectroscopy diagnostic (CXRS), described in Chapter 2, which gives measurements of the ion flow and temperature. From this, the rotation frequency of the $E_r = 0$ frame, $\omega_{E_r=0}$, can be estimated. Then the island rotation frequency, ω_{Mirnov}, is Doppler shifted from the lab frame to the $E_r = 0$ frame. The term is expected to provide a similar contribution to the MRE in all the discharges considered here, due to the islands being born at a similar frequency lower than $\omega_{E_r=0}$ and in the opposite direction (in the lab frame) in all cases. However, it is not possible to make a quantitative statement about $g(\varepsilon, \nu_i, \omega)$ for these discharges as current available models do not include sufficient physics. In the absence of a complete theory, the unknown contribution is absorbed into dimensionless fitting parameter, a_3. As was mentioned in Chapter 3, polarisation current theory is only developed for $W > W_b$, the banana width. In order to take account of this, the functional form $\Delta_{pol} \propto W/(W^4 + W_b^4)$ was adopted as a heuristic model [53].

The coefficients associated with each of the five terms: Δ', a_{nl}, a_1, a_2 and a_3, are now considered. Δ' is notoriously difficult to calculate [83] and requires extremely accurate equilibrium reconstruction before it can be derived. Even with an accurate equilibrium reconstruction, sensitivity to small changes in the current and pressure profiles make uncertainties very high. a_{nl} can be calculated but is a function of the first and second radial derivatives of the equilibrium current density [58], which have large errors experimentally. a_1 and a_2 can be estimated for a given equilibrium and have values ~ -3 and ~ 6 respectively [41]. a_3 is an order 1 constant which can be calculated numerically, again with large uncertainty. Given the theoretical uncertainties, the five coefficients are estimated by using them as free parameters in a fit of equation 6.11 (integrated w.r.t time) to the experimentally measured W. The fitting method is described below, in section 6.5.1.

6.5.1 Probabilistic approach to fitting

The version of the MRE presented in section 6.5 is written in terms of a series of basic plasma parameters, all of which are either directly measurable or relatively well

constrained parameters in the EFIT++ equilibrium reconstruction. The measured parameters and their estimated uncertainties are written down in table 6.1. The errors on parameters derived from Thomson scattering data, such as kinetic profiles and the rational surface position, are charaterised by the typical size of T_e and n_e fluctuations [84] and the radial resolution of the diagnostic. Errors on parameters taken from EFIT are harder to estimate as they rely on a number of separate measurements but the values chosen here are thought to be reasonable for such a well constrained solution to the Grad-Shafranov equation.

Parameter	Uncertainty
W	10% + 0.5cm
β_p	10%
W_d	30%
R	1cm
r_s	1cm
$\ln\Lambda$	$\pm$0.5
T_{eV}	5%
L_p	10%
L_q	10%
B_θ	5%

TABLE 6.1: Measurable parameters from the MRE and their uncertainties.

The approach taken is similar to that in Urso et al. (2010) [85] and in Chapter 4. Each of the measurable parameters from table 6.1 are assumed to be described by a Gaussian probability density function (PDF) with a mean and σ given by the experimentally measured value and its experimental uncertainty. Values are then randomly sampled from these PDFs and fed into equation 6.11 before integrating and fitting it to the experimentally observed W. This process is then repeated 1000 times to build up histograms of the free parameters (the five coefficients), the mean and σ of which are the best estimate and uncertainty of the parameter.

For the observed value of W, a significant part of the estimated uncertainty comes from the 10% error on the calibration factor calculated in section 6.3. This is propagated through the MRE using a single multiplication factor for the whole time series, randomly sampled from a Gaussian distribution with a mean of 1 and σ=10%. In addition, a Gaussian error component of 0.5cm, estimated from the background noise floor, is included to account for the noise in the Mirnov signal from magnetic fluctuations.

Following the same procedure used for the constraint on w in Chapter 4, constraints on the free parameters, based on their theoretically predicted values, are included in the

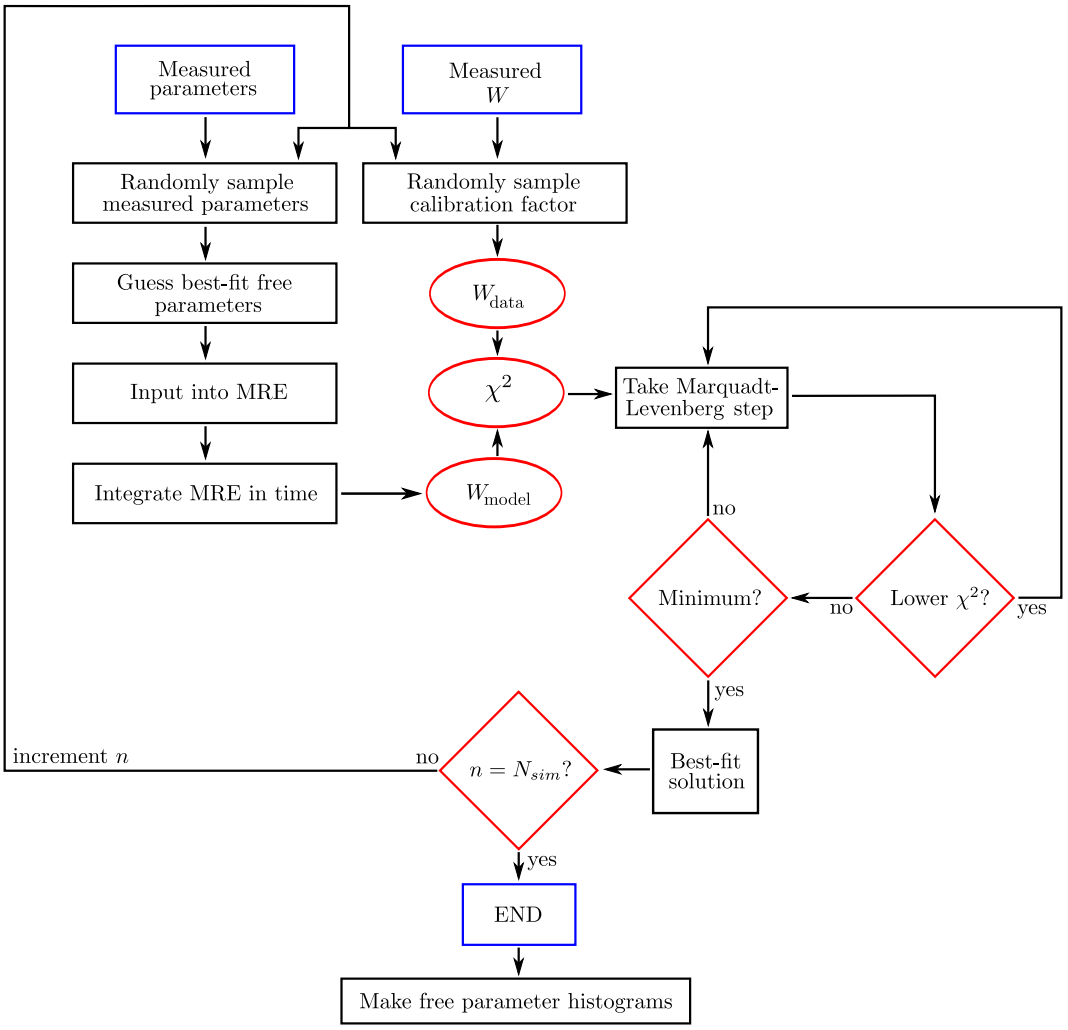

FIGURE 6.5: Flow chart for MRE fitting procedure.

fit to ensure that their sign and order of magnitude is physically plausible. For the a_1 and a_2 parameters, whose values are fairly well characterised by theory, the constraints are fairly stringent with $\sigma = 20\%$. The other parameters have much looser restrictions at $\sigma = 200\%$.

This method provides an experimental estimate of the relative contributions of the five terms and also experimental errors not easily derived from the usual calculation methods. Note that the mean evolution of W obtained through this method may not necessarily give the closest fit to the data, but it is the most probable given the experimental uncertainty and the prior theoretical information about the fit parameters. The fitting procedure is summarised in the flow chart in figure 6.5.

6.6 Results for fitting to NTM onset up to saturation

The majority of MAST discharges with NTMs result in disruption when the associated magnetic island grows large and locks to the wall. Section 6.6.1, below, outlines the results from the fitting of the MRE to the observed NTM evolution in one of these discharges.

6.6.1 Discharge 23447

Discharge 23447 was presented in section 6.4 as an example in which the ideal β_N limit is reached and a 'triggerless' NTM is destabilised. Figure 6.6 shows that this is a high power discharge with around 3MW of injected NBI power and a maximum β_N of over 4. The discharge is particularly quiescent, entering a 0.07s period of ELM free H-mode at about 0.27s. The β_N increases continuously due to the high level of heating and fueling throughout the discharge, as well as the good confinement and lack of energy-dissipating ELMs during the H-mode period. An NTM starts to grow from a very low size at around 0.29s, saturates at about 0.32s, locks to the wall at 0.34s and terminates the plasma at 0.35s. The wall-locking is seen as a drop in the amplitude of the Mirnov signal as the rotation slows, giving a reduced dB/dt.

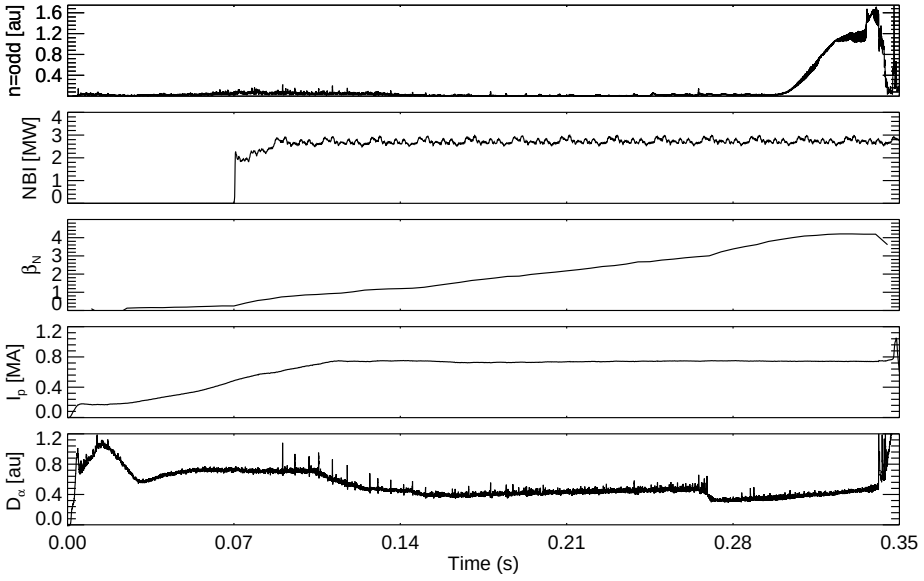

FIGURE 6.6: Time traces for discharge 23447. From top to bottom: 1. n=odd Mirnov coil amplitude. 2. Summed power from MAST's two neutral beams. 3. β_N, the normalised β of the plasma. 4. I_p, the plasma current. 5. Line integrated D_α emission.

This discharge provides 0.05s of NTM evolution at a range of magnetic island widths, which can be studied using the MRE. One advantage of using this discharge is the relatively smooth evolution of the NTM in the quiescent ELM free H-mode period. As section 6.7.2 will show, other instabilities can often interrupt or modify NTM evolution, which can make fitting a challenge. For example, a sudden transient event, such as a large ELM, can often reduce the plasma rotation in the vicinity of the magnetic island, resulting in a reduction in the measured Mirnov amplitude. However, this can be very difficult to decouple from any simultaneous change in the magnetic island width due to the perturbation and the signal due to the ejected ELM filament. Therefore, it is advantageous to study such quiescent discharges so as to minimise these external effects, which are not easily included in the MRE.

6.6.1.1 Best fit solution

Figure 6.7 shows the coefficient distributions for discharge 23447. They are approximately Gaussian and their mean and σ give the best-estimate and uncertainty for the five parameters: $\Delta' = 1.6 \pm 0.8$, $a_{nl} = 26 \pm 9$, $a_1 = -3.6 \pm 0.8$, $a_2 = 7.1 \pm 0.6$, $a_3 = 1.0 \pm 1.2$. Figure 6.8 shows the best-fit solution compared to the experimental data.

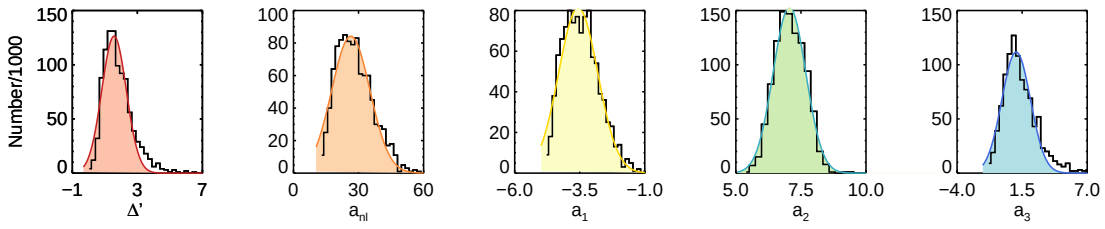

FIGURE 6.7: Distributions of the five coefficients for discharge 23447, found to be approximately Gaussian. The mean of each distribution is taken to be the best-estimate given the errors on the measured data.

It is of interest to look at the overall contributions from the five terms in equation 3.30 as they evolve in time (figure 6.9). Both a strongly destabilising Δ_{bs}, due to steep pressure gradients, and a positive Δ' are required for NTM growth from such a small starting size. As expected in a spherical tokamak, the Δ_{GGJ} term is significantly stabilising and a_2 is somewhat larger than the theoretically predicted value (7.1 rather than 6.5), suggesting that a small aspect ratio correction to the resistive interchange parameter, D_R, has been absorbed into this coefficient. Also, with a positive Δ', it is important to include the stabilising non-linear term, in order to account for the saturation of the

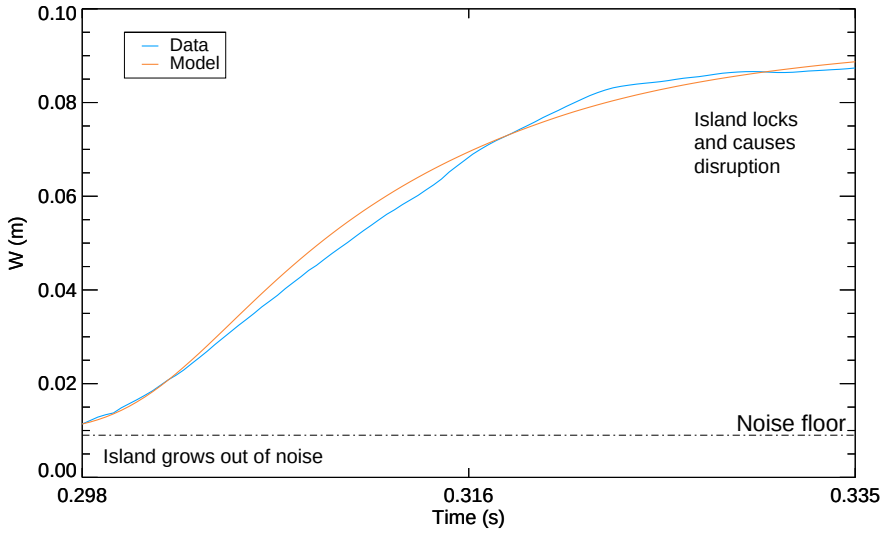

FIGURE 6.8: Measured W from Mirnov coil data and model W, during island onset and growth, using mean values from parameter distributions for discharge 23447.

island. The $a_3\Delta_{pol}$ term appears to play a small stabilising role when the island is small, although errors are significant due to the $1/W^3$ dependence.

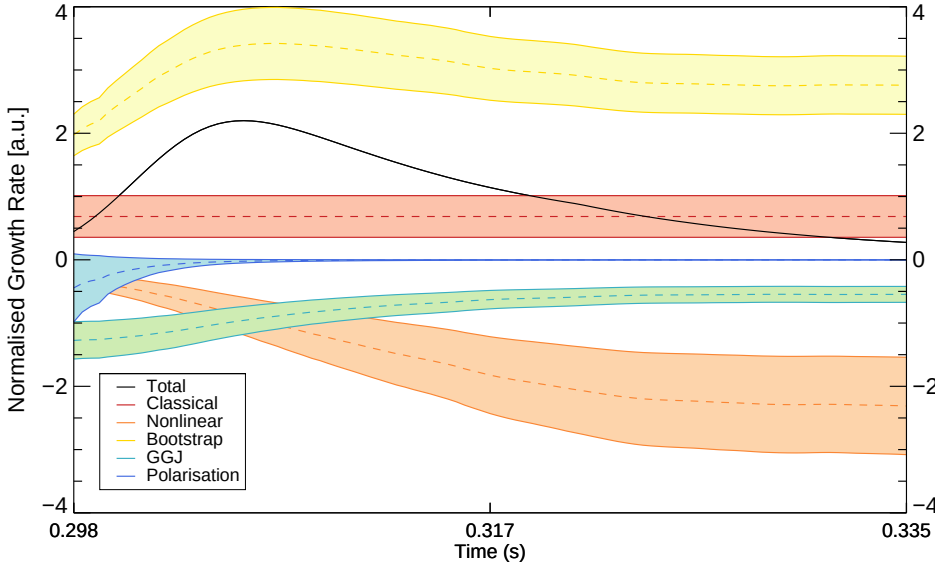

FIGURE 6.9: Time evolution of individual contributions to the modified Rutherford equation for discharge 23447.

The requirement for a positive Δ' is in-line with the theory that, close to the ideal β_N limit, a 'pole' in Δ' is approached [48, 60]. Note that approaching a pole is unlikely to result in a very large, positive Δ' because an NTM will be driven unstable as soon as Δ' becomes sufficiently positive, i.e. $\Delta' \sim 1.6$. Also, it is unlikely that the NTM is really 'triggerless', but that the destabilising contribution of Δ' causes the required seed

island size to be smaller than the noise floor, in which case small magnetic fluctuations may be creating seed islands above the threshold.

Reimerdes [53] has shown that classically unstable tearing modes, which later become neoclassically unstable, show two phases of distinctly different evolution, with an increase in growth rate as the mode becomes neoclassical. In 23447, the NTM is both classically and neoclassically unstable at onset, but the two contributions are comparable. Two distinct phases are not present, but there is a clear increase in growth rate as the neoclassical drive takes over, shortly after onset.

6.6.1.2 Contours of χ^2_{red}

As in Chapter 4, it is instructive to look at the χ^2_{red} contours for an individual fit in order to examine the relationships between pairs of parameters. Figure 6.10 shows a series of 2D cross sections of χ^2_{red} in the 5D parameter space.

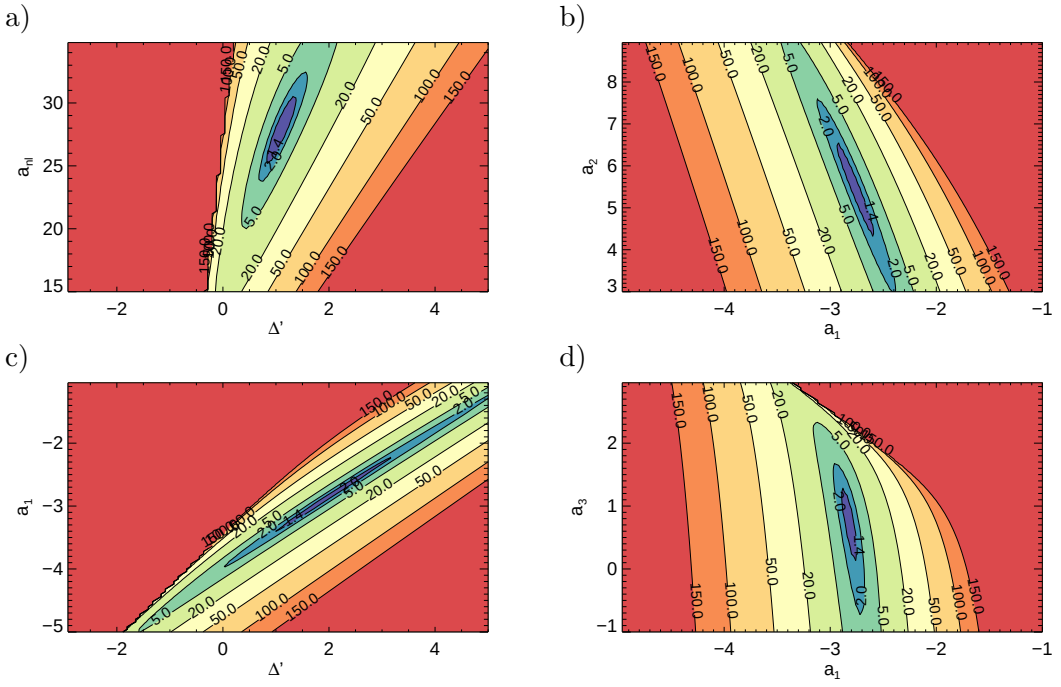

FIGURE 6.10: Contours of χ^2_{red} for discharge 23447. **a)** Δ' and a_{nl}. **b)** a_1 and a_2. **c)** Δ' and a_1. **d)** a_1 and a_3. All parameters are dimensionless except Δ', which has units of m^{-1}.

The minimum value is close to $\chi^2_{red} = 1$ but this test is perhaps not appropriate for this type of data as the majority of the error comes from the overall multiplication factor used to calculate W, rather than noise on the signal. Still, it is a useful indication of quality of fit and is therefore used as a guide. The angled minima demonstrate that there are correlations between most of the parameters, due to numerous shared dependences

on the measured parameters. For example, a_1 and a_2 are anti-correlated because Δ_{bs} and Δ_{GGJ} share similar β_p, L_p and W dependences but with opposite signs. One interesting feature of several of the plots is the visibility of the NTM threshold. This can be seen clearly as a very steep gradient in χ^2_{red} in the bottom left corners of figures 6.10a and c and the top right corner of figure d. When the model is in a parameter regime below the threshold, the island shrinks away, leading to a very large χ^2_{red} due to the large difference between the observed W and the model W. In these three plots, the minima appear to be very close to the threshold in parameter space. This is in agreement with the hypothesis, presented in section 6.6.1.1, that as the ideal limit is approached Δ' becomes more positive and the threshold is crossed just as the balance of terms for a very small seed island becomes net-destabilising.

6.7 Results for NTM β ramp-down experiments

NTM stability can be investigated further by studying the β dependence of equation 6.11. This has previously been investigated on various tokamaks, notably for 3/2 NTMs on MAST [41] and 3/2 and 2/1 NTMs on JET [63]. As was explained in Chapter 2, there is a particular difficulty in ramping down β for spherical tokamak plasmas containing 2/1 NTMs as the $q = 2$ surface tends to be close to the plasma edge and all external heating and torque sources are supplied by the NBI system. Furthermore, stepping the NBI power input down gradually is not currently possible on MAST and even if it were, it would be very difficult to make this gradual power reduction quick enough to remove the NTM before the end of the shot. The loss of torque input also means that removing the NBI power is very likely to result in the mode locking and plasma disruption before β can drop significantly. However, scenario development has enabled an operational window in which successful β ramp-downs have been achieved, providing NTM stabilisation and disappearance without mode locking. Two examples of β ramp-downs are presented in sections 6.7.1 and 6.7.2.

6.7.1 Discharge 24082

The time traces for discharge 24082 are shown in figure 6.11. The main characteristics are similar to 23447, with similar profiles and a β_N reaching $4l_i$, leading to NTM growth. One difference is the H-L back-transition, which can be seen on the line integrated D_α emission trace of figure 6.11 at about 0.26s. This event does interrupt the Mirnov signal

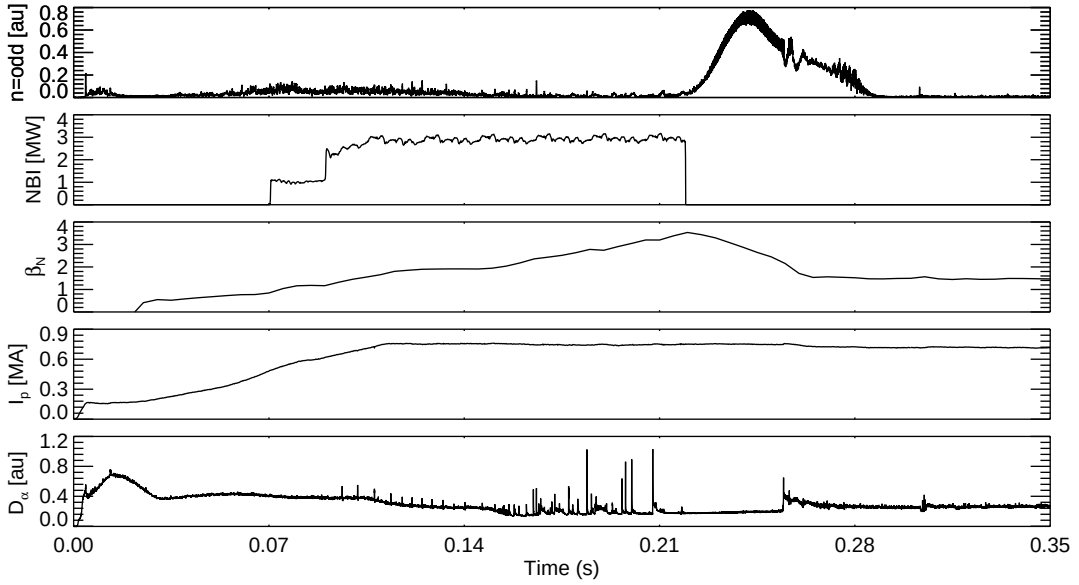

FIGURE 6.11: Time traces for β ramp-down discharge 24082. From top to bottom: 1. n=odd Mirnov coil amplitude. 2. Summed power from MAST's two neutral beams. 3. β_N, the normalised β of the plasma. 4. I_p, the plasma current. 5. Line integrated D_α emission. β ramp-down analysis carried out between 0.22s and 0.28s.

as plasma filaments are lost from the edge but it is not clear whether the magnetic island itself is affected. It does not appear to affect the fitting procedure significantly. Fits in previous studies [41, 63] have included an H-L transition without problem.

One change to the model is required for a decreasing β. In the previous section, it was assumed that Δ' stays constant between NTM onset and saturation and, as β usually remains roughly constant during this period, this is a reasonable assumption. However, as β is reduced below the ideal limit, Δ' is expected to move away from its initially destabilising value. It is probable that, at lower β and smaller saturated island size, the two terms making up the classical tearing part of equation 6.1 will return to a stabilising constant $\sim -2m$ [59]. Equation 6.12 shows the functional form used to describe the evolution of the classical tearing terms. This form captures the essential behaviour and is a matching of two limits rather than a derived expression.

$$\begin{aligned} \Delta_{classical} &= r_s\Delta' - a_{nl}W \qquad & r_s\Delta' - a_{nl}W &\leq -2m \\ \Delta_{classical} &= -2m \qquad & r_s\Delta' - a_{nl}W &> -2m \end{aligned} \tag{6.12}$$

The 2/1 NTM evolution for discharge 24082 is shown in figure 6.12. Also shown are

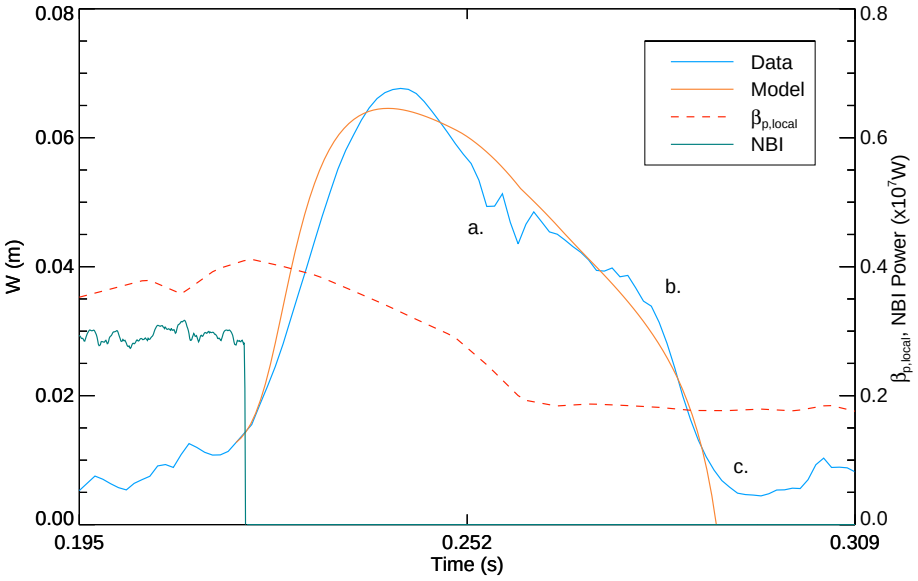

FIGURE 6.12: NTM evolution for β ramp-down discharge, 24082. **a.** H-L transition. **b.** Stabilisation, with change in growth rate due to transport threshold. **c.** Island width drops below noise level and is assumed to be stabilised.

the injected NBI power, removed at 0.22s, and the local β_p (at the $q = 2$ surface), which begins to drop thereafter. The island width, W, drops steadily with β until about 0.28s when the decay rate suddenly increases. Figure 6.12 also shows the best-fit solution, which is found to be a good match to the data.

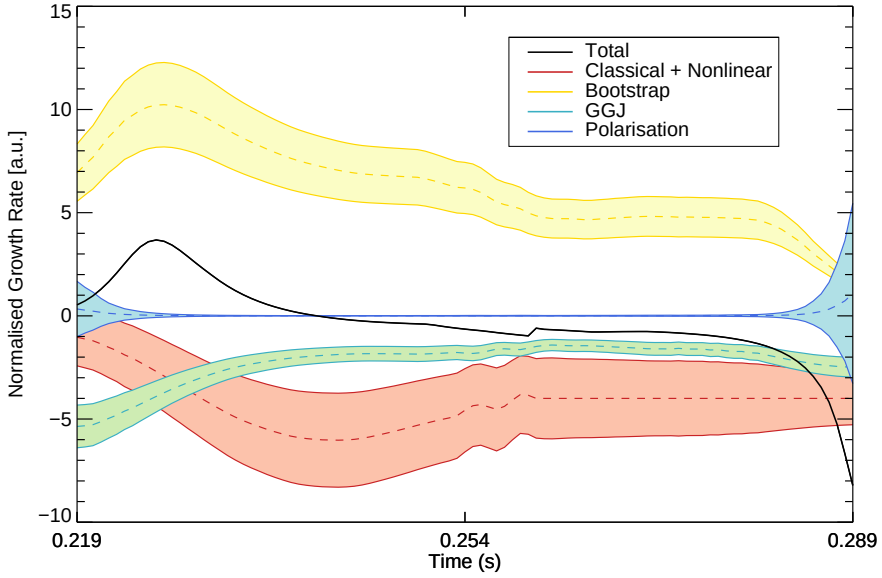

FIGURE 6.13: Time evolution of individual contributions to the modified Rutherford equation for discharge 24082, indicating the role of the reduction in bootstrap drive as the island width approaches the measured transport threshold.

The five contributions as a function of time are shown in figure 6.13. The best fit

values are $\Delta' = 0.4 \pm 0.7$, $a_{nl} = 83 \pm 16$, $a_1 = -3.4 \pm 0.6$, $a_2 = 6.8 \pm 1.0$, $a_3 = -0.05 \pm 1.5$. It is found that $\Delta' \sim 0$, initially, and that the $a_1 \Delta_{bs}$ term is the most significant destabilising term. The main conclusion of this analysis is that the island stabilisation at 0.28s is found to be close to the marginal point predicted by the transport threshold, when W reaches a value close to $W_d = 5.1 w_c = 3.6$cm, obtained from experimental T_e profiles in Chapter 4. The contribution from the polarisation current is found to be small and only plays a role later, when the island is smaller than W_d but, again, the uncertainties are significant.

6.7.2 Discharge 28124

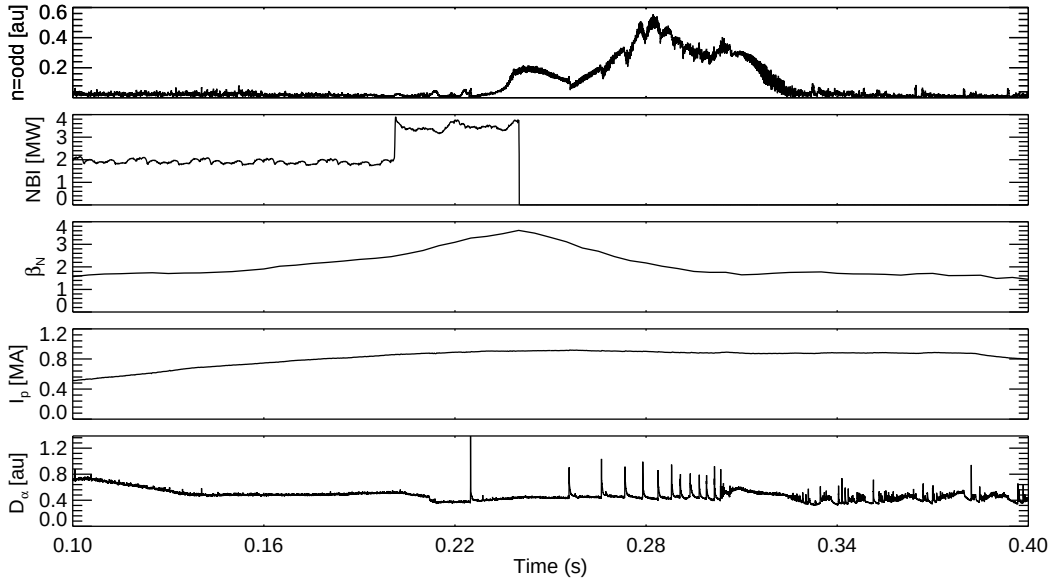

FIGURE 6.14: Time traces for β ramp-down discharge 28124. From top to bottom: 1. n=odd Mirnov coil amplitude. 2. Summed power from MAST's two neutral beams. 3. β_N. 4. I_p, the plasma current. 5. Line integrated D_α emission. β ramp-down analysis carried out between 0.225s and 0.33s.

The time traces for discharge 28124 are shown in figure 6.14. Again, it has similar characteristics to 23447 and 24082, with similar profiles and a β_N reaching $4l_i$, leading to NTM growth.

One significant difference is the presence of higher mode number NTMs, on different rational surfaces, in the early stages of the evolution of the 2/1 NTM. This is shown in the toroidal mode number analysis in figure 6.15 performed using an array of toroidal separated Mirnov coils. An EFIT reconstruction shows that the 3/2 and 4/3 surfaces are approximately 7cm and 10cm away from the q=2 surface. Previous work [63] has shown

that a 3/2 or 4/3 mode can non-resonantly couple to a 2/1 mode, providing a stabilising contribution to the MRE. In Sauter et al. (2002) [63] this was semi-heuristically modelled as an additional term: $-r_s\Delta_{3/2}$ or $-r_s\Delta_{4/3}$.

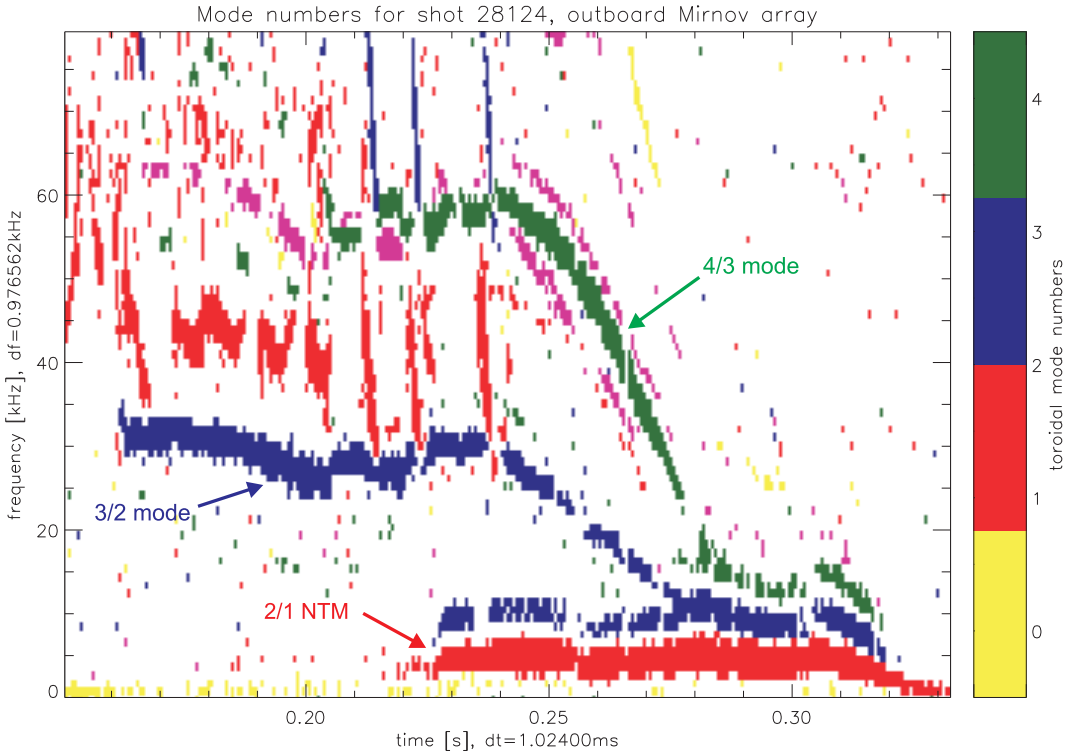

FIGURE 6.15: Toroidal mode number analysis for discharge 28124. The analysis reveals simultaneous 3/2 and 4/3 NTMs growing and decaying away as a 2/1 NTM grows.

This effect is further complicated by interaction with ELMs. The first ELM to have an effect on the 2/1 NTM occurs at 0.26s, just as the 3/2 and 4/3 modes are disappearing. This ELM perturbs the 2/1 NTM, which then starts a new phase of growth. The 2/1 NTM is able to grow to a larger saturated width than previously as it is now free from the stabilising effects of the non-resonant mode coupling, which is considered to disappear with the 3/2 and 4/3 modes at 0.26s. As with section 6.7.1, a heuristic model was devised in order to extract the general behaviour of the 2/1 NTM, without properly considering its interactions with other modes. A realistic model for this system of interacting instabilities would require much more detail, such as the inclusion of stochastic field lines due to overlapping magnetic islands, for which the MRE is not well-suited.

The simple approach used here is to split the evolution of W into two time regions, one before the first ELM ($t = 0.225\text{s}-0.26\text{s}$) in which the 3/2 and 4/3 modes are present, and one after the ELM ($t = 0.26\text{s}-0.33\text{s}$) when the modes are not. By fitting the MRE

to these two regions separately, the magnitude of the effect of the 3/2 and 4/3 modes can be extracted without having to implement a complicated model.

The best fit parameters for the first time region are: $\Delta' = 10.1 \pm 2.5$, $a_{nl} = 550 \pm 16$, $a_1 = -4.8 \pm 1.7$, $a_2 = 5.81 \pm 2.2$, $a_3 = 0.0 \pm 1.3$. For the second time region, they are: $\Delta' = -0.5 \pm 1.2$, $a_{nl} = 112 \pm 10$, $a_1 = -3.3 \pm 0.9$, $a_2 = 6.8 \pm 0.8$, $a_3 = 0.8 \pm 1.2$. Figure 6.16 shows the best-fit solution compared to the experimental data.

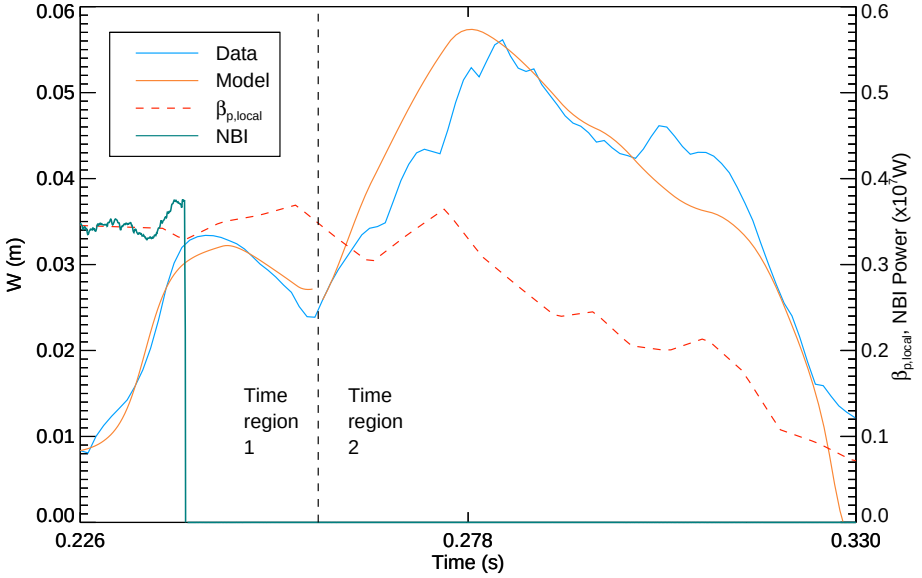

FIGURE 6.16: NTM evolution for β ramp-down discharge, 28124. In *time region 1*, a 3/2 and a 4/3 are NTM present. In *time region 2*, the 3/2 and 4/3 NTMs have disappeared.

The best fit values of Δ' and a_{nl} in the first time region are questionable, but this was to be expected as the combined physics of the ideal β_N limit and the non-resonant mode coupling is absorbed into these terms. The high value of Δ' is required to destabilise the 2/1 NTM from small W. Though probably an overestimate, this result is consistent with the hypothesis that the approach to the ideal β_N limit gives rise to a positive Δ'. The large value of a_{nl} is required to both compensate for the large Δ' and to take account of the additional stabilisation due to the 3/2 and 4/3 modes. In Sauter et al. (2002) [63], it is found that Δ' is negative and that the bootstrap current drive is the main destabilising term. Furthermore, the other modes do not appear until the 2/1 NTM is already at its saturated W. For Sauter, the addition of a simple stabilising $-r_s\Delta_{3/2}$ or $-r_s\Delta_{4/3}$ term does not prevent the 2/1 NTM from growing. However, for the MAST discharge considered here, where a positive Δ' is required to provide the initial destabilisation for the 2/1 NTM, this simple stabilising contribution has to be absorbed into a_{nl}, which only takes effect after the 2/1 NTM has started growing and does not inhibit the initial

growth of the small island. The best-fit values of a_1, a_2 and a_3 in the first time region are all similar to those obtained in the previous two discharges.

All of the best fit parameters in the second time region are closer to those in the previous two discharges. The fact that all parameters return to reasonable values as soon as the 3/2 and 4/3 NTMs disappear validates that hypothesis that it is their presence that causes the unusual best-fit values of Δ' and a_{nl} in the first time region. The negative Δ' term is as expected because the β_N has dropped well below the ideal limit by 0.26s. Also, the threshold island stabilisation as the β_p drops below its marginal value is well matched by the model, which, as before makes use of the w_c obtained in Chapter 4.

6.8 Summary

The modified Rutherford equation (MRE) is a well-established model for NTM evolution that has been used in numerous studies to investigate NTM stability, but the analysis presented above has several key differences. One advantage is that the value of w_c, which contributes to the Δ_{bs} and Δ_{GGJ} terms, has been experimentally evaluated using the technique described in Chapter 4, so that no specific models for parallel or perpendicular heat transport are assumed. This has not been the case in many previous analyses of NTM growth. Estimation of the coefficients of the MRE was undertaken using a probabilistic approach which provides estimates of the uncertainties on the parameters, which have usually been neglected in previous studies.

In a series of MAST discharges, all approaching the ideal, no wall β limit, it was found that Δ' was marginally destabilising, the non-linear classical evolution term was stabilising, the bootstrap current term was strongly destabilising and the curvature term was stabilising. The contribution from the polarisation current term was found to be small for these discharges with large uncertainties, and it is not currently possible to make general statements about the significance of this term without a more complete physics model. The fitted parameters are summarised in table 6.2:

The fitted values are generally consistent with the theoretical values, although Δ' was found to be positive, as discussed above. The parameter a_{nl} demonstrates considerable variation between discharges, although its order of magnitude is consistent with the theoretical value. This may be explained by the fact that the parameter is sensitive to small changes in the current profile especially in discharge 28124, which has a lot of

Discharge	Δ'	a_{nl}	a_1	a_2	a_3
23447	1.6	26	-3.6	7.1	1
24082	0.3	86	-3.6	6.7	-0.1
28124	-0.5	112	-3.3	6.8	0.8
Theoretical values [43, 59]	-2	~ 50	-3–-4.6	6.35	$\sim$1

TABLE 6.2: Fitted values of MRE coefficients compared against theoretical values. Note that the theoretical Δ' is stabilising but as was stated previously this parameter can become destabilising.

MHD activity affecting the current profile. It is worth noting that a_2 is consistently higher than the theoretical prediction in these fits, which may be due to the plasma shaping effects of the spherical tokamak not properly included in the simple version of the MRE used here.

The probabilistic approach outlined here indicates that errors on measurements of the polarisation current term are significant, mainly due to the $1/W^3$ dependence. A careful treatment of small island measurements, with good statistics, will be required if this is to be overcome in future. Data from two β ramp-down experiments was also analysed. A simple model was used to account for the effect of non-resonant coupling with other instabilities on the evolution of the 2/1 NTM, which did not reveal anything about the nature of the interaction itself but did facilitate an analysis of the balance of terms in the MRE. In both cases, the transport threshold for the bootstrap current drive was found to explain the increase in decay rate at $W \sim W_d$.

Chapter 7

Conclusions

Though neoclassical tearing modes (NTMs) can be controlled, they remain one of the major concerns to the future of fusion as a commercially viable energy source. The most effective mitigation systems available have significant power requirements that are predicted to reduce the efficiency by over 20% while in use on ITER [22]. For this reason it is important to attempt to better understand the causes of NTM destabilisation, both through theoretical models and experimental measurements on existing tokamaks. NTMs typically require a seed magnetic island, above a certain threshold width, before they become unstable and therefore much of the theoretical work of the past 20 years has focused on the behaviour of small magnetic islands. As a result, a number of different but correlated models are thought to influence this behaviour and are often combined together in a single equation, known as the modified Rutherford equation (MRE), in order to study their net effect. This thesis has investigated the limits of the experimentalist's ability to resolve the structure and evolution of small magnetic islands with current MAST diagnostics and to distinguish between the effects of different models, given the uncertainties on experimental measurements. Section 7.1 presents a summary of each of the chapters and their findings. A key theme of this thesis has been that if there are correlations between model parameters, additional independent measurements or theoretical constraints can be used to reduce uncertainties and build a more complete picture of the system under observation. This is reflected in section 7.2, which outlines a number of ideas for future work, including the potential implementation of an integrated approach to the study of NTMs that would use a number of diagnostics simultaneously to constrain key parameters of interest, such as Δ' and w_c.

7.1 Summary

NTMs are not isolated phenomena and are influenced by the conditions throughout the tokamak, such as the amount of external heating, the global confinement, the presence of other instabilities and the proximity to the conducting wall of the tokamak vessel. Therefore, Chapter 1 described the features of the tokamak, with a focus on those attributes that impact NTM behaviour. This included an explanation of resonant surfaces and their susceptibility to plasma instabilities, the origins and pressure dependence of the bootstrap current and an overview of high β and high confinement tokamak regimes.

The analysis methods presented in this thesis are generally applicable to the study of NTMs on most tokamaks but here they were applied to the MAST spherical tokamak. Chapter 2 described the diagnostic tools used to measure the plasma parameters that affect NTM stability and the experiment design process that was conducted in order to find a suitable regime for studying NTMs on MAST. In order to help find this regime, a database of MAST discharges was created, in which the dependence of the NTM magnetic island width on a range of different parameters was considered. In particular, it was necessary to find a scenario in which an NTM β ramp-down could be studied. This required rapid but controlled energy input followed by a similarly rapid but controlled reduction in the stored energy, which proved to be a challenging scenario to find. This process was further complicated by interactions with the vessel wall and other instabilities but an operational window was found, which enabled the collection of useful β ramp-down data.

Chapter 3 introduced the various theories that govern NTM evolution. The key parameters and coordinate systems used to study magnetic islands were presented and previous experimental observations of NTMs in various tokamaks were summarised. Each of the contributions that make up the MRE were described in turn but particular attention was paid to the bootstrap current drive and the associated transport model, thought to give rise to a threshold for NTM growth. The critical width for island temperature flattening, w_c, which has been used throughout this thesis, was introduced as a key parameter in this transport threshold model. Finally, all the contributions were combined in a version of the MRE, which was used again in more detail in Chapter 6.

The transport threshold model was revisited more thoroughly in Chapters 4 and 5. The aim here was to generate temperature profiles using Fitzpatrick's heat transport model for a magnetic island and fit them to MAST Thomson scattering T_e profiles in

order to infer the size of w_c [1]. In Chapter 4, the heat transport equation was modified to take account of the radially asymmetric islands observed on MAST. To avoid over-complicating the model, a simple quasi-linear correction to the perturbed flux was used, parameterised by a single variable, A. The equation was solved numerically using a finite difference scheme with appropriate boundary conditions. The solutions are 2D profiles of the magnetic island temperature perturbation, with characteristic geometry described by a set of six parameters, including the island half width, w, the critical width, w_c, and the asymmetry parameter, A.

In Chapter 5, these free parameters were used to fit the model temperature profiles to data. Initially, the fitting procedure was tested by fitting to synthetic data, generated by adding randomly sampled Gaussian noise to the transport model solutions. By repeatedly generating data using different random noise each time, histograms of the best fit parameters were produced, which were found to be approximately Gaussian. The mean of the Gaussian gave an indication of the accuracy of the fitting method and the standard deviation was an estimate of the experimental uncertainty. This process was repeated for a variety of experimental arrangements and the variation of the parameter uncertainties under different conditions was characterised. It was found that w_c could be inferred with reasonable levels of certainty in most realistic experimental arrangements but that there were optimum conditions under which the uncertainty was minimised. It was also found that w_c is correlated with w and that an independent measurement of w can help to constrain w_c. Following this, the model temperated profiles were fitted to real data from the MAST Thomson scattering system for a series of 13 similar discharges. By combining the estimates of w_c from each of the discharges, a best estimate of $w_c = 0.7 \pm 0.2$cm was obtained.

Finally, the scenario development described in Chapter 2 and the inferred experimental results from Chapter 5 were brought together in Chapter 6 to study the balance of terms in the MRE for a series of high performance MAST discharges. Though this type of analysis has been conducted in the past [41, 59, 63], the work presented here has several key differences. Firstly, an experimentally measured w_c was used, rather than one calculated using analytical models for parallel and perpendicular transport processes that are not well understood. Secondly, a probabilistic method for parameter estimation was used, representing the measured parameters as probability density functions. The functions were propagated through the analysis, giving estimates of the uncertainties on the different terms in the MRE and taking into account the correlations between the

terms due to their shared parameter dependences. In each of the discharges considered, the ideal, no wall β limit was reached. It was found that Δ' was marginally destabilising, the non-linear classical evolution term was stabilising, the bootstrap current term was strongly destabilising and the curvature term was stabilising. The contribution from the polarisation current term was found to be small and the uncertainties were significant so that the sign of this term was unclear. It is not possible to compare this result to theory as current models do not include all the necessary physics. Two β ramp-down discharges were also considered, one of which required a modification of the analysis in order to account for non-resonant coupling with NTMs on nearby rational surfaces. The measured value of w_c matched well with the observed stabilisation threshold, in both cases.

This thesis has considered different phenomena that are difficult to resolve experimentally, either because the structures under consideration are at the limits of the diagnostic resolution or because the models being tested are complicated by a large numbers of correlated parameters. One significant finding was that, assuming model assumptions hold, w_c can be resolved with the MAST Thomson scattering system with a reasonable level of certainty and that this measurement can be optimised under certain conditions and with an independent measurement of the island width. Another significant finding was that, when included in the MRE, the measured value of w_c explained the observed island threshold well. This agreement does not necessarily mean that the transport threshold is always the most important contribution for small islands; this thesis has only investigated one particular scenario. The contribution from the polarisation current may also be important, but was found to have large uncertainties due to the $1/W^3$ dependence. In addition, the polarisation current model used here is unsatisfactory as it does not include the necessary physics. There is significant potential for constraining the MRE using improved and increased numbers of measurements of the different parameters. For example, a reduction in the uncertainty on measurements of the magnetic island width would have the substantial benefit of constraining both the polarisation current contribution and w_c simultaneously. Section 7.2, below, describes potential ways in which the work from this thesis could be extended, including comparisons with a new, more complete polarisation current model and a framework for introducing multiple measurements to constrain the MRE model and rigorously find the most likely balance of contributions, given the measured data.

7.2 Future work

The value of w_c calculated in Chapter 5 is only valid for one specific MAST scenario, the characteristics of which were described in Chapters 2 and 6. In order to test this model further it would be of interest to try and alter the transport properties to see if w_c changes. As w_c depends on the $\frac{1}{4}$ power of $\chi_\perp/\chi_\parallel$, a significant change in either of these diffusivities would be required to observe a modest change in w_c. This would be further complicated by the fact that an attempt to change the discharge transport properties may result in other changes that could also influence w_c. For example, changing the pressure will also influence the local bootstrap current, resistivity and ultimately the local q profile, on which w_c depends more sensitively than $\chi_\perp$ and $\chi_\parallel$. As many tokamak parameters are correlated, it can often be difficult to perform an isolated 'scan' of a single parameter but, with careful scenario development and detailed measurements, this type of experiment might be feasible in the future. Testing the model on other tokamaks may also provide a way of varying the transport.

The model described in Chapters 4 and 5 deals specifically with conductive heat transport but there are other potentially important effects not addressed in this thesis, such as convective heat transport and density transport. These effects are complicated by the need to consider electrons and ions separately whilst ensuring quasi-neutrality, which requires kinetic modelling to calculate the electric potential and describe the transport processes properly. This has the potential to be addressed by a new code being developed at the York Plasma Institute by K. Imada [86], which builds on previous work [87]. The primary purpose of this code is to study the effects of the polarisation current with a more realistic set of assumptions than has been previously used. In this code, the island width is assumed to be small compared to the minor radius and comparable to the banana orbit width, whereas previously it has been assumed that the island is wider than the banana orbit, which is rarely the case in modern tokamaks. Furthermore, the code promises to include the contributions from both inside and outside the separatrix, which has not previously been possible. It may provide new experimentally testable predictions for the effects of the polarisation current and transport on the NTM threshold and, if so, this would be an important area of future work. Experimentally, density transport is more difficult to measure than temperature because tokamak density profiles tend to be flat, so that any magnetic island flattening is indistinguishable from the equilibrium profile. As Chapter 6 demonstrated, the polarisation current effects are difficult to

measure experimentally, but MAST's high resolution charge exchange diagnostic makes it an ideal place to study this effect.

The transport model fitting routine developed in this thesis can be implemented for both Thomson scattering systems, as in this thesis, and ECE systems, as in Meskat et al. [35] and Hölzl et al. [64]. Each implementation has associated advantages and disadvantages. The Thomson scattering T_e measurement requires relatively simple calibration and interpretation. Also, the instrument function for the MAST system is narrow enough that the light is typically considered to be emitted from a point source. The calibration of ECE diagnostics to obtain an absolute T_e measurement can be problematic and interpretation of the results can give rise to uncertainties unless the microwave emission is properly modelled. On the other hand, ECE systems provide much more data than TS systems, with typical time resolutions of ∼50kHz, which can allow time-averaging to reduce the random fluctuations that can make features of the temperature profile difficult to resolve [35]. The model presented in Chapter 4 is currently being modified for use with the 2D ECE imaging diagnostic on the K-STAR tokamak. There are still calibration and interpretation issues to overcome but if this can be achieved the high time resolution and 2D radial and poloidal grid will make it possible to map the NTM T_e profile in great detail and potentially measure w_c with unprecedented accuracy.

In Chapter 4 it was demonstrated that, with a simple application of Bayes' theorem, a constraint on a particular parameter could lead to a reduction in uncertainty on the value of a correlated parameter. In recent years, a similar, but much more detailed, approach has been developed by J. Svensson and others, in the MINERVA framework for Bayesian inference [88, 89] (used briefly in Chapter 6 to implement the magnetic island current filament model). In this framework, the system under observation is described by a joint probability density function over all parameters, which depends on the model relationships between parameters and can be influenced by measurements of parameters from different diagnostics. Each new measurement that is introduced helps to constrain the overall picture of the experiment via the models that relate the parameters to one another.

MINERVA is typically used to study axisymmetric equilibrium plasmas but a new model for studying NTMs could be developed within the framework. Chapter 5 showed how magnetic measurements could be combined with temperature measurements to help reduce uncertainties. A simlar idea has recently been implemented in Brunetti et al. [90], using ECE profiles to measure the temperature perturbation and Mirnov coils to

measure the magnetic perturbation. In Brunetti's model, an approximate analytic solution to Fitzpatrick's transport equation provides the model temperature perturbation and an approximate analytic solution to the cylindrical tearing mode equation provides the model perturbed flux. The model solutions are then fitted to experimental data with respect to a set of free parameters, including important stability parameters, such as w_c and Δ'. As the models both share parameters, each of the measurements helps to constrain the whole system. This model, or something similar based on the current filament model described in Chapter 6, could be further developed in MINERVA. Additional measurements from different diagnostics could be introduced, such as motional stark effect measurements of the perturbed current [91] or the perturbed field [92].

The idea that NTM spatial structure and temporal evolution are intrinsically linked has been an important theme in this thesis. For example, information on both w_c and Δ' can be obtained by studying the spatial structure of the magnetic and temperature perturbations or by studying the evolution of the magnetic island width. In MINERVA, both spatial and temporal models could be linked through the joint PDF of all the related parameters. This could provide much improved experimental picture of NTM stability and could be another advantage of using the Bayesian approach.

Though this thesis has provided some important information about 2/1 NTM stability on MAST, it has not been possible to conclusively answer the vital question: "Which model really explains the NTM threshold, according to the measured data?". One possible way of trying to answer this question is to use a tool, provided by Bayes' theorem and MINERVA, for testing different models: the well-known 'Occam's razor' test (the link to Bayesian probability theory is outlined by MacKay [93]). This is a way of quantitatively finding the probability that a particular model describes the underlying physics of a dataset. This is a generalisation of the reduced χ^2 test used in Chapter 5 and there is a preference towards the simplest model that fits the data, within the uncertainties. Different versions of the MRE could be tried, perhaps removing the polarisation current term or the transport threshold term, to quantitatively find out which combination of terms is most probable for the measured set of data.

Ultimately, these methods would have to be applied to multiple tokamaks in an attempt to provide scalings to ITER for the different parameters and terms. By mapping out the parameter space in detail, it may be possible to find regimes that minimise the use of the costly NTM mitigation systems and the chance of damaging disruptions in the future.

Appendix A

Connection length for a magnetic island

This is an arc length calculation using the (x, θ, ζ) coordinate system, where $x = r - r_s$. First dl must be derived for the magnetic island, then integrated along a field line.

$$dl^2 = dl_x^2 + dl_\theta^2 + dl_\zeta^2 \tag{A.1}$$

$$dl^2 = dx^2 + \left[\frac{r^2}{m^2}\right] d\theta^2 + \left[\left(\frac{Rq}{m}\frac{q_s}{q_s'}\right)^2 \frac{1}{x^2}\right] d\zeta^2 \tag{A.2}$$

$$\left(\frac{dl}{d\zeta}\right)^2 = \left(\frac{dx}{d\zeta}\right)^2 + \left[\frac{r^2}{m^2}\right]\left(\frac{d\theta}{d\zeta}\right)^2 + \left[\left(\frac{Rq}{m}\frac{q_s}{q_s'}\right)^2 \frac{1}{x^2}\right] \tag{A.3}$$

To calculate the term $\frac{dx}{d\zeta}$, the equation for island flux surface function, Ω, is rearranged:

$$\Omega = \frac{2x^2}{w^2} + \cos\zeta \tag{A.4}$$

$$x = \frac{w}{\sqrt{2}}\sqrt{\Omega - \cos\zeta} \tag{A.5}$$

$$\frac{dx}{d\zeta} = -\frac{w}{2\sqrt{2}}\frac{\sin\zeta}{\sqrt{\Omega - \cos\zeta}} \tag{A.6}$$

The following simple approximate relation is also used:

$$\frac{d\theta}{d\zeta} = 1 \tag{A.7}$$

These results are put back into the equation for $\left(\frac{dl}{d\zeta}\right)^2$ and it is rearranged to dl:

$$\left(\frac{dl}{d\zeta}\right)^2 = \frac{w^2}{8}\frac{\sin^2\zeta}{\Omega-\cos\zeta} + \frac{r^2}{m^2} + \left(\frac{Rq}{m}\frac{q_s}{q_s'}\right)^2 \frac{2}{w^2\left(\Omega-\cos\zeta\right)} \tag{A.8}$$

$$dl = \sqrt{\frac{w^2}{8}\frac{\sin^2\zeta}{\Omega-\cos\zeta} + \frac{r^2}{m^2} + \left(\frac{Rq}{m}\frac{q_s}{q_s'}\right)^2 \frac{2}{w^2\left(\Omega-\cos\zeta\right)}}\, d\zeta \tag{A.9}$$

Now the equation is integrated over ζ along a field line. Inside the separatrix, the limits are from $\zeta = \pi$ to where the flux surface crosses $x = 0$ which is at $\zeta = \cos^{-1}(\Omega)$. This only gives the length half way around so it is also necessary to multiply by 2, giving the connection length:

$$L_c = \int_{\pi}^{\cos^{-1}(\Omega)} \sqrt{\frac{w^2}{8}\frac{\sin^2\zeta}{\Omega-\cos\zeta} + \frac{r^2}{m^2} + \left(\frac{Rq}{m}\frac{q_s}{q_s'}\right)^2 \frac{2}{w^2\left(\Omega-\cos\zeta\right)}}\, d\zeta \tag{A.10}$$

By using different values of Ω and numerically calculating the integral, it is possible to obtain L_c for a particular perturbed flux surface.

Appendix B

Calculation of the parallel derivative for an asymmetric magnetic island

This appendix builds on the magnetic island geometry calculations in Chapter 3 to construct the parallel derivative for an asymmetric magnetic island, described by a quasi-linear perturbed flux. The radial coordinate used here is Ψ, the normalised equilibrium poloidal flux. Length scales w and w_c are also measured in units of normalised flux.

B.1 Flux

The flux function is given by:

$$\Omega = 2\frac{(\Psi - \Psi_s)^2}{w^2} - \left(\frac{A\,(\Psi - \Psi_s)}{w} + 1\right)\cos\zeta \tag{B.1}$$

B.2 Parallel derivative

The equilibrium magnetic field is given by a sum of toroidal and poloidal components:

$$\mathbf{B} = I\,(\Psi)\,\nabla\phi + \nabla\phi \times \nabla\,(\Psi + \psi) \tag{B.2}$$

where $\psi = \tilde{\psi}\left(\frac{A(\Psi-\Psi_s)}{w} + 1\right)\cos\zeta$.

The parallel derivative is given by $\nabla_\parallel = \mathbf{B}.\nabla/B_\phi$ assuming $B \approx B_\phi$:

$$\nabla_{\parallel} \approx \frac{\mathbf{B}.\nabla}{B_\phi} = \frac{1}{R}\frac{\partial}{\partial\phi}\bigg|_\theta + \frac{B_\theta}{rB_\phi}\frac{\partial}{\partial\theta}\bigg|_\phi + \frac{\nabla\phi\times\nabla\psi}{B_\phi}.\nabla \tag{B.3}$$

Expanding out $\nabla\psi$:

$$\nabla\psi = \frac{\partial\psi}{\partial\phi}\bigg|_\theta \nabla\phi + \frac{\partial\psi}{\partial\theta}\bigg|_\phi \nabla\theta + \frac{\partial\psi}{\partial\Psi}\bigg|_{\theta,\phi} \nabla\Psi \tag{B.4}$$

Crossing with $\nabla\phi$:

$$\nabla\phi\times\nabla\psi = 0 - \frac{1}{rR^2B_\theta}\,\frac{\partial\psi}{\partial\theta}\bigg|_\phi \nabla\Psi + rB_\theta\,\frac{\partial\psi}{\partial\Psi}\bigg|_{\theta,\phi}\nabla\theta \tag{B.5}$$

Finding the parallel part of $\nabla\phi\times\nabla\psi$:

$$\frac{\nabla\phi\times\nabla\psi}{B_\phi}.\nabla = -\frac{1}{rR^2B_\theta}\frac{1}{B_\phi}\,\frac{\partial\psi}{\partial\theta}\bigg|_\phi |\nabla\Psi|^2\,\frac{\partial}{\partial\Psi}\bigg|_{\theta,\phi} + \frac{rB_\theta}{B_\phi}\,\frac{\partial\psi}{\partial\Psi}\bigg|_{\theta,\phi}|\nabla\theta|^2\,\frac{\partial}{\partial\theta}\bigg|_\phi \tag{B.6}$$

Using $|\nabla\Psi|^2 = R^2B_\theta^2$ and $|\nabla\theta|^2 = \frac{1}{r^2}$:

$$\frac{\nabla\phi\times\nabla\psi}{B_\phi}.\nabla = -\frac{1}{Rq}\,\frac{\partial\psi}{\partial\theta}\bigg|_\phi\,\frac{\partial}{\partial\Psi}\bigg|_{\theta,\phi} + \frac{1}{Rq}\,\frac{\partial\psi}{\partial\Psi}\bigg|_{\theta,\phi}\,\frac{\partial}{\partial\theta}\bigg|_\phi \tag{B.7}$$

Now the helical angle $\zeta = m\left(\theta - \frac{\phi}{q_s}\right)$ is introduced. The following identities are used to switch $\nabla_\parallel$ from (Ψ,θ,ϕ) to (Ψ,θ,ζ) coordinates:

$$\begin{aligned}\frac{\partial}{\partial\phi}\bigg|_\theta &= \frac{\partial\zeta}{\partial\phi}\bigg|_\theta\,\frac{\partial}{\partial\zeta}\bigg|_\theta \\ &= -\frac{m}{q_s}\,\frac{\partial}{\partial\zeta}\bigg|_\theta\end{aligned} \tag{B.8}$$

$$\begin{aligned}\frac{\partial}{\partial\theta}\bigg|_\phi &= \frac{\partial}{\partial\theta}\bigg|_\zeta + \frac{\partial\zeta}{\partial\theta}\bigg|_\phi\,\frac{\partial}{\partial\zeta}\bigg|_\theta \\ &= \frac{\partial}{\partial\theta}\bigg|_\zeta + m\,\frac{\partial}{\partial\zeta}\bigg|_\theta\end{aligned} \tag{B.9}$$

$\nabla_\parallel$ becomes:

$$\nabla\phi\times\nabla\psi = \underline{\frac{1}{Rq}\left(1+\left.\frac{\partial\psi}{\partial\Psi}\right|_\zeta\right)\left.\frac{\partial}{\partial\theta}\right|_\zeta} + \frac{m}{Rq}\left(1-\frac{q}{q_s}\right)\left.\frac{\partial}{\partial\zeta}\right|_\Psi - \frac{m}{Rq}\left.\frac{\partial\psi}{\partial\zeta}\right|_\theta\left.\frac{\partial}{\partial\Psi}\right|_\zeta + \frac{m}{Rq}\left.\frac{\partial\psi}{\partial\Psi}\right|_\zeta\left.\frac{\partial}{\partial\zeta}\right|_\Psi \tag{B.10}$$

By poloidal averaging, the first term (underlined) goes to zero and the following expression is obtained:

$$\nabla_\parallel = \frac{m}{Rq}\left(1-\frac{q}{q_s}\right)\left.\frac{\partial}{\partial\zeta}\right|_\Psi - \frac{m}{Rq}\left.\frac{\partial\psi}{\partial\zeta}\right|_\theta\left.\frac{\partial}{\partial\Psi}\right|_\zeta + \frac{m}{Rq}\left.\frac{\partial\psi}{\partial\Psi}\right|_\zeta\left.\frac{\partial}{\partial\zeta}\right|_\Psi \tag{B.11}$$

Now grouping terms:

$$\nabla_\parallel = \frac{m}{Rq}\left(1-\frac{q}{q_s}\right)\left.\frac{\partial}{\partial\zeta}\right|_\Psi + \frac{m}{Rq}\tilde{\psi}\left(\frac{A}{w}\left(\Psi-\Psi_s\right)+1\right)\sin\zeta\left.\frac{\partial}{\partial\Psi}\right|_\zeta + \frac{m}{Rq}\tilde{\psi}\frac{A}{w}\cos\zeta\left.\frac{\partial}{\partial\zeta}\right|_\Psi \tag{B.12}$$

Using the first order Taylor expansion of the q profile, $q = q_s + q_s'\left(\Psi-\Psi_s\right)$:

$$\nabla_\parallel = \frac{m}{Rq}\frac{q_s'}{q_s}\left(\Psi-\Psi_s\right)\left.\frac{\partial}{\partial\zeta}\right|_\Psi + \frac{m}{Rq}\tilde{\psi}\left(\frac{A}{w}\left(\Psi-\Psi_s\right)+1\right)\sin\zeta\left.\frac{\partial}{\partial\Psi}\right|_\zeta + \frac{m}{Rq}\tilde{\psi}\frac{A}{w}\cos\zeta\left.\frac{\partial}{\partial\zeta}\right|_\Psi \tag{B.13}$$

Now substitute a rearranged form of the expression for the magnetic island half width in flux space, $\tilde{\psi} = \frac{w^2}{4}\frac{q_s'}{q_s}$:

$$\nabla_\parallel = \frac{m}{Rq}\frac{q_s'}{q_s}\left(\Psi-\Psi_s\right)\left.\frac{\partial}{\partial\zeta}\right|_\Psi + w^2\,\frac{m}{Rq}\frac{q_s'}{q_s}\frac{\frac{A}{w}\left(\Psi-\Psi_s\right)+1}{4}\sin\zeta\left.\frac{\partial}{\partial\Psi}\right|_\zeta + \frac{m}{Rq}\frac{q_s'}{q_s}\frac{A}{w}\frac{\cos\zeta}{4}\left.\frac{\partial}{\partial\zeta}\right|_\Psi \tag{B.14}$$

Finally, switch to an alternative radial coordinate, normalised to the island half width, $X = \frac{\Psi-\Psi_s}{w}$:

$$\nabla_\parallel = w\,\frac{m}{Rq}\frac{q_s'}{q_s}\left[\left(X+\frac{A\cos\zeta}{4}\right)\left.\frac{\partial}{\partial\zeta}\right|_X + \frac{AX+1}{4}\sin\zeta\left.\frac{\partial}{\partial X}\right|_\zeta\right] \tag{B.15}$$

This is the parallel derivative used in the Fitzpatrick model.

Appendix C

Calculation of matrix elements for the heat transport model

The heat transport equation:

$$\left[\left(X+\frac{A\cos\zeta}{4}\right)\left.\frac{\partial}{\partial\zeta}\right|_X+\frac{AX+1}{4}\sin\zeta\left.\frac{\partial}{\partial X}\right|_\zeta\right]^2 T+\frac{w_c^4}{w^4}\frac{\partial^2 T}{\partial X^2}=0 \tag{C.1}$$

can be solved using Fourier series solutions of the form:

$$T(X,\zeta)=\sum_{n=0}^{N}T_n(X)\cos n\zeta \tag{C.2}$$

Substitute these solutions into equation C.1.

$$\begin{aligned}0=\sum_{n=0}^{N}\Bigg[&-\left(X+\frac{A\cos\zeta}{4}\right)\frac{\partial}{\partial\zeta}\left[\left(X+\frac{A\cos\zeta}{4}\right)n\sin n\zeta T_n\right]\\&+\left(X+\frac{A\cos\zeta}{4}\right)\frac{\partial}{\partial\zeta}\left[\frac{AX+1}{4}\sin\zeta\cos n\zeta\,T_n'\right]\\&-\frac{AX+1}{4}\sin\zeta\frac{\partial}{\partial X}\left[\left(X+\frac{A\cos\zeta}{4}\right)n\sin n\zeta T_n\right]\\&+\frac{AX+1}{4}\sin\zeta\frac{\partial}{\partial X}\left[\frac{AX+1}{4}\sin\zeta\cos n\zeta\,T_n'\right]+\frac{w_c^4}{w^4}\cos n\zeta\,T_n''\Bigg]\end{aligned} \tag{C.3}$$

Expand and rearrange:

$$
\begin{aligned}
0 = \sum_{n=0}^{N} \Bigg[& -\left(X + \frac{A\cos\zeta}{4}\right)\left(n^2 X\cos n\zeta + \frac{An}{4}\left(n\cos\zeta\cos n\zeta - \sin\zeta\sin n\zeta\right)\right)T_n \\
& + \left(X + \frac{A\cos\zeta}{4}\right)\frac{AX+1}{4}\left(\cos\zeta\cos n\zeta - n\sin\zeta\sin n\zeta\right)T_n' \\
& - \frac{AX+1}{4} n\sin\zeta\sin n\zeta\left[T_n + XT_n'\right] - \frac{A\cos\zeta}{4}\frac{AX+1}{4} n\sin\zeta\sin n\zeta T_n' \\
& + \frac{AX+1}{4}\sin^2\zeta\cos n\zeta\left(\frac{A}{4}T_n' + \frac{AX+1}{4}T_n''\right) + \frac{w_c^4}{w^4}\cos n\zeta\, T_n''\Bigg]
\end{aligned}
\tag{C.4}
$$

C.1 Coefficients of X derivatives

The equation will be re-written in the form:

$$
\sum_{n=0}^{N}\left[aT_n'' + bT_n' + cT_n\right] = 0 \tag{C.5}
$$

Trig identities to be used:

$$
\begin{aligned}
\cos\zeta\cos n\zeta &= \frac{1}{2}\cos\left[(n-1)\zeta\right] + \frac{1}{2}\cos\left[(n+1)\zeta\right] \\
\cos^2\zeta\cos n\zeta &= \frac{1}{2}\cos n\zeta + \frac{1}{4}\cos\left[(n-2)\zeta\right] + \frac{1}{4}\cos\left[(n+2)\zeta\right] \\
\sin^2\zeta\cos n\zeta &= \frac{1}{2}\cos n\zeta - \frac{1}{4}\cos\left[(n-2)\zeta\right] - \frac{1}{4}\cos\left[(n+2)\zeta\right] \\
\sin\zeta\sin n\zeta &= \frac{1}{2}\cos\left[(n-1)\zeta\right] - \frac{1}{2}\cos\left[(n+1)\zeta\right] \\
\cos\zeta\sin\zeta\sin n\zeta &= \frac{1}{4}\cos\left[(n-2)\zeta\right] - \frac{1}{4}\cos\left[(n+2)\zeta\right]
\end{aligned}
\tag{C.6}
$$

C.1.1 T_n coefficient

This term has coefficient c:

$$
\begin{aligned}
c = -\left(X + \frac{A\cos\zeta}{4}\right)\Bigg(n^2 X\cos n\zeta + \frac{An}{4}\left(n\cos\zeta\cos n\zeta - \sin\zeta\sin n\zeta\right)\Bigg) \\
- \frac{AX+1}{4} n\sin\zeta\sin n\zeta
\end{aligned}
\tag{C.7}
$$

Multiply out:

$$
\begin{aligned}
c = -n^2X^2\cos n\zeta - \frac{AnX}{4}\left(n\cos\zeta\cos n\zeta - \sin\zeta\sin n\zeta\right) \\
-\frac{An^2X}{4}\cos\zeta\cos n\zeta - \frac{A^2n}{16}\cos\zeta\left(n\cos\zeta\cos n\zeta - \sin\zeta\sin n\zeta\right) \\
-\frac{AX+1}{4}n\sin\zeta\sin n\zeta
\end{aligned}
\tag{C.8}
$$

Using trig identities:

$$
\begin{aligned}
c = -n^2X^2\cos n\zeta - \frac{An^2X}{4}\left[\frac{1}{2}\cos\left[(n-1)\,\zeta\right] + \frac{1}{2}\cos\left[(n+1)\,\zeta\right]\right] \\
+\frac{AnX}{4}\left[\frac{1}{2}\cos\left[(n-1)\,\zeta\right] - \frac{1}{2}\cos\left[(n+1)\,\zeta\right]\right] \\
-\frac{An^2X}{4}\left[\frac{1}{2}\cos\left[(n-1)\,\zeta\right] + \frac{1}{2}\cos\left[(n+1)\,\zeta\right]\right] \\
-\frac{A^2n^2}{16}\left[\frac{1}{2}\cos n\zeta + \frac{1}{4}\cos\left[(n-2)\,\zeta\right] + \frac{1}{4}\cos\left[(n+2)\,\zeta\right]\right] \\
+\frac{A^2n}{16}\left[\frac{1}{4}\cos\left[(n-2)\,\zeta\right] - \frac{1}{4}\cos\left[(n+2)\,\zeta\right]\right] \\
-\frac{AX+1}{4}n\left[\frac{1}{2}\cos\left[(n-1)\,\zeta\right] - \frac{1}{2}\cos\left[(n+1)\,\zeta\right]\right]
\end{aligned}
\tag{C.9}
$$

So c can be written as:

$$
\begin{aligned}
c = -\frac{A^2n^2}{64}\left[\cos\left[(n-2)\,\zeta\right] + \cos\left[(n+2)\,\zeta\right]\right] \\
+\frac{A^2n}{64}\left[\cos\left[(n-2)\,\zeta\right] - \cos\left[(n+2)\,\zeta\right]\right] \\
-\frac{An^2X}{4}\left[\cos\left[(n-1)\,\zeta\right] + \cos\left[(n+1)\,\zeta\right]\right] \\
-\frac{n}{8}\left[\cos\left[(n-1)\,\zeta\right] - \cos\left[(n+1)\,\zeta\right]\right] \\
-\left(n^2X^2 + \frac{A^2n^2}{32}\right)\cos n\zeta
\end{aligned}
\tag{C.10}
$$

C.1.2 T'_n coefficient

This term has coefficient b:

$$b = \left(X + \frac{A\cos\zeta}{4}\right)\frac{AX+1}{4}\left(\cos\zeta\cos n\zeta - n\sin\zeta\sin n\zeta\right) \tag{C.11}$$
$$-n\left(X + \frac{A\cos\zeta}{4}\right)\frac{AX+1}{4}\sin\zeta\sin n\zeta + \frac{A}{4}\frac{AX+1}{4}\sin^2\zeta\cos n\zeta$$

Using identities to remove the sine terms:

$$\begin{aligned} b = \frac{AX+1}{4}\Bigg[&X\left(\frac{1}{2}\cos\left[(n-1)\,\zeta\right] + \frac{1}{2}\cos\left[(n+1)\,\zeta\right]\right) \\ &-2nX\left(\frac{1}{2}\cos\left[(n-1)\,\zeta\right] - \frac{1}{2}\cos\left[(n+1)\,\zeta\right]\right) \\ &+\frac{A}{4}\left[\frac{1}{2}\cos n\zeta + \frac{1}{4}\cos\left[(n-2)\,\zeta\right] + \frac{1}{4}\cos\left[(n+2)\,\zeta\right]\right] \\ &-\frac{An}{4}\left[\frac{1}{4}\cos\left[(n-2)\,\zeta\right] - \frac{1}{4}\cos\left[(n+2)\,\zeta\right]\right] \\ &-\frac{An}{4}\left[\frac{1}{4}\cos\left[(n-2)\,\zeta\right] - \frac{1}{4}\cos\left[(n+2)\,\zeta\right]\right] \\ &+\frac{A}{4}\left(\frac{1}{2}\cos n\zeta - \frac{1}{4}\cos\left[(n-2)\,\zeta\right] - \frac{1}{4}\cos\left[(n+2)\,\zeta\right]\right)\Bigg] \end{aligned} \tag{C.12}$$

So b can be written as:

$$\begin{aligned} b = \frac{AX+1}{8}\Bigg[&-\frac{An}{4}\left(\cos\left[(n-2)\,\zeta\right] - \cos\left[(n+2)\,\zeta\right]\right) \\ &+X\left(\cos\left[(n-1)\,\zeta\right] + \cos\left[(n+1)\,\zeta\right]\right) \\ &-2nX\left(\cos\left[(n-1)\,\zeta\right] - \cos\left[(n+1)\,\zeta\right]\right) \\ &+\frac{A}{2}\cos n\zeta\Bigg] \end{aligned} \tag{C.13}$$

C.1.3 T_n'' coefficient

This term has coefficient a:

$$a = \left(\frac{AX+1}{4}\right)^2\sin^2\zeta\cos n\zeta + \frac{w_c^4}{w^4}\cos n\zeta \tag{C.14}$$

Multiply out and remove sine terms:

$$a = \left(\frac{AX+1}{4}\right)^2 \left(\frac{1}{2}\cos n\zeta - \frac{1}{4}\cos\left[(n-2)\,\zeta\right] - \frac{1}{4}\cos\left[(n+2)\,\zeta\right]\right) + \frac{w_c^4}{w^4}\cos n\zeta \quad \text{(C.15)}$$

So a can be written as:

$$\begin{aligned} a = &-\left(\frac{AX+1}{8}\right)^2 \left(\cos\left[(n-2)\,\zeta\right] + \cos\left[(n+2)\,\zeta\right]\right) \\ &+ \left(\frac{1}{2}\left(\frac{AX+1}{4}\right)^2 + \frac{w_c^4}{w^4}\right)\cos n\zeta \end{aligned} \quad \text{(C.16)}$$

C.2 Matrix form of the equation

The equation is multiplied by an arbitrary cos $k\zeta$ and integrate $\frac{1}{2\pi}\int_{-\pi}^{\pi}\ldots d\zeta$. Using the following relation:

$$\begin{aligned} \frac{1}{2\pi}\int_{-\pi}^{\pi}\cos m\zeta\cos n\zeta d\zeta &= \frac{\delta_{m,n}}{2} \qquad m,n>0 \\ &= 1 \qquad m,n=0 \end{aligned} \quad \text{(C.17)}$$

The coefficients of the differential equation in X then become:

$$\begin{aligned} a_{k,n} = &-\frac{1}{128}\left(AX+1\right)^2\left(\delta_{k,n-2} + \underline{\delta_{k,2-n}} + \delta_{k,n+2} + \cancel{\delta_{k,-n-2}}\right) \\ &+ \left(\frac{1}{64}\left(AX+1\right)^2 + \frac{1}{2}\frac{w_c^4}{w^4}\right)\left(\delta_{k,n} + \underline{\delta_{k,-n}}\right) \end{aligned} \quad \text{(C.18)}$$

$$\begin{aligned} b_{k,n} = \frac{AX+1}{16}\Bigg[&-\frac{An}{4}\left(\delta_{k,n-2} + \underline{\delta_{k,2-n}} - \delta_{k,n+2} - \cancel{\delta_{k,-n-2}}\right) \\ &+X\left(\delta_{k,n-1} + \underline{\delta_{k,1-n}} + \delta_{k,n+1} + \cancel{\delta_{k,-n-1}}\right) \\ &-2nX\left(\delta_{k,n-1} + \underline{\delta_{k,1-n}} - \delta_{k,n+1} - \cancel{\delta_{k,-n-1}}\right) \\ &+\frac{A}{2}\left(\delta_{k,n} + \underline{\delta_{k,-n}}\right)\Bigg] \end{aligned} \quad \text{(C.19)}$$

$$
\begin{aligned}
c_{k,n} = &-\frac{A^2n^2}{128}\left(\delta_{k,n-2} + \underline{\delta_{k,2-n}} + \delta_{k,n+2} + \underline{\cancel{\delta_{k,-n-2}}}\right) \\
&+\frac{A^2n}{128}\left(\delta_{k,n-2} + \underline{\delta_{k,2-n}} - \delta_{k,n+2} - \underline{\cancel{\delta_{k,-n-2}}}\right) \\
&-\frac{An^2X}{8}\left(\delta_{k,n-1} + \underline{\delta_{k,1-n}} + \delta_{k,n+1} + \underline{\cancel{\delta_{k,-n-1}}}\right) \\
&-\frac{n}{16}\left(\delta_{k,n-1} + \underline{\delta_{k,1-n}} - \delta_{k,n+1} - \underline{\cancel{\delta_{k,-n-1}}}\right) \\
&-\left(\frac{1}{2}n^2X^2 + \frac{A^2n^2}{64}\right)\left(\delta_{k,n} + \underline{\delta_{k,-n}}\right)
\end{aligned}
\tag{C.20}
$$

All the 4^{th} terms can be neglected as there are negative n. The 2^{nd} terms (underlined) are only included for certain n. For example, $\delta_{k,a-n}$ is only included for $n = 0, 1, ..., a$.

There are $N+1$ coupled equations for $N+1$ Fourier modes. For each k ($0 \leq k \leq N$) we have:

$$
\sum_{n=0}^{N}\left[a_{k,n}T_n'' + b_{k,n}T_n' + c_{k,n}T_n\right] = 0 \tag{C.21}
$$

Where $a_{k,n}$, $b_{k,n}$ and $c_{k,n}$ are the matrix elements.

Appendix D

Boundary conditions for the heat transport equation

D.1 Heat Transport Equation

Recall the heat transport equation for a magnetic island:

$$\left[\left(X+\frac{A\cos\zeta}{4}\right)\left.\frac{\partial}{\partial\zeta}\right|_X+\frac{AX+1}{4}\sin\zeta\left.\frac{\partial}{\partial X}\right|_\zeta\right]^2 T+\frac{w_c^4}{w^4}\frac{\partial^2 T}{\partial X^2}=0 \tag{D.1}$$

Expand out the brackets:

$$\begin{aligned}0=&\left(X+\frac{A\cos\zeta}{4}\right)\frac{\partial}{\partial\zeta}\left[\left(X+\frac{A\cos\zeta}{4}\right)\frac{\partial T}{\partial\zeta}\right]\\&+\left(X+\frac{A\cos\zeta}{4}\right)\frac{\partial}{\partial\zeta}\left[\frac{AX+1}{4}\sin\zeta\frac{\partial T}{\partial X}\right]\\&+\frac{AX+1}{4}\sin\zeta\frac{\partial}{\partial X}\left[\left(X+\frac{A\cos\zeta}{4}\right)\frac{\partial T}{\partial\zeta}\right]\\&+\frac{AX+1}{4}\sin\zeta\frac{\partial}{\partial X}\left[\frac{AX+1}{4}\sin\zeta\frac{\partial T}{\partial X}\right]+\frac{w_c^4}{w^4}\frac{\partial^2 T}{\partial X^2}\end{aligned} \tag{D.2}$$

D.2 Boundary condition

Now the behaviour of the heat transport equation at large X is investigated. Small terms are tagged with parameter ε:

$$\left[\left(X+\varepsilon\frac{A\cos\zeta}{4}\right)\left.\frac{\partial}{\partial\zeta}\right|_X+\varepsilon\frac{AX+1}{4}\sin\zeta\left.\frac{\partial}{\partial X}\right|_\zeta\right]^2 T+\varepsilon^2\frac{w_c^4}{w^4}\frac{\partial^2 T}{\partial X^2}=0 \tag{D.3}$$

$$\begin{aligned}0=&\left(X+\varepsilon\frac{A\cos\zeta}{4}\right)\frac{\partial}{\partial\zeta}\left[\left(X+\varepsilon\frac{A\cos\zeta}{4}\right)\frac{\partial T}{\partial\zeta}\right]\\&+\left(X+\varepsilon\frac{A\cos\zeta}{4}\right)\frac{\partial}{\partial\zeta}\left[\varepsilon\frac{AX+1}{4}\sin\zeta\frac{\partial T}{\partial X}\right]\\&+\varepsilon\frac{AX+1}{4}\sin\zeta\frac{\partial}{\partial X}\left[\left(X+\varepsilon\frac{A\cos\zeta}{4}\right)\frac{\partial T}{\partial\zeta}\right]\\&+\varepsilon\frac{AX+1}{4}\sin\zeta\frac{\partial}{\partial X}\left[\varepsilon\frac{AX+1}{4}\sin\zeta\frac{\partial T}{\partial X}\right]+\varepsilon^2\frac{w_c^4}{w^4}\frac{\partial^2 T}{\partial X^2}\end{aligned} \tag{D.4}$$

Expand T as a linear sum of basis functions, also tagged with ε:

$$T=t_0+\varepsilon t_1+\varepsilon^2 t_2+\dots \tag{D.5}$$

The following sections look at the parts of the equation tagged with increasing order ε (i.e. starting with the largest terms and moving down to smaller terms).

D.2.1 $\mathbf{O}(\varepsilon^0)$

The $\mathrm{O}(\varepsilon^0)$ terms from the heat transport equation are:

$$\begin{aligned}X^2\frac{\partial^2 t_0}{\partial\zeta^2}&=0\\X^2\frac{\partial t_0}{\partial\zeta}&=c_0\end{aligned} \tag{D.6}$$

introduce operator $\langle\dots\rangle=\frac{1}{2\pi}\oint\dots d\zeta$. t_0 is periodic in ζ so $\left\langle\frac{\partial t_0}{\partial\zeta}\right\rangle=0$ and $c_0=0$. This means that t_0 is purely a function of X.

D.2.2 O(ε^1)

The O(ε^1) terms from the heat transport equation are:

$$\begin{aligned} 0 = X^2\frac{\partial^2 t_1}{\partial\zeta^2} \\ +X\frac{\partial}{\partial\zeta}\left[\frac{A\cos\zeta}{4}\cancel{\frac{\partial t_0}{\partial\zeta}}\right]+\frac{A\cos\zeta}{4}\frac{\partial}{\partial\zeta}\left[X\cancel{\frac{\partial t_0}{\partial\zeta}}\right] \\ +X\frac{\partial}{\partial\zeta}\left[\frac{AX+1}{4}\sin\zeta\frac{\partial t_0}{\partial X}\right] \\ +\frac{AX+1}{4}\sin\zeta\frac{\partial}{\partial X}\left[X\cancel{\frac{\partial t_0}{\partial\zeta}}\right] \end{aligned} \tag{D.7}$$

The ζ derivative of t_0 is equal to zero as t_0 is a function of X. Integrate w.r.t. ζ.

$$X\frac{\partial t_1}{\partial\zeta} = -\frac{AX+1}{4}\sin\zeta\frac{\partial t_0}{\partial X}+\cancel{c_1}^{0} \tag{D.8}$$

Neglect c_1 as $\langle\sin\zeta\rangle = 0$ and integrate again w.r.t ζ.

$$t_1 = \left(\frac{A}{4}+\frac{1}{4X}\right)\cos\zeta\frac{\partial t_0}{\partial X}+\bar{t_1}(X) \tag{D.9}$$

To use this as a boundary condition, the behaviour of $\bar{t_1}(X)$ at large X must also be investigated (see sections D.2.4 and D.2.5).

D.2.3 O(ε^2)

The O(ε^2) terms from the heat transport equation are:

$$\begin{aligned} 0 = X^2\frac{\partial^2 t_2}{\partial\zeta^2} \\ +X\frac{\partial}{\partial\zeta}\left[\frac{A\cos\zeta}{4}\frac{\partial t_1}{\partial\zeta}\right]+\frac{A\cos\zeta}{4}\frac{\partial}{\partial\zeta}\left[X\frac{\partial t_1}{\partial\zeta}\right] \\ +\frac{A\cos\zeta}{4}\frac{\partial}{\partial\zeta}\left[\frac{AX+1}{4}\sin\zeta\frac{\partial t_0}{\partial X}\right]+X\frac{\partial}{\partial\zeta}\left[\frac{AX+1}{4}\sin\zeta\frac{\partial t_1}{\partial X}\right] \\ +\frac{AX+1}{4}\sin\zeta\frac{\partial}{\partial X}\left[\frac{A\cos\zeta}{4}\cancel{\frac{\partial t_0}{\partial\zeta}}\right]+\frac{AX+1}{4}\sin\zeta\frac{\partial}{\partial X}\left[X\frac{\partial t_1}{\partial\zeta}\right] \\ +\frac{AX+1}{4}\sin\zeta\frac{\partial}{\partial X}\left[\frac{AX+1}{4}\sin\zeta\frac{\partial t_0}{\partial X}\right]+\frac{w_c^4}{w^4}\frac{\partial^2 t_0}{\partial X^2} \end{aligned} \tag{D.10}$$

Substitute in the equation for $\frac{\partial t_1}{\partial \zeta}$:

$$
\begin{aligned}
0 = X^2 \frac{\partial^2 t_2}{\partial \zeta^2} \qquad \text{(D.11)}\\
-\frac{\partial}{\partial \zeta}\left[\frac{A\cos\zeta}{4}\frac{AX+1}{4}\sin\zeta\frac{\partial t_0}{\partial X}\right] - \cancel{\frac{A\cos\zeta}{4}\frac{\partial}{\partial \zeta}\left[\frac{AX+1}{4}\sin\zeta\frac{\partial t_0}{\partial X}\right]}\\
+\cancel{\frac{A\cos\zeta}{4}\frac{\partial}{\partial \zeta}\left[\frac{AX+1}{4}\sin\zeta\frac{\partial t_0}{\partial X}\right]} + X\frac{\partial}{\partial \zeta}\left[\frac{AX+1}{4}\sin\zeta\frac{\partial t_1}{\partial X}\right]\\
-\cancel{\frac{AX+1}{4}\sin\zeta\frac{\partial}{\partial X}\left[\frac{AX+1}{4}\sin\zeta\frac{\partial t_0}{\partial X}\right]}\\
+\cancel{\frac{AX+1}{4}\sin\zeta\frac{\partial}{\partial X}\left[\frac{AX+1}{4}\sin\zeta\frac{\partial t_0}{\partial X}\right]} + \frac{w_c^4}{w^4}\frac{\partial^2 t_0}{\partial X^2}
\end{aligned}
$$

After doing this, various terms cancel. Now, use the $\langle \dots \rangle$ operator on the whole equation:

$$
0 = \frac{w_c^4}{w^4}\frac{\partial^2 t_0}{\partial X^2} \qquad \text{(D.12)}
$$

This shows that t_0 is linear and has the form $t_0 = BX + C$ at large X.

D.2.4 Obtaining term from O(ε^2) to substitute into O(ε^3) equation

Go back to equation D.12 and substitute in the equation $t_1 = \left(\frac{A}{4} + \frac{1}{4X}\right)\cos\zeta\frac{\partial t_0}{\partial X} + \bar{t_1}(X)$:

$$
\begin{aligned}
0 = X^2 \frac{\partial^2 t_2}{\partial \zeta^2} \qquad \text{(D.13)}\\
-\frac{\partial}{\partial \zeta}\left[\frac{A\cos\zeta}{4}\frac{AX+1}{4}\sin\zeta\frac{\partial t_0}{\partial X}\right]\\
+X\frac{\partial}{\partial \zeta}\left[\frac{AX+1}{4}\sin\zeta\frac{\partial}{\partial X}\left(\left(\frac{A}{4}+\frac{1}{4X}\right)\cos\zeta\frac{\partial t_0}{\partial X} + \bar{t_1}\right)\right]\\
+\frac{w_c^4}{w^4}\frac{\partial^2 t_0}{\partial X^2}
\end{aligned}
$$

Expanding and rearranging gives:

$$
\begin{aligned}
0 = X^2 \frac{\partial^2 t_2}{\partial \zeta^2} \\
-\frac{AX+1}{4}\frac{\partial}{\partial \zeta}\left(\sin\zeta\cos\zeta\right)\frac{A}{4}\frac{\partial t_0}{\partial X} \\
+\frac{AX+1}{4}\frac{\partial}{\partial \zeta}\left(\sin\zeta\cos\zeta\right)X\frac{\partial}{\partial X}\left[\left(\frac{A}{4}+\frac{1}{4X}\right)\frac{\partial t_0}{\partial X}\right] \\
-X\frac{AX+1}{4}\cos\zeta\frac{\partial \bar{t_1}}{\partial X}+\frac{w_c^4}{w^4}\frac{\partial^2 t_0}{\partial X^2}
\end{aligned}
\tag{D.14}
$$

Now multiply by $\cos\zeta$, divide through by X and use the $\langle \dots \rangle$ operator on the whole equation.

$$
\begin{aligned}
\left\langle X\cos\zeta\frac{\partial^2 t_2}{\partial\zeta^2}\right\rangle = \frac{AX+1}{4X}\cancelto{0}{\left\langle \cos\zeta\frac{\partial}{\partial\zeta}\left(\sin\zeta\cos\zeta\right)\right\rangle}\frac{A}{4}\frac{\partial t_0}{\partial X} \\
-\frac{AX+1}{4X}\cancelto{0}{\left\langle \cos\zeta\frac{\partial}{\partial\zeta}\left(\sin\zeta\cos\zeta\right)\right\rangle}\frac{\partial}{\partial X}\left[\left(\frac{A}{4}+\frac{1}{4X}\right)\frac{\partial t_0}{\partial X}\right]-\frac{AX+1}{4}\left\langle\cos^2\zeta\right\rangle\frac{\partial \bar{t_1}}{\partial X}
\end{aligned}
\tag{D.15}
$$

$$
\left\langle X\cos\zeta\frac{\partial^2 t_2}{\partial\zeta^2}\right\rangle = -\frac{AX+1}{4}\left\langle\cos^2\zeta\right\rangle\frac{\partial \bar{t_1}}{\partial X}
\tag{D.16}
$$

This will result is used next in $\mathrm{O}(\varepsilon^3)$ calculation.

D.2.5 $\mathbf{O}(\varepsilon^3)$

Ignore t_3 as it is negligible at large X. The $\mathrm{O}(\varepsilon^3)$ terms from the heat transport equation are:

$$
\begin{aligned}
0 = X\frac{\partial}{\partial\zeta}\left[\frac{A\cos\zeta}{4}\frac{\partial t_2}{\partial\zeta}\right]+\frac{A\cos\zeta}{4}\frac{\partial}{\partial\zeta}\left[X\frac{\partial t_2}{\partial\zeta}\right]+\frac{A\cos\zeta}{4}\frac{\partial}{\partial\zeta}\left[\frac{A\cos\zeta}{4}\frac{\partial t_1}{\partial\zeta}\right] \\
+X\frac{\partial}{\partial\zeta}\left[\frac{AX+1}{4}\sin\zeta\frac{\partial t_2}{\partial X}\right]+\frac{A\cos\zeta}{4}\frac{\partial}{\partial\zeta}\left[\frac{AX+1}{4}\sin\zeta\frac{\partial t_1}{\partial X}\right] \\
+\frac{AX+1}{4}\sin\zeta\frac{\partial}{\partial X}\left[X\frac{\partial t_2}{\partial\zeta}\right]+\frac{AX+1}{4}\sin\zeta\frac{\partial}{\partial X}\left[\frac{A\cos\zeta}{4}\frac{\partial t_1}{\partial\zeta}\right] \\
+\frac{AX+1}{4}\sin\zeta\frac{\partial}{\partial X}\left[\frac{AX+1}{4}\sin\zeta\frac{\partial t_1}{\partial X}\right]+\frac{w_c^4}{w^4}\frac{\partial^2 t_1}{\partial X^2}
\end{aligned}
\tag{D.17}
$$

Now use the $\langle \dots \rangle$ operator on the whole equation.

$$
\begin{aligned}
0 = &\left\langle \frac{A\cos\zeta}{4}\frac{\partial}{\partial\zeta}\left[X\frac{\partial t_2}{\partial\zeta}\right]\right\rangle + \left\langle \frac{A\cos\zeta}{4}\frac{\partial}{\partial\zeta}\left[\frac{A\cos\zeta}{4}\frac{\partial t_1}{\partial\zeta}\right]\right\rangle \\
&+ \left\langle \frac{A\cos\zeta}{4}\frac{\partial}{\partial\zeta}\left[\frac{AX+1}{4}\sin\zeta\frac{\partial t_1}{\partial X}\right]\right\rangle \\
&+ \left\langle \frac{AX+1}{4}\sin\zeta\frac{\partial}{\partial X}\left[X\frac{\partial t_2}{\partial\zeta}\right]\right\rangle + \left\langle \frac{AX+1}{4}\sin\zeta\frac{\partial}{\partial X}\left[\frac{A\cos\zeta}{4}\frac{\partial t_1}{\partial\zeta}\right]\right\rangle \\
&+ \left\langle \frac{AX+1}{4}\sin\zeta\frac{\partial}{\partial X}\left[\frac{AX+1}{4}\sin\zeta\frac{\partial t_1}{\partial X}\right]\right\rangle + \left\langle \frac{w_c^4}{w^4}\frac{\partial^2 t_1}{\partial X^2}\right\rangle
\end{aligned}
\tag{D.18}
$$

Substitute in the equation $t_1 = \left(\frac{A}{4} + \frac{1}{4X}\right)\cos\zeta\frac{\partial t_0}{\partial X} + \bar{t_1}(X)$. Various terms cancel as $\left\langle \cos\zeta\frac{\partial}{\partial\zeta}\left(\sin\zeta\cos\zeta\right)\right\rangle = 0$ and $\left\langle \sin^2\zeta\cos\zeta\right\rangle = 0$.

$$
\begin{aligned}
0 = &\left\langle \frac{A\cos\zeta}{4}\frac{\partial}{\partial\zeta}\left[X\frac{\partial t_2}{\partial\zeta}\right]\right\rangle - \cancel{\left\langle \frac{A\cos\zeta}{4}\frac{\partial}{\partial\zeta}\left[\frac{A\cos\zeta}{4X}\left(\frac{AX+1}{4}\sin\zeta\frac{\partial t_0}{\partial X}\right)\right]\right\rangle} \\
&+ \left\langle \frac{A\cos\zeta}{4}\frac{\partial}{\partial\zeta}\left[\frac{AX+1}{4}\sin\zeta\frac{\partial}{\partial X}\left(\left(\frac{A}{4}+\frac{1}{4X}\right)\cancel{\cos\zeta}\frac{\partial t_0}{\partial X} + \bar{t_1}\right)\right]\right\rangle \\
&+ \left\langle \frac{AX+1}{4}\sin\zeta\frac{\partial}{\partial X}\left[X\frac{\partial t_2}{\partial\zeta}\right]\right\rangle \\
&+ \cancel{\left\langle \frac{AX+1}{4}\sin\zeta\frac{\partial}{\partial X}\left[\frac{A\cos\zeta}{4X}\left(\frac{AX+1}{4}\sin\zeta\frac{\partial t_0}{\partial X}\right)\right]\right\rangle} \\
&+ \left\langle \frac{AX+1}{4}\sin\zeta\frac{\partial}{\partial X}\left[\frac{AX+1}{4}\sin\zeta\frac{\partial}{\partial X}\left(\left(\frac{A}{4}+\frac{1}{4X}\right)\cancel{\cos\zeta}\frac{\partial t_0}{\partial X} + \bar{t_1}\right)\right]\right\rangle \\
&+ \left\langle \frac{w_c^4}{w^4}\frac{\partial^2 \bar{t_1}}{\partial X^2}\right\rangle
\end{aligned}
\tag{D.19}
$$

Expanding out the $\frac{\partial}{\partial\zeta}$ differentials, the equation now reads:

$$
\begin{aligned}
0 = &\left\langle \frac{A}{4}X\cos\zeta\frac{\partial^2 t_2}{\partial\zeta^2}\right\rangle \\
&+ \frac{A}{4}\frac{AX+1}{4}\left\langle\cos^2\zeta\right\rangle\frac{\partial\bar{t_1}}{\partial X} \\
&+ \left\langle \frac{AX+1}{4}\sin\zeta\frac{\partial}{\partial X}\left[X\frac{\partial t_2}{\partial\zeta}\right]\right\rangle \\
&+ \left\langle \frac{AX+1}{4}\sin\zeta\frac{\partial}{\partial X}\left[\frac{AX+1}{4}\sin\zeta\frac{\partial\bar{t_1}}{\partial X}\right]\right\rangle + \left\langle \frac{w_c^4}{w^4}\frac{\partial^2\bar{t_1}}{\partial X^2}\right\rangle
\end{aligned}
\tag{D.20}
$$

Using $\left\langle X\cos\zeta\frac{\partial^2 t_2}{\partial\zeta^2}\right\rangle = -\frac{AX+1}{4}\left\langle\cos^2\zeta\right\rangle\frac{\partial\bar{t_1}}{\partial X}$, some other terms cancel.

$$
\begin{aligned}
0 = &-\cancel{\left\langle \cos^2\zeta \right\rangle \frac{A}{4}\frac{AX+1}{4}\frac{\partial \bar{t_1}}{\partial X}} \\
&+\cancel{\left\langle \cos^2\zeta \right\rangle \frac{A}{4}\frac{AX+1}{4}\frac{\partial \bar{t_1}}{\partial X}} \\
&+\left\langle \frac{AX+1}{4}\frac{\partial}{\partial X}\left[X\sin\zeta\frac{\partial t_2}{\partial \zeta}\right]\right\rangle \\
&+\left\langle \sin^2\zeta \right\rangle \frac{A}{4}\frac{AX+1}{4}\frac{\partial \bar{t_1}}{\partial X}+\left\langle \sin^2\zeta \right\rangle \left(\frac{AX+1}{4}\right)^2\frac{\partial^2 \bar{t_1}}{\partial X^2} \\
&+\frac{w_c^4}{w^4}\frac{\partial^2 \bar{t_1}}{\partial X^2}
\end{aligned}
\tag{D.21}
$$

The following substitution can be made:

$$
\left\langle \sin\zeta\frac{\partial t_2}{\partial \zeta}\right\rangle = \cancel{\left[\sin\zeta\frac{\partial^2 t_2}{\partial \zeta^2}\right]_0^{2\pi}}^{0} + \left\langle \cos\zeta\frac{\partial^2 t_2}{\partial \zeta^2}\right\rangle \tag{D.22}
$$

Using equation D.22 and the relation $\left\langle X\cos\zeta\frac{\partial^2 t_2}{\partial \zeta^2}\right\rangle = -\frac{AX+1}{4}\left\langle \cos^2\zeta\right\rangle\frac{\partial \bar{t_1}}{\partial X}$ this becomes:

$$
\begin{aligned}
0 = &-\left\langle \cos^2\zeta\right\rangle\left\langle \frac{AX+1}{4}\frac{\partial}{\partial X}\left[\frac{AX+1}{4}\frac{\partial \bar{t_1}}{\partial X}\right]\right\rangle \\
&+\left\langle \sin^2\zeta\right\rangle\frac{A}{4}\frac{AX+1}{4}\frac{\partial \bar{t_1}}{\partial X}+\left\langle \sin^2\zeta\right\rangle\left(\frac{AX+1}{4}\right)^2\frac{\partial^2 \bar{t_1}}{\partial X^2} \\
&+\frac{w_c^4}{w^4}\frac{\partial^2 \bar{t_1}}{\partial X^2}
\end{aligned}
\tag{D.23}
$$

Expanding out the $\frac{\partial}{\partial X}$ differentials, the equation now reads:

$$
\begin{aligned}
0 = &-\cancel{\left\langle \cos^2\zeta\right\rangle\frac{A}{4}\frac{AX+1}{4}\frac{\partial \bar{t_1}}{\partial X}}-\cancel{\left\langle \cos^2\zeta\right\rangle\left(\frac{AX+1}{4}\right)^2\frac{\partial^2 \bar{t_1}}{\partial X^2}} \\
&+\cancel{\left\langle \sin^2\zeta\right\rangle\frac{A}{4}\frac{AX+1}{4}\frac{\partial \bar{t_1}}{\partial X}}+\cancel{\left\langle \sin^2\zeta\right\rangle\left(\frac{AX+1}{4}\right)^2\frac{\partial^2 \bar{t_1}}{\partial X^2}} \\
&+\frac{w_c^4}{w^4}\frac{\partial^2 \bar{t_1}}{\partial X^2}
\end{aligned}
\tag{D.24}
$$

Which leads to the result:

$$
\frac{\partial^2 \bar{t_1}}{\partial X^2} = 0 \tag{D.25}
$$

So $\bar{t_1}$ is also linear and can be absorbed into t_0. The final boundary conditions, used in the solution of the heat transport equation, are then:

$$\begin{aligned} t_0 &= BX + C \\ t_1 &= \left(\frac{A}{4} + \frac{1}{4X}\right)\cos\zeta\frac{\partial t_0}{\partial X} \end{aligned} \tag{D.26}$$

D.3 Implementing the conditions in the finite difference scheme

At large X, we have assumed that all but the first two harmonics of $\underline{t}^i_m$ are negligible (T_n is effectively linear). The form used at the end grid points is explained below.

For the first harmonic at X^I we have:

$$\begin{aligned} t_{1m}(X) &= \left(\frac{1}{4X} + \frac{A}{4}\right)\frac{dt_{0m}}{dX} \qquad (D.27) \\ t^I_{1m} &= \left(\frac{1}{4X^I} + \frac{A}{4}\right)\frac{t^I_{0m} - t^{I-1}_{0m}}{X^I - X^{I-1}} \\ t^I_{1m} &= \left(\frac{1}{4\Delta X^I} + \frac{A}{4\Delta}\right)\left(t^I_{0m} - \alpha^{I-1}_{00}t^I_{0m} - \alpha^{I-1}_{01}t^I_{1m} - \beta^{I-1}_{0m}\right) \\ \left(\alpha^{I-1}_{01} + 4\Delta\left(\frac{1}{X^I} + A\right)^{-1}\right)t^I_{1m} &= \left(1 - \alpha^{I-1}_{00}\right)t^+_{end} - \beta^{I-1}_{0m} \\ t^I_{1m} &= \frac{\left(1 - \alpha^{I-1}_{00}\right)t^+_{end} - \beta^{I-1}_{0m}}{\alpha^{I-1}_{01} + 4\Delta\left(\frac{1}{X^I} + A\right)^{-1}} \end{aligned}$$

For the first harmonic at X^{-I} we have:

$$
\begin{aligned}
t_{1m}(X) &= \left(\frac{1}{4X}+\frac{A}{4}\right)\frac{dt_{0m}}{dX} \qquad \text{(D.28)}\\
t_{1m}^{-I} &= \left(\frac{1}{4X^{-I}}+\frac{A}{4}\right)\frac{t_{0m}^{-I+1}-t_{0m}^{-I}}{X^{-I+1}-X^{-I}}\\
t_{1m}^{-I} &= \left(\frac{1}{4\Delta X^{-I}}+\frac{A}{4\Delta}\right)\left(\alpha_{00}^{-I+1}t_{0m}^{-I}+\alpha_{01}^{-I+1}t_{1m}^{-I}+\beta_{0m}^{-I+1}\right)\\
\left(4\Delta\left(\frac{1}{X^{-I}}+A\right)^{-1}-\alpha_{01}^{-I+1}\right)t_{1m}^{-I} &= \left(\alpha_{00}^{-I+1}-1\right)t_{end}^{-}+\beta_{0m}^{-I+1}\\
t_{1m}^{-I} &= \frac{\left(\alpha_{00}^{-I+1}-1\right)t_{end}^{-}+\beta_{0m}^{-I+1}}{4\Delta\left(\frac{1}{X^{-I}}+A\right)^{-1}-\alpha_{01}^{-I+1}}
\end{aligned}
$$

The boundary condition is then:

$$
\underline{t}_{m}^{\pm I} = \begin{pmatrix} t_{end}^{\pm} \\ t_{1m}^{\pm I} \\ 0 \\ 0 \\ \vdots \end{pmatrix} \qquad \text{(D.29)}
$$

Abbreviations

NTM	**N**eoclassical **T**earing **M**ode
MRE	**M**odified **R**utherford **E**quation
MHD	**M**agneto-**H**ydro-**D**ynamics
MCF	**M**agnetic **C**onfinement **F**usion
MAST	**M**ega **A**mp **S**pherical **T**okamak
JET	**J**oint **E**uropean **T**orus
ST	**S**pherical **T**okamak
CXRS	**C**harge e**X**change **R**ecombination **S**pectroscopy
TS	**T**homson **S**cattering
ECE	**E**lectron **C**yclotron **E**mission
NBI	**N**eutral **B**eam **I**njection
ECRH	**E**lectron **C**yclotron **R**esonance **H**eating
ICRH	**I**on **C**yclotron **R**esonance **H**eating
ECCD	**E**lectron **C**yclotron **C**urrent **D**rive
HFS	**H**igh **F**ield **S**ide
LFS	**L**ow **F**ield **S**ide
SOL	**S**crape **O**ff **L**ayer
LCFS	**L**ast **C**losed **F**lux **S**urface
H-mode	**H**igh confinement **mode**
L-mode	**L**ow confinement **mode**
ELM	**E**dge **L**ocalised **M**ode
LLM	**L**ong **L**ived **M**ode
DND	**D**ouble **N**ull **D**ivertor
SND	**S**ingle **N**ull **D**ivertor
PDF	**P**robability **D**ensity **F**unction

Symbols

q	tokamak safety factor	dimensionless
β	ratio of plasma pressure to magnetic pressure	dimensionless
T_e	electron temperature	eV
n_e	electron density	m^3
T_i	ion temperature	eV
v_i	ion velocity	m/s
Ψ	equilibrium poloidal flux	Tm^2
r_s	rational surface location	m
ψ	perturbed flux	Tm^2
w	magnetic island half width	m
w_c	critical width for temperature flattening	m
T'_{end}	temperature gradient far from magnetic island	(eV/m)
T_0	temperature at rational surface	(eV)
X_0	rational surface position correction parameter	dimensionless
A	island asymmetry parameter	dimensionless
W	magnetic island full width	m
W_d	magnetic island width for which $\frac{dW}{dt}$ a maximum	m
Δ'	classical tearing stability parameter	dimensionless
a_{nl}	nonlinear classical tearing term	m^{-1}
Δ_{bs}	bootstrap contribution for NTM stability	dimensionless
Δ_{GGJ}	curvature contribution for NTM stability	dimensionless
Δ_{pol}	polarisation current contribution for NTM stability	dimensionless
j_{bs}	bootstrap current density	A
D_R	resistive interchange parameter	dimensionless

Bibliography

[1] R. Fitzpatrick. Helical temperature perturbations associated with tearing modes in tokamak plasmas. *Phys. Plasmas*, 2:825, 1995.

[2] H. A. Bethe. Energy production in stars. *Phys. Rev.*, 55:434–456, 1939.

[3] International Energy Agency. Key world energy statistics. *IEA*, 2011.

[4] M. K. Hubbert. Nuclear energy and the fossil fuels. *American Petroleum Institute*, 95, 1956.

[5] N. Tanaka (Executive Director International Energy Agency, 30/10/2007). Long-term oil supply outlook: constraints on increasing production. *OECD/IEA*.

[6] International Energy Agency. Iea world energy outlook. *IEA*, 2009.

[7] S. Solomon, D. Qin, M. Manning, Z. Chen, et al. IPCC fourth assessment report: Working group i: The physical science basis. *IPCC*, 4, 2007.

[8] C. L. Smith. The energy challenge and the case for fusion. *Talk from the "Frontiers and Interfaces" workshop, York, UK*, 2010.

[9] P. A Tipler and G. Mosca. Physics for scientists and engineers. *W. H. Freeman and Company*, page 201, 2004.

[10] J. D. Lawson. Some criteria for a power producing thermonuclear reaction. *Proc. Phys. Soc. B*, 70:6, 1957.

[11] M. Shimada D. J. Campbell, V. Mukhovatov, and and others M. Fujiwara. Progress in the ITER physics basis: Overview and summary. *Nucl. Fusion*, 47:S1S17, 2007.

[12] R. Fitzpatrick. The physics of plasmas. 1:200–202, 2008.

[13] F. Wagner. Stellarators. *Talk from the "Frontiers and Interfaces" workshop, York, UK*, 2011.

[14] F. Troyon and R. Gruber and H. Saurenmann and S. Semenzato and S. Succi. MHD-limits to plasma confinement. *Plasma Phys. Control. Fusion*, 26:209, 1984.

[15] E. J. Strait. Stability of high beta tokamak plasmas. *Phys. Plasmas*, 1:1415, 1994.

[16] F. Wagner, G. Becker, K. Behringer, D. Campbell, et al. Regime of improved confinement and high beta in neutral-beam-heated divertor discharges of the ASDEX tokamak. *Phys. Rev. Lett.*, 49:1408–1411, 1982.

[17] R. J. Bickerton, J. W. Connor, and J. B. Taylor. Diffusion driven plasma currents and bootstrap tokamak. *Nature*, 229:110–112, 1971.

[18] J. G. Cordey, C. D. Challis, and P. M. Stubberfield. Bootstrap current theory and experimental evidence. *Plasma Phys. Control. Fusion*, 30:1625, 1988.

[19] J. Wesson. Tokamaks, first edition. *Clarendon Press*, page 112, 1987.

[20] C. E. Kessel. Bootstrap current in a tokamak. *Nucl. Fusion*, 34:1222, 1994.

[21] T. Hender, J. C. Wesley, J. Bialek, A. Bondeson, et al. Progress on the ITER physics basis: Chapter 3. *Nucl. Fusion*, 47:S128S202, 2007.

[22] O. Sauter, M. A. Henderson, G. Ramponi, H. Zohm, and C. Zucca. On the requirements to control neoclassical tearing modes in burning plasmas. *Plasma Phys. Control. Fusion*, 52:025002, 2010.

[23] T. O'Gorman. Investigation of neoclassical tearing modes on MAST using Thomson scattering. *PhD Thesis, Ollscoil na h-Éireann, Corcaigh*, 2011.

[24] B. D. Dudson, N. Ben Ayed, A. Kirk, H. R. Wilson, et al. Experiments and simulation of edge turbulence and filaments in MAST. *Plasma Phys. Control. Fusion*, 50:124012, 2008.

[25] I. T. Chapman, M.-D. Hua, S.D. Pinches, R.J. Akers, et al. Saturated ideal modes in advanced tokamak regimes in MAST. *Plasma Phys. Control. Fusion*, 50:045007, 2010.

[26] S. Gerhardt, D. P. Brennan, R. Buttery, R.J. La Haye, et al. Relationship between onset thresholds, trigger types and rotation shear for the m/n = 2/1 neoclassical tearing mode in a high-β spherical torus. *Nucl. Fusion*, 49:032003, 2009.

[27] J. J. Thomson. On the number of corpuscles in an atom. *Phil. Mag*, 11:769, 1906.

[28] R. Scannell, M. J. Walsh, P. G. Carolan, A. C. Darke, et al. Design of a new Nd:YAG Thomson scattering system for MAST. *Rev. Sci. Instrum.*, 79:10E730, 2008.

[29] L. R. Baylor, K. H. Burrell, R. J. Groebner, W. A. Houlberg, D. P. Ernst, et al. Comparison of toroidal rotation velocities of different impurity ions in the DIII-D tokamak. *Phys. Plasmas*, 11:3100, 2004.

[30] N. J. Conway, P. G. Carolan, J. McCone, M. J. Walsh, and M. Wisse. High-throughput charge exchange recombination spectroscopy system on MAST. *Rev. Sci. Instrum.*, 77:10F131, 2006.

[31] M. Greenwald. Density limits in toroidal plasmas. *Plasma Phys. Control. Fusion*, 44:R27R80, 2002.

[32] H. R. Wilson. Neoclassical tearing modes. *Fusion Sci. Technol*, 49:155–163, 2006.

[33] H. P. Furth, P. H. Rutherford, and H. Selberg. Tearing mode in the cylindrical tokamak. *Phys. Fluids*, 16:1054, 1973.

[34] H. P. Furth, J. Killeen, and M. N. Rosenbluth. Finite-resistivity instabilities of a sheet pinch. *Phys. Fluids*, 6:456, 1963.

[35] J. P. Meskat, H. Zohm, G. Gantenbein, S. Günter, et al. Analysis of the structure of neoclassical tearing modes in ASDEX Upgrade. *Plasma Phys. Control. Fusion*, 43:13251332, 2001.

[36] D. De Lazzari and E. Westerhof. The role of asymmetries in the growth and suppression of neoclassical tearing modes. *Plasma Phys. Control. Fusion*, 53:035020, 2011.

[37] C. C. Hegna and J. D. Callen. Stability of tearing modes in tokamak plasmas. *Phys. Plasmas*, 1:2308, 1994.

[38] R. Carrera, R. D. Hazeltine, and M. Kotschenreuther. Island bootstrap current modification to the nonlinear dynamics of the tearing mode. *Phys. Fluids*, 29:899, 1986.

[39] Z. Chang, J. D. Callen, E. D. Fredrickson, and et al. Observation of nonlinear neoclassical pressure-gradient-driven tearing modes in TFTR. *Phys. Rev. Lett.*, 74: 4663, 1995.

[40] O. Sauter and C. Angioni and Y. R. Lin-Liu. Neoclassical conductivity and bootstrap current formulas for general axisymmetric equilibria and arbitrary collisionality regime. *Phys. Plasmas*, 6:2834–2839, 1999.

[41] R. J. Buttery, O. Sauter, R. Akers, M. Gryaznevich, et al. Neoclassical tearing physics in the spherical tokamak MAST. *Phys. Rev. Lett.*, 88:125005–1, 2002.

[42] I. T. Chapman, R. J. Buttery, S. Coda, and S. Gerhardt. Empirical scaling of sawtooth period for onset of neoclassical tearing modes. *Nucl. Fusion*, 50:102001, 2010.

[43] O. Sauter, R. J. La Haye, Z. Chang, D. A. Gates, Y. Kamada, H. Zohm, et al. Beta limits in long-pulse tokamak discharges. *Phys. Plasmas*, 4:1654, 1997.

[44] R. J. la Haye and O. Sauter. Threshold for metastable tearing modes in DIII-D. *Nucl. Fusion*, 38:987, 1998.

[45] A. Gude, S. Günter, and S. Sesnic. Seed island of neoclassical tearing modes at ASDEX Upgrade. *Nucl. Fusion*, 39:127, 1999.

[46] R. J. Buttery, M. Valovič, C.D. Warrick, and H.R. Wilson. Controlled seeding of neoclassical tearing modes in COMPASS-D. *Nucl. Fusion*, 41:985, 2001.

[47] H. R. Koslowski, E. Westerhof, M. de Bock, I. Classen, et al. Tearing mode physics studies applying the dynamic ergodic divertor on TEXTOR. *Plasma Phys. Control. Fusion*, 48:B53, 2006.

[48] D. P. Brennan, R. J. La Haye, A. D. Turnbull, M. S. Chu, et al. A mechanism for tearing onset near ideal stability boundaries. *Phys. Plasmas*, 10:1643–1652, 2003.

[49] R. McAdams, H. R. Wilson, and I. T. Chapman. Stability of high beta tokamak plasmas. *39th EPS Conference and 16th Int. Congress on Plasma Physics.*

[50] A. H. Glasser, J. M. Greene, and J. L. Johnson. Resistive instabilities in general toroidal plasma configurations. *Phys. Fluids*, 18:875–888, 1975.

[51] H. Lütjens and J. F. Luciani and X. Garbet. Curvature effects on the dynamics of tearing modes in tokamaks. *Phys. Plasmas*, 8:4267–4270, 2001.

[52] H. Lütjens, O. Sauter, and A. Bondeson. The CHEASE code for toroidal MHD equilibria. *Comput. Phys. Commun.*, 97:219–260, 1996.

[53] H. Reimerdes, O. Sauter, T. Goodman, and A. Pochelon. From current-driven to neoclassically driven tearing modes. *Phys. Rev. Lett.*, 88:105005, 2002.

[54] A. I. Smolyakov and A. Hirose and E. Lazzaro and G. B. Re and J. D. Callen. Rotating nonlinear magnetic islands in a tokamak plasma. *Phys. Plasmas*, 2:1581–1598, 1995.

[55] H. R. Wilson, J. W. Connor, R. J. Hastie, and C. C. Hegna. Threshold for neoclassical magnetic islands in a low collision frequency tokamak. *Phys. Plasmas*, 3: 248–265, 1996.

[56] R. J. La Haye, C. C. Petty, E. J. Strait, F. L. Waelbroeck, and H. R. Wilson. Propagation of magnetic islands in the $E_r = 0$ frame of co-injected neutral beam driven discharges in the DIII-D tokamak. *Phys. Plasmas*, 10:3644–3648, 2003.

[57] Q. Yu and S. Günter, and K. Lackner. Numerical modeling of nonlinear growth and saturation of neoclassical tearing modes. *Phys. Plasmas*, 11:141–150, 2004.

[58] R. J. Hastie, F. Militello, and F. Porcelli. Nonlinear saturation of tearing mode islands. *Phys. Rev. Lett.*, 95:065001, 2005.

[59] L. Urso, M. Maraschek, and H. Zohm. Fitting of the Rutherford Equation for neoclassical tearing mode stabilisation in ASDEX Upgrade. *Plasma Phys. Control. Fusion*, 25:266–273, 2005.

[60] C. J. Ham, J. W. Connor, S. C. Cowley, C. G. Gimblett, et al. Strong toroidal effects on tokamak tearing mode stability in the hybrid and conventional scenarios. *Plasma Phys. Control. Fusion*, 54:025009, 2012.

[61] R. J. La Haye, P. A. Politzer, and D. P. Brennan. Beta limit due to m/n=2/1 tearing mode onset in the DIII-D hybrid scenario. *Nucl. Fusion*, 48:015005, 2008.

[62] D. Chandra, A. Sen, P. Kaw, M. P. Bora, and S. Kruger. Effect of sheared flows on classical and neoclassical tearing modes. *Nucl. Fusion*, 45:524, 2005.

[63] O. Sauter, R. J. Buttery, R. Felton, T. C. Hender, and D. F. Howell. Marginal β-limit for neoclassical tearing modes in JET H-mode discharges. *Plasma Phys. Control. Fusion*, 44:19992019, 2002.

[64] M. Hölzl, S. Günter, I. G. J. Classen, and Q. Yu. Determination of the heat diffusion anisotropy by comparing measured and simulated electron temperature profiles across magnetic islands. *Plasma Phys. Control. Fusion*, 49:115009, 2009.

[65] K. J. Gibson, N. Barratt, I. Chapman, N. Conway, J. Snape, et al. New physics capabilities from the upgraded Thomson scattering diagnostic on MAST. *Plasma Phys. Control. Fusion*, 52:124041, 2010.

[66] J. A. Snape, K. J. Gibson, T. O'Gorman, and N. C. Barratt. The influence of finite radial transport on the structure and evolution of $m/n = 2/1$ neoclassical tearing modes on MAST. *Plasma Phys. Control. Fusion*, 54:085001, 2012.

[67] M. Turnyanskiy, D.L. Keeling, R. J. Akers, G. Cunningham, et al. Study of the fast ion connement and current prole control on MAST. *Nucl. Fusion*, 49:065002, 2011.

[68] G. E. P. Box and M. E. Muller. A note on the generation of random normal deviates. *Ann. Math. Statist.*, 29:610–611, 1958.

[69] I. G. Hughes and T. P. A. Hase. Measurements and their uncertainties: A practical guide to modern error analysis. *Oxford University Press.*, pages 90–92, 2010.

[70] D. S. Sivia and J. Skilling. Data analysis: a Bayesian tutorial. *Oxford University Press.*, 2006.

[71] A. J. Wootton, B. A. Carreras, H. Matsumoto, K. McGuire, et al. Fluctuations and anomalous transport in tokamaks. *Phys. Fluids B*, 2:2879–2903, 1990.

[72] A. L. Rosenberg, D. A. Gates, A. Pletzer, J. E. Menard, et al. Modeling of neoclassical tearing mode stability for generalized toroidal geometry. *Phys. Plasmas*, 9:4567–4572, 2002.

[73] J. W. Connor, F. L. Waelbroeck, and H. R. Wilson. The role of polarization current in magnetic island evolution. *Phys. Plasmas*, 8:2835–2848, 2001.

[74] E. Poli, A. Bergmann, and A. G. Peeters. Role of kinetic effects on the polarization current around a magnetic island. *Phys. Rev. Lett.*, 94:205001, 2005.

[75] H. Reimerdes. MHD stability limits in the TCV tokamak. *PhD Thesis, École Polytechnique Fédérale de Lausanne.*, 2001.

[76] A. Scarabosio. Stability and toroidal rotation properties of highly shaped plasmas in the TCV tokamak. *PhD Thesis, École Polytechnique Fédérale de Lausanne.*, 2006.

[77] T. J. Martin (EURATOM/UKAEA Fusion Association). *Private communication.* .

[78] G. Cunningham (EURATOM/UKAEA Fusion Association). *Private communication.* .

[79] J. Svensson and A. Werner. Current tomography for axisymmetric plasmas. *Plasma Phys. Control. Fusion*, 40:085002, 2008.

[80] A. B. Mikhailovskii, G. T. A. Huysmans, W. O. K. Kerner, and S. E. Sharapov. Optimization of computational MHD normal-mode analysis for tokamaks. *Plasma Phys. Rep*, 23:844, 1997.

[81] W. A. Houlberg, K. C. Shaing, S. P. Hirshman, and M. C. Zarnstorff. Bootstrap current and neoclassical transport in tokamaks of arbitrary collisionality and aspect ratio. *Phys. Plasmas*, 4:3230–3242, 1997.

[82] R. J. La Haye, R. J. Buttery, S. P. Gerhardt, S. A. Sabbagh, and D. P. Brennan. Aspect ratio effects on neoclassical tearing modes from comparison between DIII-D and National Spherical Torus Experiment. *Phys. Plasmas*, 19:062506, 2012.

[83] C. M. Bishop, J. W. Connor, R. J. Hastie, and S. C. Cowley. On the difficulty of determining tearing mode stability. *Plasma Phys. Control. Fusion*, 33:389–395, 1990.

[84] C. Bowman (York Plasma Institute). *Private communication.* .

[85] L. Urso, R Fischer, A Isayama, et al. Application of the Bayesian analysis to the modified Rutherford equation for NTM stabilization. *Plasma Phys. Control. Fusion*, 52:055012, 2010.

[86] K. Imada (York Plasma Institute). *Private communication.* .

[87] K. Imada and H. R. Wilson. Collision frequency dependence of polarization current in neoclassical tearing modes. *Phys. Plasmas*, 19:032120, 2012.

[88] J. Svensson, O. Ford, D. C. McDonald, A. Meakins, et al. Modelling of JET diagnostics using Bayesian graphical models. *Contrib. Plasma Phys.*, 51:152 157, 2011.

[89] J. Svensson and A. Werner. Large scale Bayesian data analysis for nuclear fusion experiments. *Proc. 21st IAEA Fusion Energy Conference*, 2006.

[90] D. Brunetti, E. Lazzaro, F. de Luca, S. Nowak, and G. Gervasini. Interpretation of tearing mode physics from ECE temperature fluctuations associated with magnetic islands and Mirnov signals. *Eur. Phys. J. D*, 64:405 411, 2011.

[91] T. Oikawa, T. Suzuki, A. Isayama, N. Hayashi, et al. Observation of the bootstrap current reduction at magnetic island in a neoclassical tearing mode plasma. *Nucl. Fusion*, 45:1101, 2005.

[92] T. Suzuki, A. Isayama, G. Matsunaga, N. Oyama, T. Fujita, and T. Oikawa. Magnetic fluctuation profile measurement using optics of motional Stark effect diagnostics in JT-60U. *Rev. Sci. Instrum.*, 79:10F533, 2008.

[93] D. J. C. MacKay. Information theory, inference, and learning algorithms. *Cambridge University Press.*, 2003.